

A Study of Voltage-Mode and Current-Mode Filters
Using Modified Current Feedback Operational Amplifier

Xin Cui

A Thesis
In the Department
of
Electrical and Computer Engineering

Presented in Partial Fulfillment of the Requirements
For the Degree of
Master of Applied Science (Electrical and Computer Engineering) at
Concordia University
Montreal, Quebec, Canada

September 2018

© Xin Cui, 2018

**CONCORDIA UNIVERSITY
SCHOOL OF GRADUATE STUDIES**

This is to certify that the thesis prepared

By: Xin Cui

Entitled: A Study of Voltage-Mode and Current-Mode Filters Using Modified Current Feedback Operational Amplifier

and submitted in partial fulfillment of the requirements for the degree of

Master of Applied Science (Electrical and Computer Engineering)

complies with the regulations of this University and meets the accepted standards with respect to originality and quality.

Signed by the final examining committee:

Chair

Dr. M.O. Ahmad

External Examiner

Dr. C.-Y. Su

Internal Examiner

Dr. R. Raut

Supervisor

Dr. M.N.S. Swamy

Approved by:

Dr. W.E. Lynch, Chair

Department of Electrical and Computer Engineering

20

Dr. Amir Asif, Dean,
Faculty of Engineering and Computer Science

Abstract

A Study of Voltage-Mode and Current-Mode Filters Using
Modified Current Feedback Operational Amplifier

Xin Cui

There is a prevalent use of current-mode (CM) circuit techniques in analog integrated circuit design, in view of the fact that CM circuits offer certain advantages over voltage-mode (VM) circuits in terms of certain performance parameters such as propagation delay, dynamic range, and bandwidth. The characteristics of a CM circuit make it not so vulnerable to the current demands of IC design trends, such as continuously decreased size and lower DC supply voltages. Therefore, some active devices that could be exploited in both CM and VM circuits have drawn a lot of attention, such as the second generation current conveyor (CCII) and operational transconductance amplifier (OTA). However, a large amount of effort has been made on VM circuits due to their dominant form of signal processing in analog circuit design for the past several decades. The concept of network transposition, introduced by Bhattacharyya and Swamy as early as in 1971, is a powerful technique to convert a VM circuit to a CM one and vice-versa, with little physical circuit alteration and retaining the same performance as its voltage-mode counterpart. It is especially attractive in transforming those circuits that employ active devices which are transposes of themselves, such as OTA or CCII-.

Recently, it has been shown in the literature that a new active element, the modified current feedback operational amplifier (MCFOA), is also its own transpose, and hence can be used to design both VM and CM circuits. It is also known that using the same MCFOA, four equivalent realizations are possible for synthesizing a VM filter function, and further, corresponding four CM filter realizations can be obtained utilizing transposition. However, no detailed study has been conducted with regard to the relative

performance of the four equivalent VM structures or the corresponding four CM structures, particularly from the point of view of the non-idealness or the parasitic effects of MCFOA on the performance.

This thesis presents a thorough study on band-pass filter (BPF) and notch filter (NF) implemented with MCFOA both in the voltage-mode and their transposed current-mode counterparts. The transfer functions of the four configurations of voltage-mode circuits, as well as that of the current-mode circuits, should be the same when the MCFOA is ideal. However, in practice, they are influenced by parasitic parameters. Accordingly, the performances of the band-pass and notch filters are influenced remarkably by the parasitic parameters of the active device, namely, MCFOA, especially the parasitic resistances for low frequency applications. These effects are studied by comparing the theoretical and SPICE simulation results of the four configurations of the voltage- and current-mode BPF and NF using non-ideal MCFOA.

In addition, an improved MCFOA that reduces the effect of parasitic resistances is proposed. Performance of BPF and NF are compared among the four configurations of voltage- and current-mode circuits using the improved MCFOA. They are also compared with those using the original version of MCFOA. It is shown that the proposed MCFOA yields several improvements on the performance of both VM and CM BPFs, such as more attenuation at the low frequencies, and drastic reduction in the ω_p and Q_p errors.

Based on the fact that MCFOA is composed of two CCIIIs (CCII+ and CCII-), and FTFN can be realized with minor modifications of CCII-, it is natural to compare the performance of BPF using CCII- and FTFN with that using MCFOA. Thus, BPF using CCII- and FTFN and their transposed circuits are also studied. As mentioned earlier, CCII- is its own transpose. However, FTFN does not have a proposed admittance or a hybrid matrix for us to find its transpose. An attempt to find the admittance matrix of FTFN is explored in this thesis. The results show that FTFN can be used as its own transpose only under ideal conditions. Comparisons of performance of BPFs using the original MCFOA, the proposed MCFOA, and CCII-, as

well as among their transposes, are presented. It is shown that BPF using the proposed MCFOA exhibits the best performance.

Acknowledgements

At the outset, I would like to express my gratitude from the bottom of my heart to my supervisor, Dr. M.N.S. Swamy. I got interested in this area of research because of the excellent graduate course on Modern Analog / Integrated Circuit Filters Analysis and Design that I took from Dr. Raut. I have been very lucky to have had the chance to study and work with them in the last three years. The doors to their offices were always open whenever I ran into a trouble on my research. Their knowledge and insight supported me to overcome one difficulty after another. They were constantly giving me encouragement, especially at times when I wanted to give up. It is an unforgettable experience in my life. Their rigorous attitude to research will always inspire me to do better in my work.

I am also grateful for all the help I received from the administrators of the Department of Electric and Computer Engineering. Without their help, my research cannot proceed smoothly. They gave a lot of help to fix problems on my computer and my experimental environment.

Finally, I would like to give my thanks to my husband, my two lovely kids, and my dear parents. They are always the first ones with whom I share my happiness and my tears, and I will keep all the warm words and hugs they gave me in my heart.

Table of Contents

List of Figures.....	xi
List of Tables	xv
List of Acronyms and symbols.....	xvii
Chapter 1 Introduction.....	1
1.1 Current-Mode Circuits	1
1.2 Advantages of Current-Mode Circuits	2
1.2.1 Source and Load Impedance	2
1.2.2 Bandwidth	3
1.2.3 Propagation Delay	5
1.3 Some Well-Known Active Elements Used in Current-Mode Circuit Design	6
1.3.1 Current Conveyor.....	6
1.3.2 Operational Transconductance Amplifier (OTA)	9
1.3.3 Current-Mode Operational Amplifier (COA)	10
1.3.4 Four Terminal Floating Nullor (FTFN)	11
1.3.5 Modified Current Feedback Operational Amplifier (MCFOA).....	13
1.4 Deriving Current-Mode Transfer Function from Voltage-Mode Transfer Function	14
1.4.1 General	14
1.4.2 Transposes of Some Active Elements [2]	17
1.5 Motivation.....	19
1.6 Thesis Outline	20

Chapter 2 Voltage and Current Transfer Function Realizations with Modified Current Feedback Operational Amplifier.....	22
2.1 Implementation of MCFOA.....	23
2.2 Equivalent Circuit Model of MCFOA	24
2.3 VTF Implementation.....	32
2.3.1 Equivalent Configurations	33
2.3.2 Procedure for the Simulation	34
2.3.3 Simulation Results for VM Band-pass Filter.....	35
2.3.4 Simulation Results for VM Notch Filter.....	38
2.3.5 Performance Comparison of VM Band-pass and Notch Filters	40
2.4 CTF Implementation	43
2.4.1 Simulation Results for CM Band-pass Filter	45
2.4.2 Simulation Results for CM Notch Filter	46
2.4.3 Performance Comparison of CM Band-pass and Notch Filters.....	48
2.5 Comparison of VTF with its Transposed CTF.....	50
2.5.1 Comparison of Transfer Functions	50
2.5.2 Comparison of Simulation Results	50
2.6 Limitation of MCFOA Based Filters	52
2.6.1 Frequency Limitations	52
2.6.2 Effect of Terminal Parasitic Resistances	53
2.7 Sensitivity.....	54
2.7.1 Sensitivity of VM filters	54

2.7.2 Sensitivity of CM filters.....	55
2.8 Conclusions	56
Chapter 3 Improved MCFOA.....	57
3.1 Implementation of Improved MCFOA	57
3.1.1 Decreasing the Resistances at Terminals X and W.....	57
3.1.2 Increasing the Resistances at Terminals Y and Z	59
3.1.3 Choice of the Current Mirror to Enhance the Resistances at Terminals Y and Z.....	64
3.2 Parasitic Parameters of Improved MCFOA	67
3.3 VTF Implemented with Improved MCFOA	71
3.3.1 Simulation Results for VM Band-pass Filter.....	71
3.3.2 Simulation Results for VM Notch Filter.....	73
3.3.3 Performance Comparison of VM Band-pass and Notch Filters	75
3.3.4 Comparison of ω_p and Q_p Errors with Old and New MCFOA for VM BPF and NF	76
3.4 CTF Implemented with Improved MCFOA	77
3.4.1 Simulation Results for CM Band-pass Filter	77
3.4.2 Simulation Results for CM Notch Filter	79
3.4.3 Performance Comparison of CM Band-pass and Notch Filters.....	80
3.4.4 Comparison of ω_p and Q_p Errors with Old and New MCFOA for CM Band-pass and Notch Filters	81
3.5 Comparison of VTF with the Transposed CTF	82
3.6 Conclusion	84

Chapter 4 Voltage and Current Transfer Function Realizations with CCII and FTFN	85
4.1 VTF and CTF Realized with CCII.....	85
4.1.1 The Implementation of CCII.....	85
4.1.2 Filter Implemented with CCII.....	91
4.1.3 Performance Comparison of Band-pass Filters Implemented Using CCII- and MCFOA	96
4.2 VTF And CTF of BPF Using FTFN	97
4.2.1 Transpose of FTFN	97
4.3 Band-pass Filters Using FTFN	100
4.3.1 Current-Mode Band-pass Filter	100
4.3.2 Voltage-mode Band-pass Filter Using FTFN	102
4.4 Conclusion	103
Chapter 5 Conclusion and Scope for Future Work	105
5.1 Conclusion	105
5.2 Future Work	107
Appendix A	108
Appendix B	119
References	129

List of Figures

Figure 1.1: Loading effect	3
Figure 1.2: Dominant pole analysis	4
Figure 1.3: (a) Symbol of CCII \pm and (b) i-v relation of CCII \pm	7
Figure 1.4: (a) CCII- (b) NMOS (c) Create ideal NMOS [14].....	8
Figure 1.5: (a) Realization of CCII+ and (b) Realization of CCII-	8
Figure 1.6: CMOS realization of CCII	9
Figure 1.7: OTA.....	10
Figure 1.8: COA	11
Figure 1.9: Nullor representation of CCII and FTFN	12
Figure 1.10: FTFN implemented from CCII+	13
Figure 1.11: MCFOA.....	14
Figure 1.12: The symbol of a two-port network.....	15
Figure 1.13: Some active devices and their transposes	19
Figure 2.1: MCFOA circuit implemented with CMOS transistors [7].....	24
Figure 2.2: Block diagram of the MCFOA proposed in [7]	24
Figure 2.3: Simulation set up to determine a_{11}	27
Figure 2.4: MCFOA terminal impedances at terminals Y and Z.....	27
Figure 2.5: MCFOA terminal impedances at terminals X and W	28
Figure 2.6: The voltage gains of the MCFOA as a function of frequency	28
Figure 2.7: The current gains of the MCFOA as a function of frequency.....	29
Figure 2.8: MCFOA model taking the parasitics into consideration	30
Figure 2.9: Differential input stage with current mirror load	32

Figure 2.10: Biquad filters proposed in [7].....	33
Figure 2.11: VM filter with triple inputs and single output [25]	35
Figure 2.12: Schematic of VM BPF of configuration (a) of Figure 2.11	36
Figure 2.13: Simulation and numerical results for BPF of Figure 2.12 (VM) and Figure 2.17 (CM)	37
Figure 2.14: Schematic of VM NF of configuration (a) of Figure 2.11	39
Figure 2.15: Simulation and numerical results for NF of Figure 2.14 (VM) and Figure 2.18 (CM)	40
Figure 2.16: Transposed CTF with current input at terminal	43
Figure 2.17: Schematic of CM BPF as the transpose of VM BPF of Figure 2.12 and using the same MCFOA as in Figure 2.12	46
Figure 2.18: Schematic of CM NF as the transpose of VM NF of Figure 2.14.....	47
Figure 3.1: Schematic of the old version of MCFOA.....	59
Figure 3.2: Simple current mirror.....	60
Figure 3.3: Cascode Current Mirror	61
Figure 3.4: High-swing cascode current mirror.....	62
Figure 3.5: Self-biased cascode current mirror.....	63
Figure 3.6: Wilson current mirror.....	63
Figure 3.7: Cascade current mirror used in the improved MCFOA.....	66
Figure 3.8: The schematics of the improved MCFOA	67
Figure 3.9: Terminal resistances at terminals X and W of the improved MCFOA	68
Figure 3.10: Terminal resistances at terminals Y and Z of the improved MCFOA	68
Figure 3.11: Current gains of the improved MCFOA	69
Figure 3.12: Voltage gains of the improved MCFOA	69
Figure 3.13: Comparison of VM and CM BPF using the old and improved MCFOA	73

Figure 3.14: Comparison of VM and CM NF using the old and improved MCFOA	75
Figure 4.1: The implementation of CCII	86
Figure 4.2: Circuit setup to determine the CCII parasitic parameters	87
Figure 4.3: Current/voltage gain frequency response of CCII+	88
Figure 4.4: Current/voltage gain frequency response of CCII-	88
Figure 4.5: Frequency response of Z_x of CCII+	89
Figure 4.6: Frequency response of Z_z of CCII+.....	89
Figure 4.7: Frequency response of Z_x of CCII-	90
Figure 4.8: Frequency response of Z_z of CCII-.....	90
Figure 4.9: Non-ideal model of CCII.....	91
Figure 4.10: VM and transposed CM BPF with two CCII-.....	92
Figure 4.11: Results for BPF of the circuits of Figure 4.10	94
Figure 4.12: The block diagram of FTFN.....	97
Figure 4.13: AC equivalent circuit of FTFN	98
Figure 4.14: The diagram of transposed FTFN	100
Figure 4.15: Current-mode filter using single FTFN.....	101
Figure 4.16: Current-mode second-order BPF with single FTFN	102
Figure 4.17: VM BPF corresponding to CM BPF using the same FTFN	102
Figure A.1: Schematics of BPF configuration (b).....	109
Figure A.2: Simulation and numerical results for BPF $Q_p = 1$ of Figures A.1 (a) and A.1 (b)	110
Figure A.3: Simulation and numerical results for BPF $Q_p = 3$ of Figures A.1 (a) and A.1 (b)	111
Figure A.4: Schematics of BPF configuration (c)	112
Figure A.5: Simulation and numerical results for BPF $Q_p = 1$ of Figures A.4 (a) and A.4 (b)	113

Figure A.6: Simulation and numerical results for BPF $Qp = 3$ of Figures A.4 (a) and A.4 (b)	114
Figure A.7: Schematics of BPF configuration (d) of Figure 2.11	115
Figure A.8: Simulation and numerical results for BPF $Qp = 1$ of Figures A.7 (a) and A.7 (b)	117
Figure A.9: Simulation and numerical results for BPF $Qp = 3$ of Figures A.7 (a) and A.7 (b)	118
Figure B.1: (a) Schematic of VM NF configuration (b) of Figure 2.11 (b) Schematic of CM configuration (b) realizing LP and HP responses.....	120
Figure B.2: Simulation and numerical results for NF $Qp = 1$ of Figure B.1 (a)	121
Figure B.3: Simulation and numerical results for NF $Qp = 3$ of Figure B.1 (a)	122
Figure B.4: Schematics of NF configuration (c) of Figure 2.11 and Figure 2.16.....	123
Figure B.5: Simulation and numerical results for NF $Qp = 1$ of Figures B.4 (a) and B.4 (b).....	124
Figure B.6: Simulation and numerical results for NF $Qp = 3$ of Figures B.4 (a) and B.4 (b).....	125
Figure B.7: (a) Schematic of VM NF configuration (d) of Figure 2.11 (b) Schematic of CM configuration realizing LP and HP responses	126
Figure B.8: Simulation and numerical results for NF $Qp = 1$ of Figure B.7 (a)	127
Figure B.9: Simulation and numerical results for NF $Qp = 3$ of Figure B.7 (a)	128

List of Tables

Table 2.1: Dimentions of the transistors in Figure 2.1.....	23
Table 2.2: Terminal parasitic parameters of the MCFOA	29
Table 2.3: Terminal resistances comparison of numerical calculation and circuit simulation results....	32
Table 2.4: $\omega_p=1\text{M rad/s}=159\text{K Hz}$, $Q_p=1$, VM BPF with MCFOA.....	41
Table 2.5: $\omega_p=1\text{M rad/s}=159\text{K Hz}$, $Q_p=3$, VM BPF with MCFOA.....	41
Table 2.6: $\omega_p=1\text{M rad/s}=159\text{K Hz}$, $Q_p=1$, VM NF with MCFOA.....	42
Table 2.7: $\omega_p=1\text{M rad/s}=159\text{K Hz}$, $Q_p=3$, VM NF with MCFOA.....	42
Table 2.8: Transfer functions of CM filters for the four configurations shown in Figure 2.16 using ideal MCFOA	44
Table 2.9: $\omega_p=1\text{M rad/s}=159\text{K Hz}$, $Q_p=1$, CM BPF with MCFOA	48
Table 2.10: $\omega_p=1\text{M rad/s}=159\text{K Hz}$, $Q_p=3$, CM BPF with MCFOA	49
Table 2.11: $\omega_p=1\text{M rad/s}=159\text{K Hz}$, $Q_p=1$, CM NF with MCFOA	49
Table 2.12: $\omega_p=1\text{M rad/s}=159\text{K Hz}$, $Q_p=3$, CM NF with MCFOA	49
Table 2.13: VM and CM BPF performance comparison	51
Table 2.14: VM and CM NF performance comparison	51
Table 3.1: Aspect ratio change of some transistors	58
Table 3.2: Aspect ratios of new added transisitors.....	66
Table 3.3: Comparison of the parasitic parameters of the improved and old MCFOA	70
Table 3.4: Comparison of the bandwidth of the improved and old MCFOA	70
Table 3.5: $\omega_p=1\text{M rad/s}=159\text{K Hz}$, $Q_p=1$, VM BPF with improved MCFOA	72
Table 3.6: $\omega_p=1\text{M rad/s}=159\text{K Hz}$, $Q_p=3$, VM BPF with improved MCFOA	72

Table 3.7: $\omega_p=1\text{M rad/s}=159\text{K Hz}$, $Q_p=1$, VM NF with improved MCFOA	74
Table 3.8: $\omega_p=1\text{M rad/s}=159\text{K Hz}$, $Q_p=3$, VM NF with improved MCFOA	74
Table 3.9: Reduction in VM BPF ω_p and Q_p errors	76
Table 3.10: Reduction in VM NF ω_p and Q_p errors	77
Table 3.11: $\omega_p=1\text{M rad/s}=159\text{K Hz}$, $Q_p=1$, CM BPF with the improved MCFOA.....	78
Table 3.12: $\omega_p=1\text{M rad/s}=159\text{K Hz}$, $Q_p=3$, CM BPF with the improved MCFOA.....	79
Table 3.13: $\omega_p=1\text{M rad/s}=159\text{K Hz}$, $Q_p=1$, CM NF with the improved MCFOA.....	80
Table 3.14: $\omega_p=1\text{M rad/s}=159\text{K Hz}$, $Q_p=3$, CM NF with the improved MCFOA.....	80
Table 3.15: Reduction in CM BPF ω_p and Q_p errors	82
Table 3.16: Reduction in CM NF ω_p and Q_p errors	82
Table 3.17: Comparison of performance of VM and CM BPF using improved MCFOA	83
Table 3.18: Comparison of performance of VM and CM NF using improved MCFOA	83
Table 4.1: Parasitic parameters of CCII- and CCII+	91
Table 4.2: CCII- BPF ω_p and Q_p errors.....	95
Table 4.3: Comparison of BPF performance implemented using MCFOA and CCII-	96

List of Acronyms and Symbols

C	<i>capacitor</i>
R	<i>resistor</i>
L	<i>inductor</i>
Q	<i>quality factor</i>
ω	<i>frequency in radians</i>
CMOS	<i>complementary metal oxide semiconductor</i>
PMOS	<i>positive-channel metal oxide semiconductor</i>
NMOS	<i>negative-channel metal oxide semiconductor</i>
MOSFET	<i>MOS field effect transistor</i>
BJT	<i>bipolar junction transistor</i>
IC	<i>integrated circuit</i>
V_{DD}	<i>positive power supply</i>
V_{SS}	<i>negative power supply</i>
r_o	<i>drain-source resistance of MOSFET</i>
g_m	<i>AC transconductance</i>
V_{ov}	<i>overdrive voltage</i>
V_{TH}	<i>threshold voltage</i>
C_{gs}	<i>gate source capacitance of MOSFET</i>
C_{gd}	<i>gate drain capacitance of MOSFET</i>
C_{ox}	<i>gate oxide capacitance</i>
μ_p	<i>charge-carrier effective mobility of PMOS</i>

CM	<i>current mode</i>
VM	<i>voltage mode</i>
CTF	<i>current transfer function</i>
VTF	<i>voltage transfer function</i>
CC	<i>current conveyor</i>
CCC	<i>composite current conveyor</i>
CCCS	<i>current control current source</i>
CCII	<i>second generation current conveyor</i>
COA	<i>current-mode operational amplifier</i>
CFA	<i>current feedback amplifier</i>
OFA	<i>operational floating amplifier</i>
Op-Amp	<i>operational amplifier</i>
OTA	<i>operational transconductance amplifier</i>
FTFN	<i>four terminal floating nullor</i>
MCFOA	<i>modified current feedback operational amplifier</i>
AC	<i>alternating current</i>
DC	<i>direct current</i>
DA	<i>differential amplifier</i>
GD	<i>generalized dual</i>
TISO	<i>triple inputs and single output</i>
SITO	<i>single input and triple outputs</i>
LPF	<i>low pass filter</i>
HPF	<i>high pass filter</i>

BPF	<i>band pass filter</i>
NF	<i>notch filter</i>
APF	<i>all pass filter</i>
dB	<i>decibel</i>
K	10^3
M	10^6
G	10^9
m	10^{-3}
μ	10^{-6}
n	10^{-9}
p	10^{-12}
F	<i>Farad, unit of capacitance</i>
H	<i>Henry, unit of inductance</i>
S	<i>Siemens, unit of conductance</i>
Ohm	<i>unit of resistance</i>
Hz	<i>Hertz, unit of measurement for frequency</i>

Chapter 1

Introduction

1.1 Current-Mode Circuits

Analog signal filtering has historically been the filtering of voltage signals. Toward the end of twentieth century, the use of current signals became of interest. The interest on current-mode circuits arose due to the difficulties that voltage-mode circuits encounter. The continuous reduction in size and power supply of CMOS technology makes voltage-mode circuits lose their advantages and face more challenges on the reduction of dynamic range, increase in the propagation delay and low noise margin. On the contrary, current-mode circuits are less influenced by the reduction of voltage power supply and increase in the speed of operation. Besides, current-mode circuits also have simpler circuit structures than the voltage-mode circuits for realizing additions and amplifications. These advances make current-mode circuits a trend.

Regarding the design of current-mode circuits, there are several current-mode active devices that have been proposed in past decades, such as second generation current conveyor (CCII), current operation amplifier (COA), operational floating amplifier (OFA), four terminal floating nullor (FTFN) and modified current feedback operational amplifier (MCFOA). Researchers have made significant effort to use the same method to generate current-mode circuits as that used to synthesize the voltage-mode circuits. However, this could be painful and time consuming. Actually, substantial synthesis work has already been done on voltage-mode circuits, and a straightforward transformation from voltage-mode to current-mode circuits is the most efficient approach. As early

as in 70's, Bhattacharyya and Swamy introduced the concept of "network transposition" [1], through which a current transfer function (CTF) can be directly obtained from a structure that realized a voltage transfer function (VTF). Later on, Swamy introduced a method to find the transpose of a multiterminal active device [2]. This has opened up the possibility of obtaining the transposed current-mode circuit from an associated voltage-mode circuit.

1.2 Advantages of Current-Mode Circuits

There is a detailed comparison of the characteristics of current-mode and voltage-mode circuits in [3]. The following presents a summary of the results.

1.2.1 Source and Load Impedance

An ideal current-mode circuit should have infinite source impedance and zero load impedance. On the contrary, an ideal voltage-mode circuit features zero source impedance and infinite load impedance. However, in practice this is not the case, and a loading effect occurs. Figure 1.1 (a) shows the loading effect of a voltage-mode circuit. The source is represented as the Thévenin equivalent circuit. Equation (1.1) shows that due to the non-zero source impedance or finite load impedance, the voltage that reaches the load is only a fraction of V_s . To minimize the loading effect, the source impedance needs to be as small as possible and load impedance needs to be as large as possible.

$$V_{load} = V_s * \frac{Z_{load}}{Z_{load} + Z_s} = V_s * \left(\frac{1}{1 + \frac{Z_s}{Z_{load}}} \right) \approx V_o * \left(1 - \frac{Z_s}{Z_{load}} \right) \quad (1.1)$$

Similarly, the source in Figure 1.1 (b) for a current-mode circuit is represented as a Norton equivalent circuit. By doing the nodal analysis, the current drawn by the load will be:

$$i_{load} = i_s * \frac{Z_s}{Z_s + Z_{load}} = i_s * \left(\frac{1}{1 + \frac{Z_{load}}{Z_s}} \right) \approx i_o * \left(1 - \frac{Z_{load}}{Z_s} \right) \quad (1.2)$$

To minimize the loading effect, the source impedance needs to be as small as possible and the load impedance needs to be as large as possible.

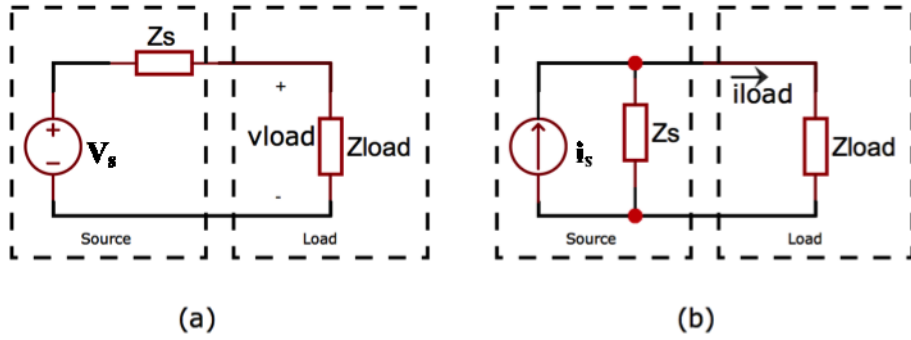


Figure 1.1: Loading effect
(a) Voltage-mode circuit and (b) Current-mode circuit

1.2.2 Bandwidth

Figure 1.2 (a) is the basic building block of the current mirror. As mentioned in 1.2.1, an ideal load in a current-mode circuit should be approaching zero, which is a short circuit at the output. This will make C_{gd2} grounded, and the only pole happens at the input. The input impedance is $\frac{1}{g_{m1}}$ due to the diode connection of M1. Accordingly, the pole of the current mirror occurs at:

$$\omega_{pin} = \frac{g_{m1}}{C_{gs1} + C_{gs2} + C_{gd2}} \quad (1.3)$$

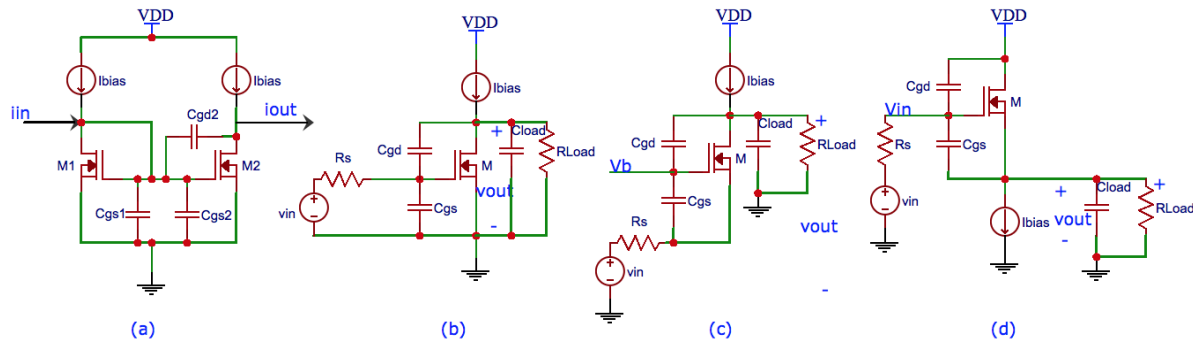


Figure 1.2: Dominant pole analysis

(a) Basic current mirror (b) Common source circuit (c) Common gate circuit (d) Source follower

Figure 1.2 (b) is a common source circuit. According to Miller's theorem, because C_{gd} is floating between the input and the output, there is an equivalent capacitance of $C_{gd}*(1-K)$ at the input side and a capacitance of $C_{gd}*(1-\frac{1}{K}) \approx C_{gd}$ at the output side, where K is the voltage gain of the common source circuit and K is very large. There are two poles for the common source circuit, one is at the input which is $\omega_{in} = \frac{1}{R_s*[C_{gs}+C_{gd}*(1-K)]}$, and the other one is at the output which is $\omega_{out} = \frac{1}{R_{Load}*(C_{Load}+C_{gd})}$. In a voltage-mode circuit, R_s should be small and R_{Load} , C_{Load} should be large. The dominant pole is the smaller one of ω_{in} and ω_{out} . Usually it is decided by ω_{out} .

Figure 1.2 (c) is a common gate circuit. There is no Miller effect because the C_{gd} is grounded. There are two poles for common gate stage, one is at the input which is $\omega_{in} = \frac{1}{(R_s/\frac{1}{gm})*C_{gs}}$, and the other one is at the output which is $\omega_{out} = \frac{1}{R_{Load}*(C_{Load}+C_{gd})}$. The above two poles are obtained by ignoring the channel length modulation. Normally R_{Load} and C_{Load} are large, and the dominant pole is ω_{out} .

Figure 1.2 (d) is a common drain circuit. There is also no Miller effect because one of the terminals of C_{gd} is grounded. By doing the open circuit time constant analysis, the pole at input is $\omega_{in} = \frac{1}{R_s * C_{gd}}$, and the pole at output is $\omega_{out} = \frac{1}{(R_{Load}/\frac{1}{gm}) * (C_{Load} + C_{gs})} \approx \frac{gm}{(C_{Load} + C_{gs})}$, ignoring the channel length modulation. Considering that $C_{gs} \gg C_{gd}$, and C_{Load} is usually large, the dominant pole of the common drain circuit is ω_{out} .

The lack of Miller effect makes common gate and common drain circuits to have wider bandwidths than a common source circuit. However, the load impedances of the three circuits are very high, and their bandwidths are low. The requirement of high load impedance is decided by the intrinsic characteristics of a voltage-mode circuit. On the other hand, the load impedance of a current-mode circuit is very low, resulting in a very high frequency pole at the output of the basic current mirror circuit. Accordingly, the dominant pole of the basic current mirror circuit occurs at the input. This dominant pole is also at much higher frequency than that of the three voltage-mode circuits, considering the low input impedance of basic current mirror circuit.

1.2.3 Propagation Delay

Analysis of a transient response reveals how fast a system can recover from a suddenly applied turn-on/off signal. This is characterized by a propagation delay in digital circuits. The following equation gives the definition of the propagation delay:

$$\text{Propagation Delay} = \frac{C * \Delta V}{\Delta I_{avg}} \quad (1.4)$$

where C is the capacitance, ΔV is the voltage swing, and ΔI_{avg} is the average charging/discharging current. Thus, the propagation delay can be reduced either by decreasing the voltage swing or

increasing the average charging/discharging current. In a voltage-mode circuit, usually the voltage swing is fixed and cannot be reduced, since it is constrained by signal to noise ratio requirements. On the contrary, the average charging and discharging current could be increased with very small variation on the nodal voltages in a current-mode circuit. Thus, a current-mode circuit could have less of a propagation delay, i.e. a faster transient response.

1.3 Some Well-Known Active Elements Used in Current-Mode Circuit Design

Active elements are fundamental building blocks that are widely employed in IC (Integrated Circuit) design. By using these building blocks, basic circuit operations and signal processing functions—such as adder, multiplier, integrator, differentiator, filters and oscillators—can be realized[4]. Due to the trend in current-mode circuits during the past decades, many active elements that could be used on current-mode circuits have been proposed and investigated in [5-9]. Many of these active elements are evolved actually from some basic elements, such as voltage feedback amplifier (VFA), current feedback amplifier (CFA), operational transconductance amplifier (OTA), and especially from current conveyor (CC) [10]. In the following, some of the current-mode active elements are described in detail.

1.3.1 Current Conveyor

The principle of the first generation of Current Conveyor (CC) was published in 1968 [11], and the second generation of Current Conveyor was proposed two years later [5]. However, it did not draw too much attention because current-mode circuits did not exhibit much more benefits than voltage-mode circuits in applications with wide voltage swings and low speed operations at that time. In addition, the lack of availability of a commercial current conveyor also limited its

popularity [10]. Hitherto, the most well-known commercial current conveyor is AD844, which is modeled as a CCII+ (positive second generation current conveyor) followed by a voltage follower [12].

CCII is categorized into two types according to its direction of the output current with respect to the input current. Figure 1.3 shows the symbol of CCII and its i-v relation. CCII is denoted by CCII+ when $i_z = i_x$, and by CCII- when $i_z = -i_x$.

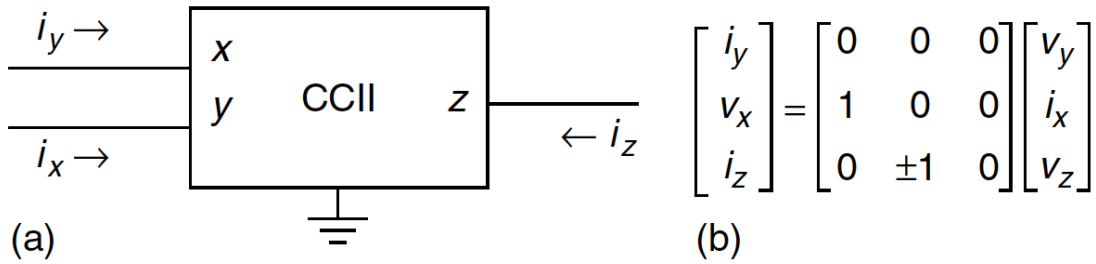


Figure 1.3: (a) Symbol of CCII \pm and (b) i-v relation of CCII \pm

There are several implementations proposed using CMOS technology. The most attractive one consists an Op-Amp and current mirrors[13]. A theoretical model is given in[14], which sees an ideal CCII- as an ideal NMOS. As shown in Figures 1.4 (a) and (b), an ideal NMOS has threshold voltage $V_{th} = 0$ and $I_g = 0$, resulting in $V_G = V_S$ and $i_D = -i_S$ respectively. Therefore, the gate of an ideal NMOS can be seen as the terminal Y of a CCII- with infinite input impedance, the source of an ideal NMOS can be seen as the terminal X with zero input impedance, and the drain of an ideal NMOS is the terminal Z with high output impedance. In a practical implementation, to make V_S approach V_D , a NMOS transistor is placed in the negative feedback loop of an Op-Amp as shown in Figure 1.4 (c). Figure 1.5 (a) is a CMOS implementation of CCII+ with the structure shown in Figure 1.4 (c). The PMOS and NMOS in the feedback loop allow the current flow in both positive and negative directions, thus forming a Class B output stage. Figure 1.5 (b) is the CMOS

implementation of CCII-. This structure has been fabricated and verified in [14]. The results show that the voltage gain between terminals Y and X is approaching the ideal situation ($V_x = V_y$) because of the high gain of an Op-amp. Comparatively, the current gain is not so ideal because it only depends on the matching properties of current mirrors. The output resistance of terminal Z should be high, and it could be increased by using cascoded current mirrors at the expense of the voltage swing reduction.

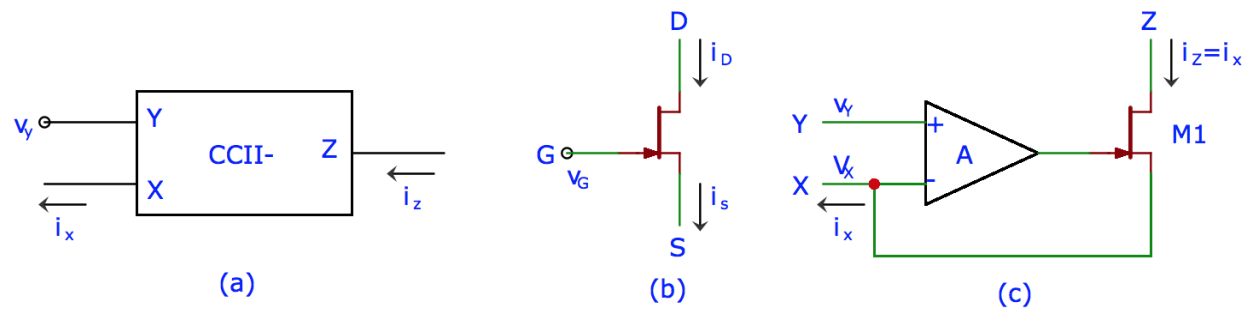


Figure 1.4: (a) CCII- (b) NMOS (c) Create ideal NMOS [14]

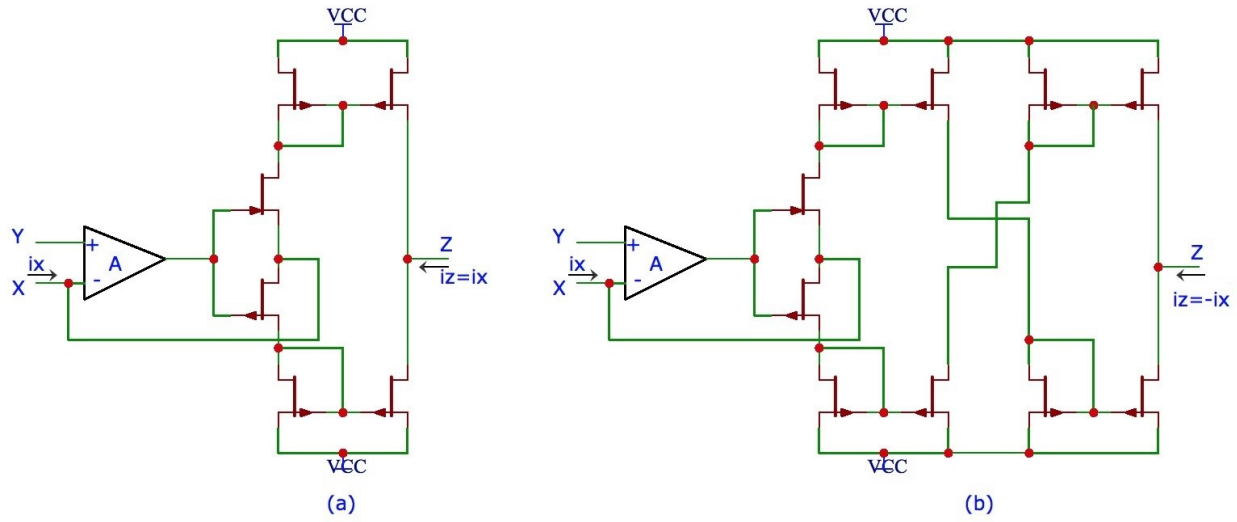


Figure 1.5: (a) Realization of CCII+ and (b) Realization of CCII-

The drawback of the CCII+/- with a structure consisting an Op-Amp and current mirrors is that it consumes substantial chip area. The reason lies in the fact that an Op-Amp occupies substantial area. Another CMOS realization of CCII+/- has been proposed in [15] by using an OTA and current mirrors. The difference between these two implementations are (1) the Op-Amp in Figure 1.5 is replaced by an OTA as shown in Figure 1.6, and (2) the CCII with the Op-Amp has a Class B output stage, and the CCII with the OTA has a Class A output stage. The advantage of the second implementation is that it saves the chip area due to its simple structure, and has a wider bandwidth (the former one has a frequency response of about 1M Hz, while the latter one can be up to 1G Hz). The downside of this improvement is the large deviation of the voltage-gain from the ideal situation due to the low voltage gain of OTA.

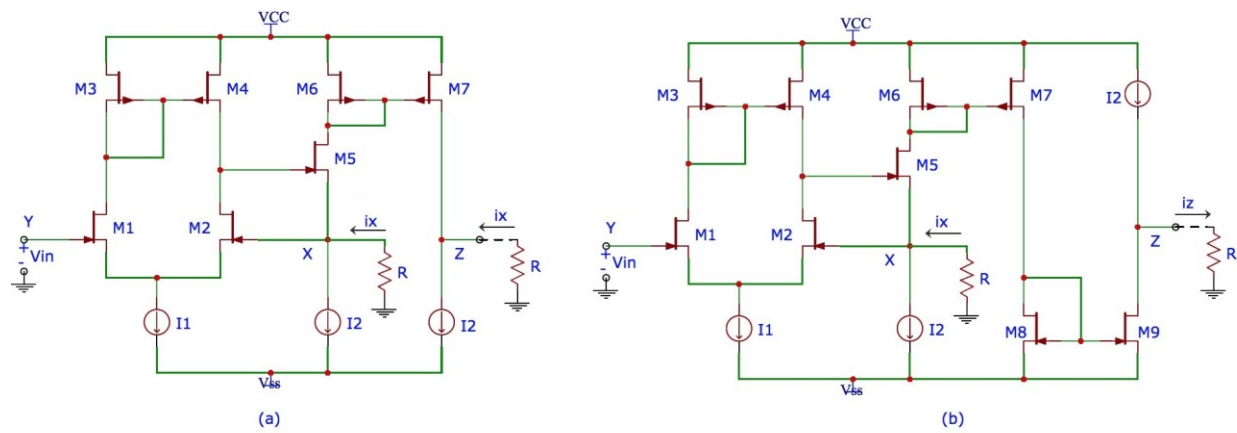


Figure 1.6: CMOS realization of CCII
 (a) CMOS realization of CCII+ (b) CMOS realization of CCII- [15]

1.3.2 Operational Transconductance Amplifier (OTA)

OTA acts as a voltage control current source with high impedance nodes at both inputs and output. For this reason, OTA is usually terminated with capacitive load. A resistive load will destroy the high gain of OTA (except a very large resistor). The block diagram of OTA is shown in Figure 1.7.

The transconductance g_m is proportional to I_{bias} , and I_{bias} is provided by an external circuit. The value of g_m is adjustable by changing I_{bias} .

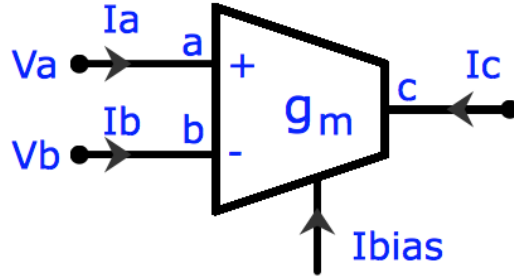


Figure 1.7: OTA

The port relation of OTA is

$$I_c = -g_m(V_a - V_b) \quad (1.5)$$

OTA is one of the most widely used active elements to implement on-chip filters. The reason lies in the fact that it can be easily implemented as a resistor. BJT and MOSFET are inherently transconductance amplifier, and they can be used as a resistor by connecting the base (gate) and collector (drain). Similarly, OTA can also be configured as a resistor by connecting the output with the input. Thus, filters containing only OTA and capacitors are very suitable for monolithic realization. In addition, like op-amp, OTA can be used to implement some building blocks, such as integrator, summer, gyrator, and frequency-dependent negative resistor (FDNR). Some building block realizations are given in [4].

1.3.3 Current-Mode Operational Amplifier (COA)

The ideal behavior of a Current-Mode Operational Amplifier (COA) is that of a current controlled current source (CCCS). Therefore, it should have low impedance at the input nodes, and high impedance at the output node. The symbol of COA is shown in Figure 1.8.

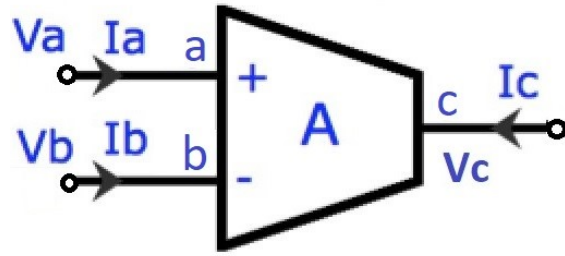


Figure 1.8: COA

The port relation of COA is

$$I_c = -A(I_a - I_b) \quad (1.6)$$

The short circuit current gain A is ideally infinity. There are several implementations of COA proposed in [16, 17].

1.3.4 Four Terminal Floating Nullor (FTFN)

There are many works that show that a four-terminals floating nullor (FTFN) is a more flexible and versatile building block. The symbol and nullor representation of an FTFN is shown in Figure 1.9 (a). Compared with the nullor representation of CCII, shown in Figure 1.9 (b), FTFN is formed with no connection between the nullator and the norator. The port relations are $I_x=I_y=0$, $V_x=V_y$, $I_z=-I_w$. There are several possible realizations of FTFN [18-21]. Generally, there are two approaches [10]. One implementation is similar to that of an operational floating amplifier (OFA) [22]. The pair of output currents are symmetrically derived from input voltages, i.e. $I_w = -I_z = G(V_x - V_y)$, ideally $G=\infty$. It can be seen as a bipolar-output OTA. Thus, the terminal resistance of terminals W and Z should be equal, or symmetrical. Another implementation uses Op-Amp and current mirrors. The current of the terminal W is derived from input voltages, while the current of

terminal Z is a current replica of the signal at terminal W. In this case, the impedances at terminals W and Z become unequal, or asymmetrical.

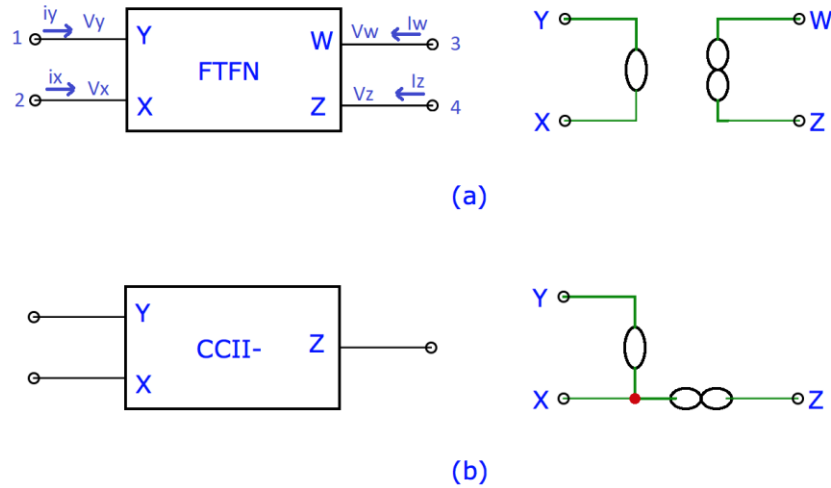


Figure 1.9: Nullor representation of CCII and FTFN
(a) FTFN symbol and nullor representation (b) CCII and nullor representation

Figure 1.9 (b) shows a possibility of implementing a FTFN with an existing CCII circuit, only by disconnecting the feedback between the output and the X node. Figures Figure 1.10 (a) and (b) are two FTFN implementations from modifying the two implementations of CCII-, which are shown in Figure 1.5 (b) and Figure 1.6 (b), respectively. This kind of implementation gives rise to an FTFN with asymmetrical impedance at terminals W and Z, because terminal W is to sink the current with ideal zero terminal impedance, and terminal Z is to steer the current with ideal infinite terminal impedance.

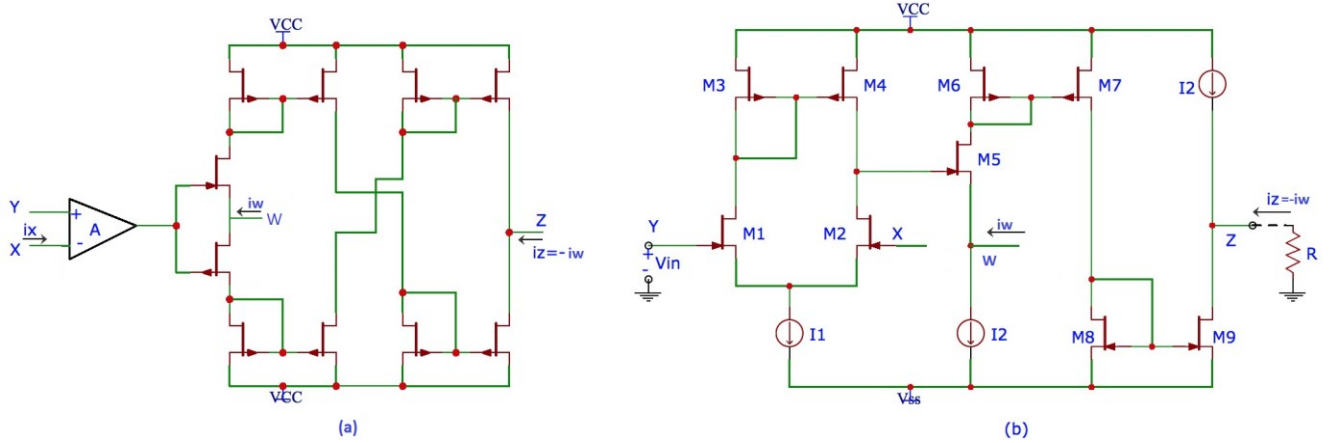


Figure 1.10: FTFN implemented from CCII+
 (a) shown in Figure 1.5(b), (b) Figure 1.6 (b)

1.3.5 Modified Current Feedback Operational Amplifier (MCFOA)

Based on the composite current conveyor introduced by Sedra and Smith [8], Yuce and Minaei [7] proposed a modified current feedback operational amplifier (MCFOA), which is more suitable for realizing active filters. Figure 1.11 (a) shows the symbol of MCFOA. The voltage-current relationships at the ports are given by

$$\begin{aligned} I_z &= \alpha_1 I_x, & I_y &= -\alpha_2 I_w \\ V_x &= \beta_1 V_y, & V_w &= \beta_2 V_z \end{aligned} \quad (1.7)$$

where ideally $\alpha_1 = \alpha_2 = \beta_1 = \beta_2 = 1$. An implementation of MCFOA with a CCII+ and a CCII- was given in [7], as shown in Figure 1.11 (b). (The implementation of the CCII+ and CCII- are shown in Figure 1.6 (a) and Figure 1.6 (b), respectively.) The hybrid matrix of the MCFOA is given by

$$\begin{bmatrix} I_Z \\ I_Y \\ V_X \\ V_W \end{bmatrix} = \begin{bmatrix} 0 & 0 & \alpha_1 & 0 \\ 0 & 0 & 0 & -\alpha_2 \\ 0 & \beta_1 & 0 & 0 \\ \beta_2 & 0 & 0 & 0 \end{bmatrix} \begin{bmatrix} V_Z \\ V_Y \\ I_X \\ I_W \end{bmatrix} \quad (1.8)$$

For convenience, such an MCFOA will be denoted by its parameter vector $P = [\alpha_1, -\alpha_2, \beta_1, \beta_2]$.

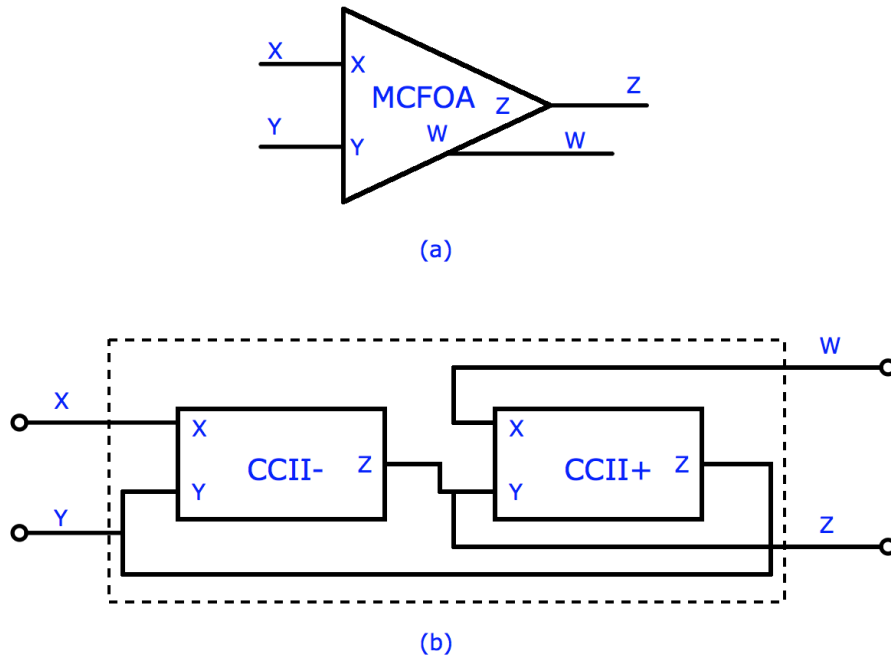


Figure 1.11: MCFOA

(a) Symbolic representation of MCFOA (b) Implementation of MCFOA with two CCIIIs

1.4 Deriving Current-Mode Transfer Function from Voltage-Mode Transfer Function

1.4.1 General

As mentioned before, voltage mode circuits have been studied thoroughly despite the fact that the concept of current mode circuits was proposed almost at the same time as the concept of voltage-mode circuits. Therefore, it will be very efficient if one could take advantage of available methods

of realizing a voltage transfer function (VTF) to synthesize a current transfer function (CTF). In general, there are two approaches to derive CTF from VTF: the first one is by obtaining the transposition of a network, the concept of which has been introduced in [1]; the second one is by utilizing the concept of Generalized Dual (GD), which was reported in [23, 24]. In the following, a brief introduction to this topic is included. Suppose the chain matrix of a two ports network N, whose block diagram is given in Figure 1.12, is

$$[a]_N = \begin{bmatrix} A & B \\ C & D \end{bmatrix} \quad (1.9)$$

From the definition of a two ports chain matrix, A is the voltage gain with $\frac{1}{A} \frac{V_2}{V_1} |_{I_2=0}$, and D is the current gain with $\frac{1}{D} \frac{I_2}{I_1} |_{V_1=0}$, where V_1 and I_1 are the voltage and current at port 1, and V_2 and I_2 are the voltage and current at port 2. As a result, $\frac{1}{A}$ is the VTF of a two ports network, and $\frac{1}{D}$ is the CTF of a two-port network.

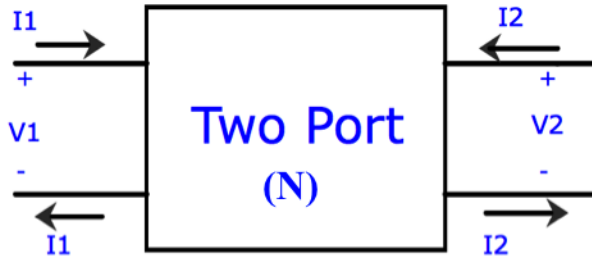


Figure 1.12: The symbol of a two-port network

The reversed transpose network N_R^T , which is obtained by transposing N and reversing the input and output ports of the transposed network will be

$$[a]_{N_R^T} = \begin{bmatrix} D & B \\ C & A \end{bmatrix} \quad (1.10)$$

Further, the chain matrix of the generalized dual (GD) network of N, i.e. N_D , with respect to $f(s)$, is given by [4]

$$[a]_{N_D} = \begin{bmatrix} D & Cf(s) \\ \frac{B}{f(s)} & A \end{bmatrix} \quad (1.11)$$

Obviously, the CTF of N_R^T and N_D is the VTF of N. So, it is possible to obtain the structure of CTF from VTF by finding the GD or transpose of the original network N. In practical operation, the method of GD is not desirable for two reasons: (1) a grounded active element becomes floating in its dual network, which brings extra parasitic capacitance and an increase of common mode noise; (2) it is difficult to choose a proper $f(s)$ to keep an active element in its resistive nature without introducing a passive inductor. The above two reasons make GD approach to convert from VTF to CTF and vice versa unattractive in integrated circuit and systems design. A detailed example to explain these situations has been given in [4].

The transposition is achieved by replacing the nonreciprocal sub-network of N (i.e. an active element) by its transpose and keeping the reciprocal part (the passive circuit) unchanged. A method to find the transposed elements corresponding to an N port element with a given hybrid matrix is proposed in [2]. If a given building block with n-ports and $(n+1)$ -terminals has a hybrid matrix G, i.e.,

$$\begin{bmatrix} I_A \\ V_B \end{bmatrix} = \begin{bmatrix} G_{11} & G_{12} \\ G_{21} & G_{22} \end{bmatrix} \begin{bmatrix} V_A \\ I_B \end{bmatrix} \quad (1.12)$$

$$I_A = [I_1, I_2, \dots, I_m]^T, I_B = [I_{m+1}, I_{m+2}, \dots, I_n]^T$$

$$V_A = [V_1, V_2, \dots, V_m]^T, V_B = [V_{m+1}, V_{m+2}, \dots, V_n]^T$$

then, the transposed element's hybrid matrix G' is given by

$$\begin{bmatrix} I'_A \\ V'_B \end{bmatrix} = G' \begin{bmatrix} V'_A \\ I'_B \end{bmatrix} = \begin{bmatrix} G_{11}^T & -G_{21}^T \\ -G_{12}^T & G_{22}^T \end{bmatrix} \begin{bmatrix} V'_A \\ I'_B \end{bmatrix} \quad (1.13)$$

where $I'_A = [I'_1, I'_2, \dots, I'_m]^T$, $I'_B = [I'_{m+1}, I'_{m+2}, \dots, I'_n]^T$

$V'_A = [V'_1, V'_2, \dots, V'_m]^T$, $V'_B = [V'_{m+1}, V'_{m+2}, \dots, V'_n]^T$

1.4.2 Transposes of Some Active Elements [2]

The hybrid matrices of a CCII+/- and a MCFOA have been shown in Figure 1.3 (b) and Equation (1.8). By using Equation (1.13), one can easily find the transposes of these active elements.

For a CCII+, the hybrid matrix of its transpose is shown in Equation (1.14). This is a building block of ICCII- (inverted CCII-), which is defined in [6].

$$\begin{bmatrix} I'_y \\ I'_z \\ V'_x \end{bmatrix} = \begin{bmatrix} 0 & 0 & -1 \\ 0 & 0 & 0 \\ 0 & -1 & 0 \end{bmatrix} \begin{bmatrix} V'_y \\ V'_z \\ I'_x \end{bmatrix} \quad (1.14)$$

For a CCII-, its transposed hybrid matrix is given by

$$\begin{bmatrix} I'_y \\ I'_z \\ V'_x \end{bmatrix} = \begin{bmatrix} 0 & 0 & -1 \\ 0 & 0 & 0 \\ 0 & 1 & 0 \end{bmatrix} \begin{bmatrix} V'_y \\ V'_z \\ I'_x \end{bmatrix} \quad (1.15)$$

This indicates that the transpose of a CCII- is itself with the connection of its Y and Z terminals to the outside circuit elements interchanged.

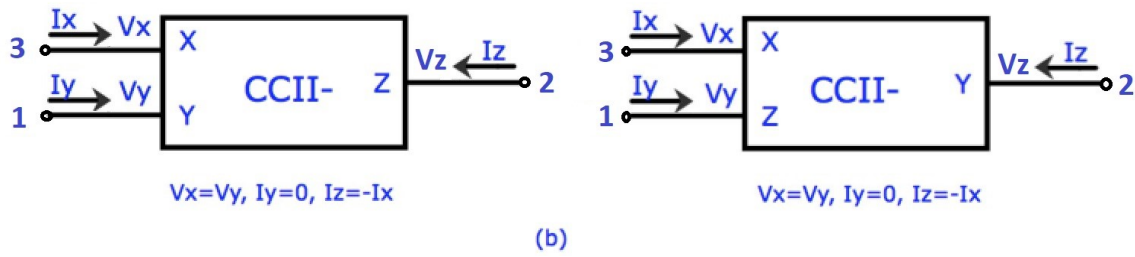
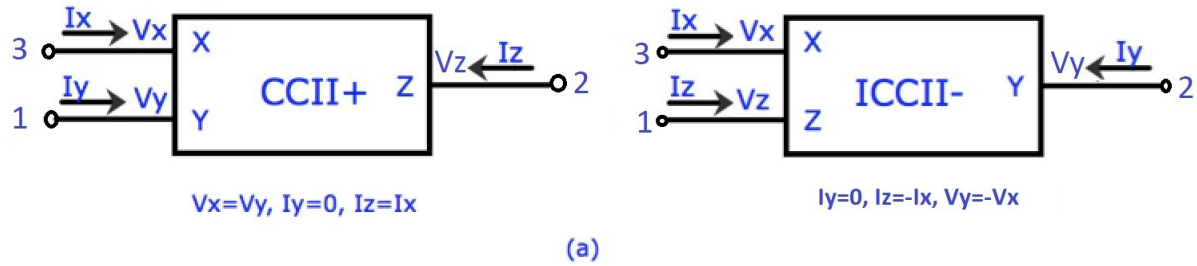
The transpose of MCFOA is given by [25]

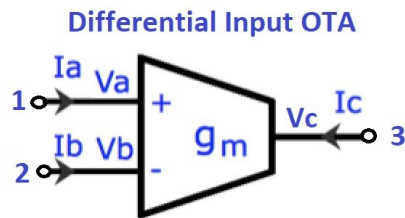
$$\begin{bmatrix} I'_z \\ I'_y \\ V'_x \\ V'_w \end{bmatrix} = \begin{bmatrix} 0 & 0 & 0 & -\beta_2 \\ 0 & 0 & -\beta_1 & 0 \\ -\alpha_1 & 0 & 0 & 0 \\ 0 & \alpha_2 & 0 & 0 \end{bmatrix} \begin{bmatrix} V'_z \\ V'_y \\ I'_x \\ I'_w \end{bmatrix} \quad (1.16)$$

It is seen that the transpose is another MCFOA with parameter vector $[-\beta_2, -\beta_1, \alpha_2, -\alpha_1]$. Thus, we may define the transpose of an MCFOA with $P = [\alpha_1, -\alpha_2, \beta_1, \beta_2]$ and with its Y, X, W and Z terminals connected to external nodes 1, 2, 3 and 4 to be another MCFOA whose parameter vector is $[-\beta_2, -\beta_1, \alpha_2, -\alpha_1]$ and having its Y, X, W and Z terminals connected to 1, 3, 2 and 4, respectively, i.e., the position of Y and Z are unchanged, while those of X and Z are interchanged.

For a FTFN, it is impossible to write the hybrid matrix directly from its port relations. The reason lies in the fact that the terminal W and Z of a FTFN are current sources, which leads to uncertain voltages at terminal W and Z (V_w and V_z). This uncertainty is dictated by the intrinsic characteristic of a current source. However, it is possible to write an admittance matrix. This opens the possibility to find its transpose from the admittance matrix. This is discussed further in Chapter 4.

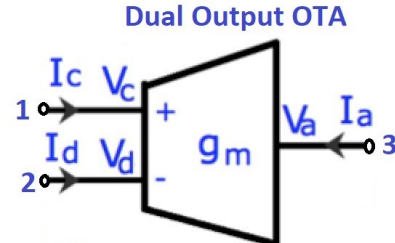
The block diagrams of some of the active elements and their transposes are shown in Figure 1.13 (a) – (e).



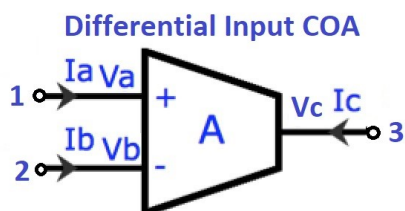


$$I_a = I_b = 0, \quad I_c = -g_m(V_a - V_b)$$

(c)

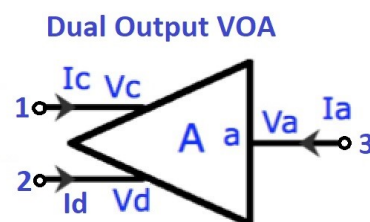


$$I_a = 0, \quad I_c = -g_m V_a, \quad I_d = g_m V_a$$

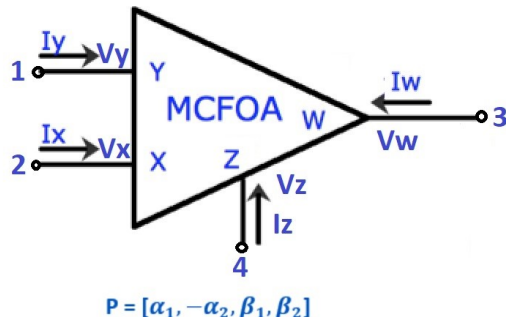


$$V_a = V_b = 0, \quad I_c = -A(I_a - I_b)$$

(d)



$$I_a = 0, \quad V_c = A V_a, \quad V_d = -A V_a$$



(e)

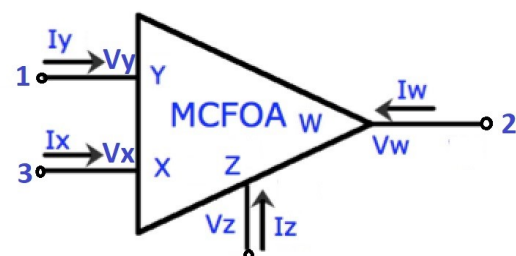


Figure 1.13: Some active devices and their transposes

- (a) CCII+ and its transpose, (b) CCII- and its transpose, (c) OTA and its transpose,
- (d) COA and its transpose, (e) MCFOA and its transpose

1.5 Motivation

Although the theory of transposed network has been proposed as early as in 1971[1], little work has been done to verify the performances and feasibility on real circuits. The reason could be that separate devices need to be invented to obtain current mode operation. We have seen that CCII-,

OTA and MCFOA are three active devices whose transposes are themselves [2, 25]. Thus, we could use an OTA, a CCII- or a MCFOA both for voltage and current mode filtering. Further, while several active devices have been used to realize voltage- and current-mode filters, very few of the reported works have analyzed and reported the influence of the non-idealities of the active devices on the performance of the associated analog filters.

The above two items constitute the motivation for the work undertaken in this thesis, wherein MCFOA is used as the active device.

1.6 Thesis Outline

Chapter 2 presents a discussion on the realizations of voltage-mode band-pass filter and notch filter using MCFOA, as well as their transposes using the same MCFOA. Three alternative realizations of BPF, NF and their transposes are also studied. The parasitic resistances are taken into consideration, and their effect on the performance of BPFs and NFs are also investigated. Comparisons among the four configurations, as well as a comparison between voltage and current-mode realizations are presented.

Chapter 3 introduces an improvement on MCFOA realization with regard to the effects resulting from parasitic resistances. The same simulation procedures on the four configurations of BPFs and NFs done in Chapter 2 are repeated in Chapter 3 using the proposed MCFOA, so that the performance can be compared with that using the original MCFOA.

Chapter 4 presents a study of BPF using CCII- and its transpose using the same CCII-. The effect caused by parasitic resistances are investigated, and the performance of the VTF circuit is compared with that of the transposed CTF circuit. In addition, a possible admittance matrix for FTFN is proposed and utilized to find a transpose under ideal conditions. So far, all the filter

realizations proposed in the literature using FTFN are in the current mode, and there is no voltage-mode filter using FTFN. Utilizing the transpose for FTFN, a VM BPF is obtained by transforming current-mode BPF. Finally, comparison of performance among CM, VM BPFs using the original MCFOA, proposed MCFOA, and CCII- is presented.

Chapter 5 contains conclusions and possible scope for future work.

Chapter 2

Voltage and Current Transfer Function Realizations with Modified Current Feedback Operational Amplifier

Several applications on simulated inductors, simulated capacitors, current-mode filters and voltage-mode filters using modified current-feedback operational amplifier (MCFOA) have been proposed in [7]. The corresponding simulation results are also presented in [7]. In this Chapter, the same implementation of MCFOA as mentioned in [7] is repeated with a different CMOS technology. Two VM filter configurations proposed in [7] using the MCFOA are studied, and their simulation results are compared with their theoretical results. Reasons for the deviations between the simulation results and the theoretical results are also given by analysing the proposed filters using a non-ideal model of MCFOA. The same procedure is also applied to two alternative configurations proposed by Swamy in [25] using the same MCFOA. The four configurations exhibit the same performance as long as the MCFOA is ideal. However, their performances are different when the MCFOA is non-ideal. The comparisons of simulation results among these four configurations are also provided. In addition, the performance of current-mode circuits, which are obtained from transposing the corresponding voltage-mode circuits, is also investigated.

2.1 Implementation of MCFOA

As mentioned in Section 1.3.5, a MCFOA consists of two composite CCII. The implementation of CCII employed in [7] is shown as Figure 1.6. In this thesis, simulations for MCFOA are based on the implementation with IBM 130nm CMOS technology ($V_{THON} = 0.293V$, $V_{THOP} = -0.324V$, $\mu_{ON} = 440cm^2/V * s$, $\mu_{OP} = 94cm^2/V * s$, $T_{OX} = 3.03 nm$) with power supply $V_{DD} = -V_{SS} = 1.5 V$ and $V_b = 800m V$. The schematic is shown in Figure 2.1, and the corresponding block diagram is shown in Figure 2.2. The transistor dimensions, shown in Table 2.1, are the same as published in [7].

Table 2.1: Dimentions of the transistors in Figure 2.1

PMOS Transistors	W(μm)/L(μm)
M_1, M_4 and M_9, M_{10}, M_{11} and M_{12}	1.0/0.25
M_2, M_3, M_5, M_6, M_7 and M_8	2.0/0.25
M_{13} and M_{14}	4.0/0.25
NMOS Transistors	W(μm)/L(μm)
$M_{15}, M_{16}, M_{17}, M_{18}, M_{19}, M_{20}$, M_{21}, M_{22}, M_{23} , and M_{24}	0.5/0.25

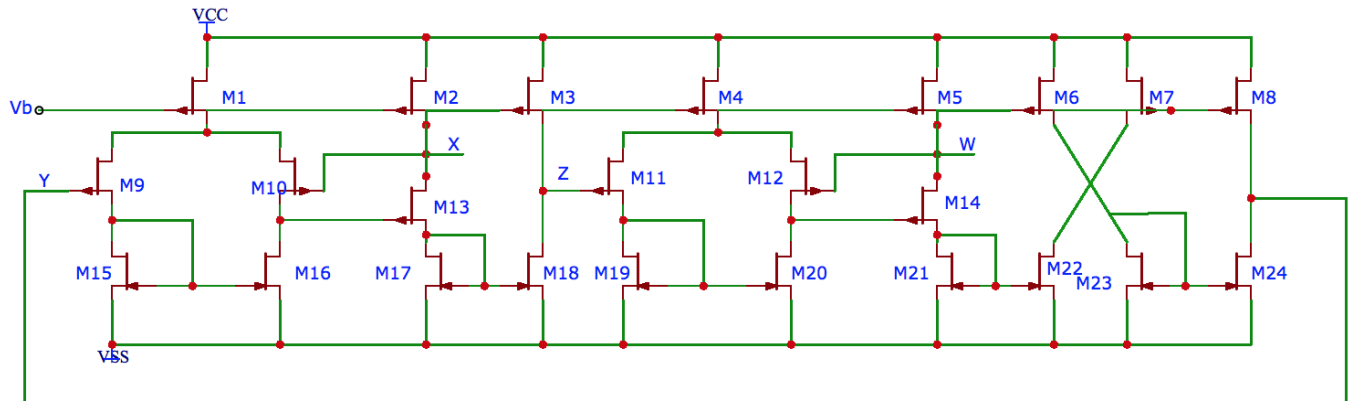


Figure 2.1: MCFOA circuit implemented with CMOS transistors [7]

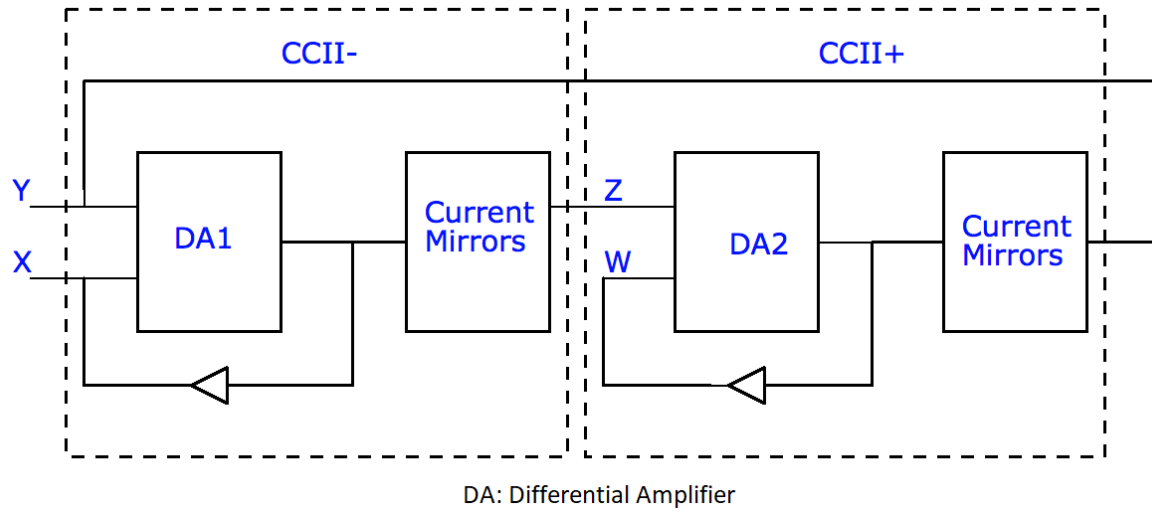


Figure 2.2: Block diagram of the MCFOA proposed in [7]

2.2 Equivalent Circuit Model of MCFOA

Equation (1.8) gives the ideal hybrid matrix of a MCFOA. It assumes that all of the voltage and current gains are unity, the high-impedance input terminals (Y and Z) have infinite impedance, the low-impedance input terminals (X and W) have zero input impedance, and the rest of trans-

elements are all zeros. However, the elements in a practical hybrid matrix of a MCFOA cannot reach the ideal conditions. Suppose the MCFOA has a hybrid matrix

$$\begin{bmatrix} I_z \\ I_Y \\ V_x \\ V_w \end{bmatrix} = \begin{bmatrix} a_{11} & a_{12} & a_{13} & a_{14} \\ a_{21} & a_{22} & a_{23} & a_{24} \\ a_{31} & a_{32} & a_{33} & a_{34} \\ a_{41} & a_{42} & a_{43} & a_{44} \end{bmatrix} \begin{bmatrix} V_z \\ V_Y \\ I_X \\ I_W \end{bmatrix} \quad (2.1)$$

Each element can be determined by simulating the MCFOA circuit. For example, from Equation (2.1), I_z can be represented by the following equation

$$I_z = a_{11}V_z + a_{12}V_Y + a_{13}I_X + a_{14}I_W \quad (2.2)$$

Accordingly, a_{11} can be determined by the following equation

$$a_{11} = \frac{I_z}{V_z} \mid_{V_Y=0, I_X=I_W=0} \quad (2.3)$$

Thus, a_{11} is the conductance at terminal Z. The circuit setup to determine a_{11} is shown in Figure 2.3. The terminal Y is grounded through a 1000F capacitor to make $V_Y=0$, and terminals X and W are open to make $I_X = I_W = 0$. A test voltage source is connected to terminal Z through a 1000F capacitor, and the current through the capacitor is measured to determine a_{11} .

The rest of the elements can be determined by repeating a similar procedure. As a result, the hybrid matrix for the MCFOA at very low frequencies is given by

$$\begin{bmatrix} I_z \\ I_Y \\ V_x \\ V_w \end{bmatrix} = \begin{bmatrix} 17.09 \times 10^{-6} S & 6.483 \times 10^{-6} S & 0.9747 & 14.04 \times 10^{-9} \\ 7.119 \times 10^{-6} S & 19.16 \times 10^{-6} S & 6.948 \times 10^{-9} & -1.013 \\ 12 \times 10^{-12} & 0.9428 & 159.5 \Omega & 0 \Omega \\ 0.9428 & 8.2 \times 10^{-15} & 0 \Omega & 159.5 \Omega \end{bmatrix} \begin{bmatrix} V_z \\ V_Y \\ I_X \\ I_W \end{bmatrix} \quad (2.4)$$

It can be seen that a_{11} and a_{22} are conductances at terminals Z and Y (terminal resistances at terminals Z and Y are $1/a_{11}$ and $1/a_{22}$, respectively), a_{33} and a_{44} are terminal resistances at terminals X and W, a_{13} and a_{24} are current gains, a_{32} and a_{41} are voltage gains. The remaining elements are trans-parameters, and they are small enough to be neglected.

The response of the terminal impedances at terminals X, Y, Z and W are measured at various frequencies and are shown in Figure 2.4 and Figure 2.5, respectively. The frequency responses of the voltage gain and the current gain are shown in Figure 2.6 and Figure 2.7, respectively. Obviously, the terminal impedances, current gains and voltage gains are all functions of frequency. The values shown in Equation (2.4) are the values at low frequencies when parasitic capacitances and inductances are not dominant. Therefore, Equation (2.4) cannot give a full picture of the characteristic of MCFOA, but only the frequency independent part.

The frequency dependent parasitic parameters can be determined by inspecting the frequency responses of terminal resistances as shown in Figure 2.4 and Figure 2.5. It is obvious that the terminals Y and Z are dominated by capacitors at high frequencies, and the terminals X and W are dominated by inductors at high frequencies. Specifically, the parasitic capacitances C_Y and C_Z can be determined by inspecting the frequency response of Z_{inY} and Z_{inZ} shown in Figure 2.4. At low frequencies, Z_{inY} and Z_{inZ} are dominated by R_Y and R_Z , respectively. By using the RC time constant method, C_Y and C_Z can be determined using the equation $f_C = 1/(2\pi RC)$, where f_C is the cut-off frequency. Similarly, the inductances L_X and L_W can be determined by observing the frequency responses of Z_{inX} and Z_{inW} shown in Figure 2.5, and L_X and L_W can be calculated using the equation $f_C = R/(2\pi L)$.

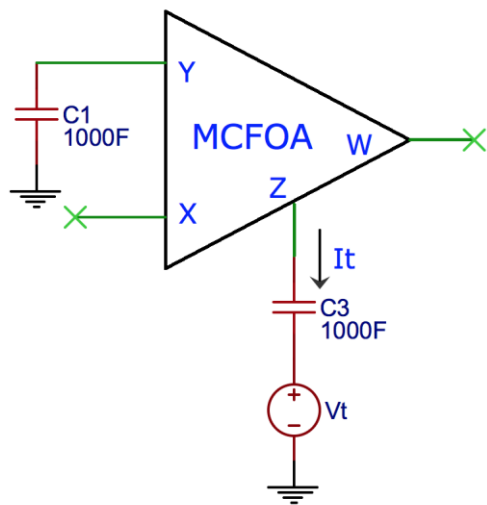


Figure 2.3: Simulation set up to determine a_{11}

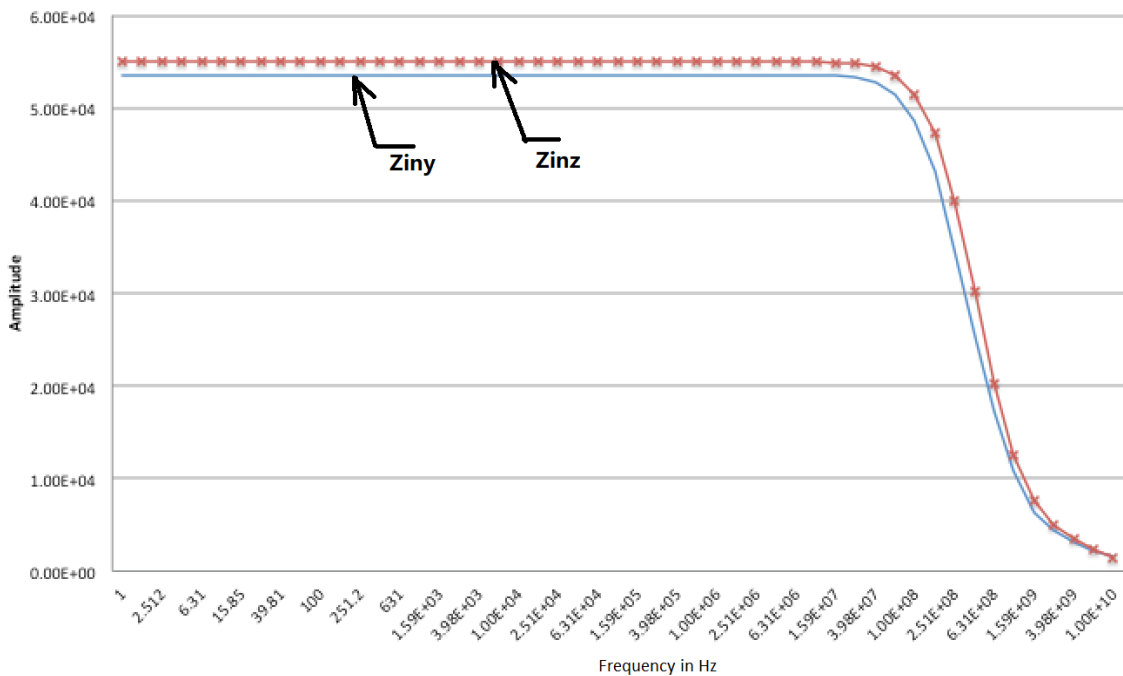


Figure 2.4: MCFOA terminal impedances at terminals Y and Z

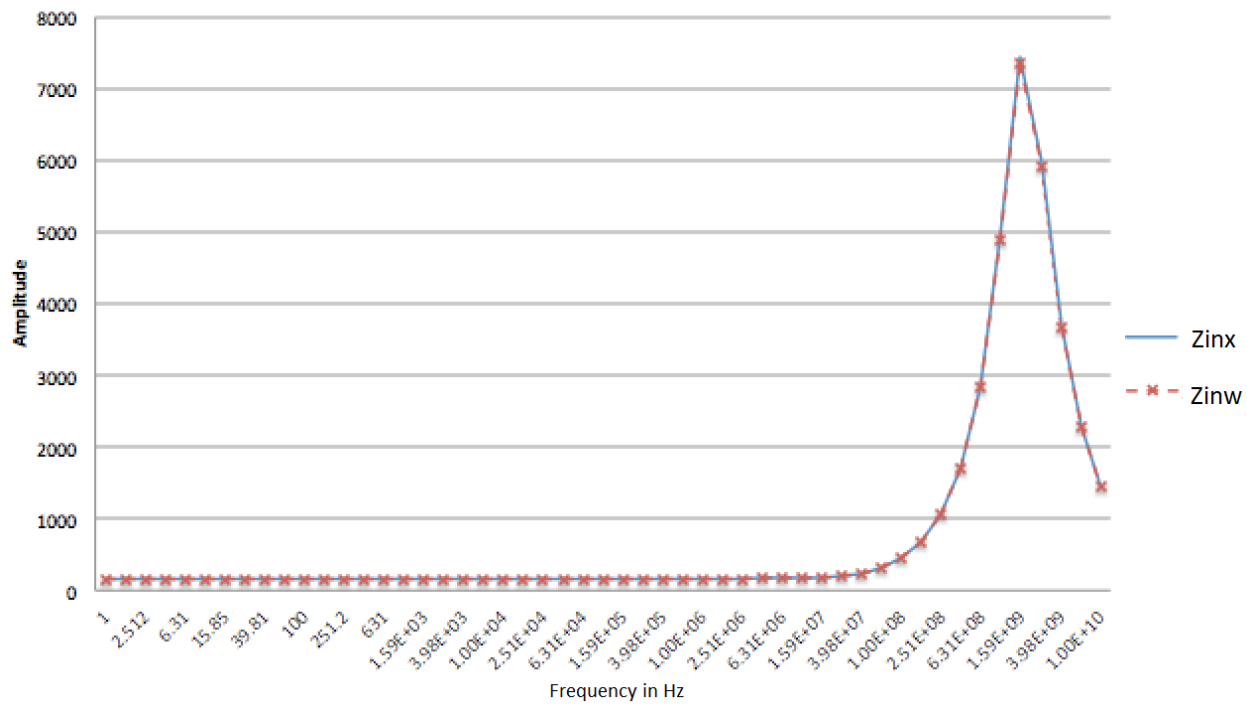


Figure 2.5: MCFOA terminal impedances at terminals X and W

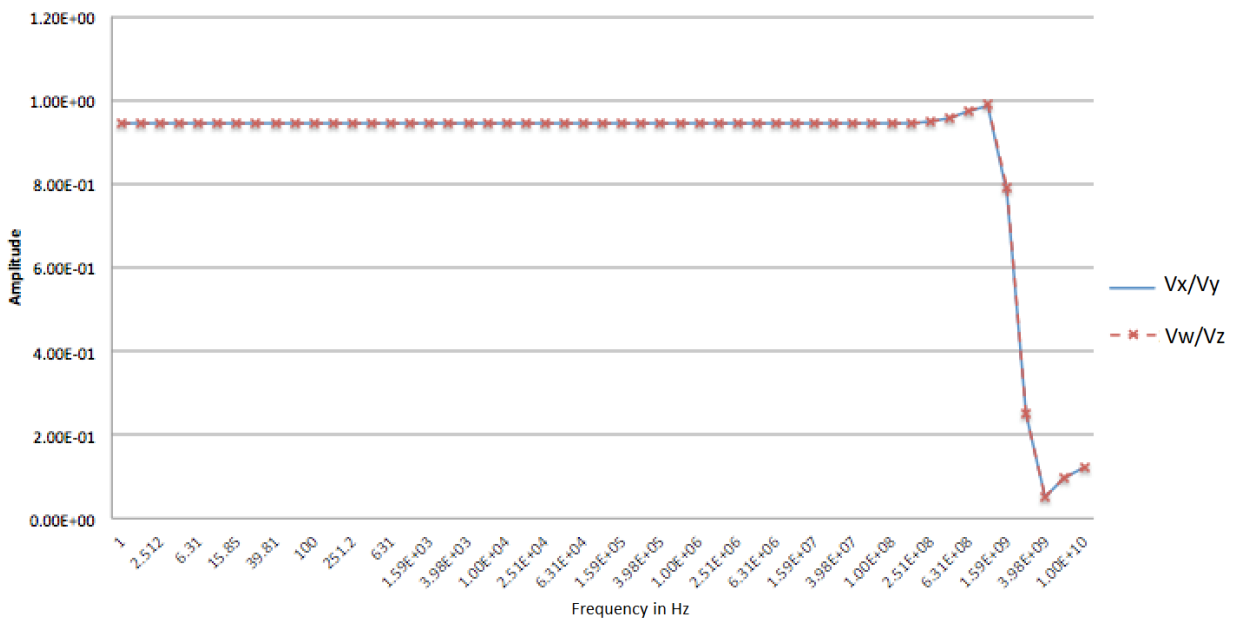


Figure 2.6: The voltage gains of the MCFOA as a function of frequency

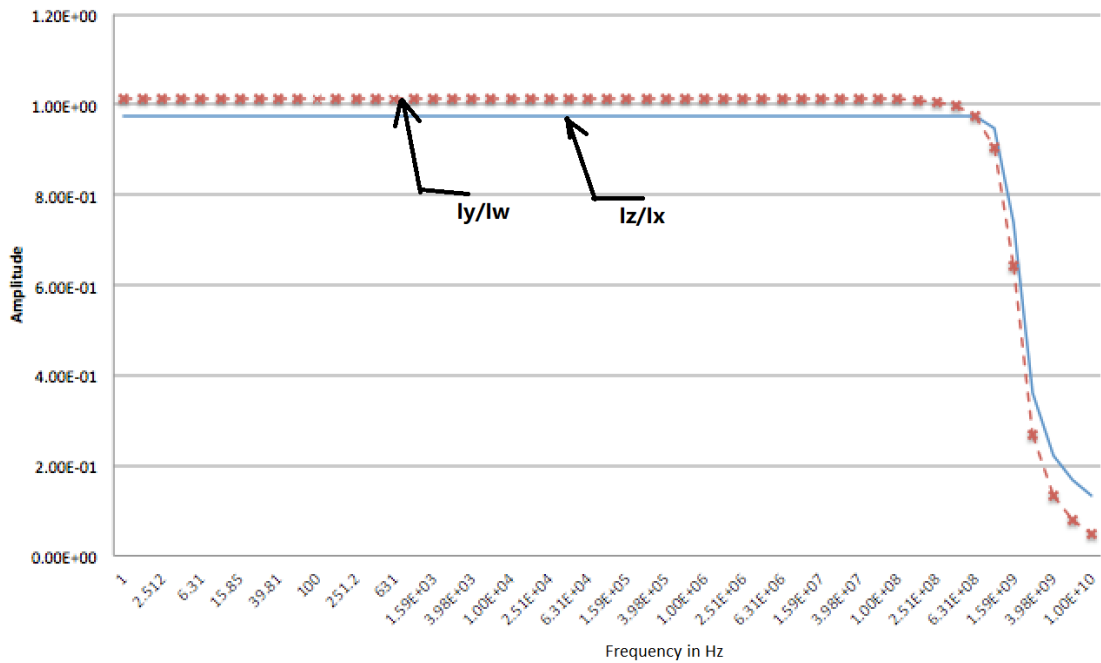


Figure 2.7: The current gains of the MCFOA as a function of frequency

The parasitic parameters of the MCFOA are given in Table 2.2.

Table 2.2: Terminal parasitic parameters of the MCFOA

Terminal	Resistance (ohm)	Capacitance (F)	Inductance (H)
X	159.5	--	699n
Y	53.62K	14×10^{-15}	--
W	159.5	--	699n
Z	55.01K	11×10^{-15}	--

By determining the above parameters, we can obtain a non-ideal MCFOA model, and is as shown in Figure 2.8.

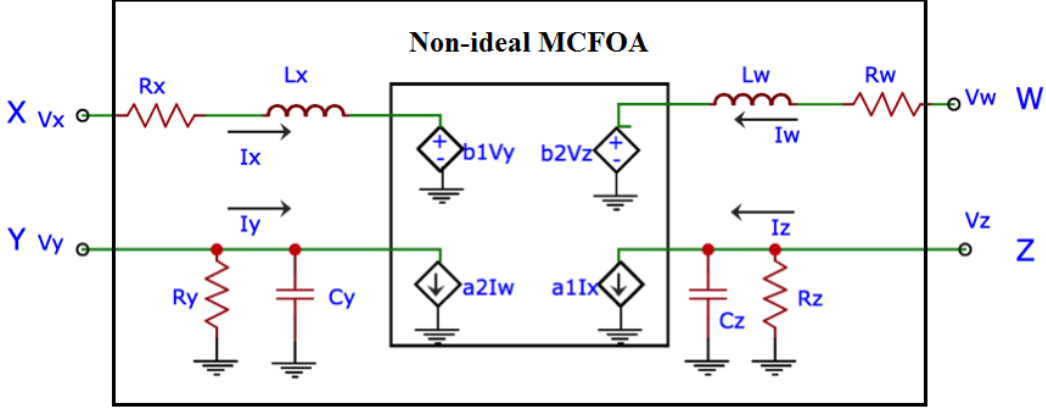


Figure 2.8: MCFOA model taking the parasitics into consideration

MCFOA is designed to receive both current and voltage signals, and is supposed to have two low resistance terminals and two high resistance terminals. The ratio of high impedance terminals to low impedance terminals should be as high as possible to approach the ideal situation. The terminal resistance simulation results show that MCFOA can meet these requirements. From [7], the ratios of both R_Y/R_X and R_Z/R_W are around 170 with 250nm TSMC technology, while the ratios can reach 400 in this design with 130nm IBM technology.

The equations to calculate the terminal resistances are given in [7], and they are as follows:

$$R_Y = \frac{r_{o8}r_{o24}}{r_{o8} + r_{o24}} \quad (2.5)$$

$$R_Z = \frac{r_{o3}r_{o18}}{r_{o3} + r_{o18}} \quad (2.6)$$

$$R_X = \left(\frac{r_{o13} + \frac{r_{o17}}{1 + g_{m17}r_{o17}}}{1 + r_{o13}g_{m13} \left(1 + \frac{r_{o10}}{2}g_{m10} \right)} \right) \mid \mid r_{o2} \approx \frac{2}{g_{m10}g_{m13}r_{o10}} \quad (2.7)$$

$$R_W = \left(\frac{r_{o14} + \frac{r_{o21}}{1 + g_{m21}r_{o21}}}{1 + r_{o14}g_{m14}\left(1 + \frac{r_{o12}}{2}g_{m12}\right)} \right) || r_{o5} \approx \frac{2}{g_{m12}g_{m14}r_{o12}} \quad (2.8)$$

where r_{oi} and g_{mi} are the output resistance and transconductance of the i th CMOS transistor shown in Figure 2.1.

The small signal parameters r_o and g_m can be obtained from AC analysis, and the terminal resistances are calculated by plugging r_o and g_m into these equations. Table 2.3 gives a comparison between the calculation and the simulation results. It shows that the deviations between the calculation and simulation results are very small for the high impedance terminals R_Y and R_Z , while they are comparatively high – about 25% difference – for the low impedance terminals R_X and R_W . The large differences at the low impedance terminals is due to an assumption used when deriving Equations (2.7) and (2.8). The assumption is that V_P , as shown in Figure 2.9 (b), can be seen as a virtual ground. When V_P is virtual ground, it can be calculated by $V_P = \frac{1}{2}(V_{in} - 0) = \frac{1}{2}V_{in}$. That means a small increase of signal current in M_{10} , as shown in Figure 2.9, is accompanied by a small decrease of signal current in M_9 , so that the voltage gain value from the input to both nodes X and Y are equal. This assumption is valid when differential pairs have symmetrical differential outputs as shown in Figure 2.9 (a). Comparatively, differential pairs with a single output, as shown in Figure 2.9 (b), have much lower voltage gain from the input to node X than that from the input to node Y. This is because the diode-connected M_{15} has a smaller resistance than M_{16} has. As a result, the effect from V_X and V_Y to V_P , through r_{o9} and r_{o10} , respectively, do not cancel each other, and V_P is not necessarily to be seen as a virtual ground. In

other words, $V_P \neq \frac{1}{2}(V_{in} - 0) \neq \frac{1}{2}V_{in}$. In reality, V_P is smaller than $\frac{1}{2}V_X$, and this causes deviation between the simulation results and the calculation results.

Table 2.3: Terminal resistances comparison of numerical calculation and circuit simulation results

	Numerical calculation	Circuit simulation
Rx	125 ohm	159.5 ohm
Ry	53.2 K ohm	53.62K ohm
Rw	125 ohm	159.5ohm
Rz	53.6K ohm	55.01K ohm

In conclusion, the high impedance terminals Y and Z can be predicted accurately by Equations (2.5) and (2.6), respectively, while the low impedance terminals X and W can only be approximately predicted by Equations (2.8) and (2.7), respectively, with some deviations.

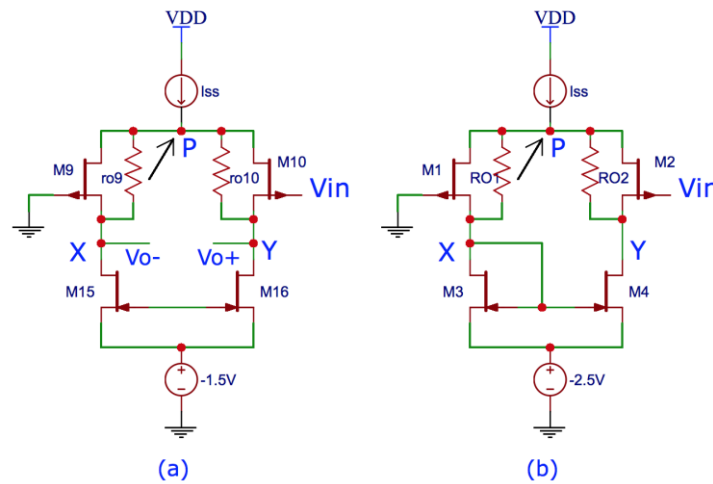


Figure 2.9: Differential input stage with current mirror load
(a) with differential output (b) with single output

2.3 VTF Implementation

2.3.1 Equivalent Configurations

Three universal VM filters and one universal CM filter have been proposed in [7] using MCFOA.

These are: (i) VM filter with single input and triple outputs (SITO), (ii) VM filter with triple inputs and single output (TISO) at the high impedance terminal Y, (iii) VM filter with triple inputs and single output (TISO) at the low impedance terminal X, and (iv) CM filter with single input and triple outputs (SITO). The circuit configurations are shown in Figure 2.10 (a)-(d), respectively.

The voltage mode configurations shown in Figure 2.10 (b) and (c) are thoroughly studied in this thesis.

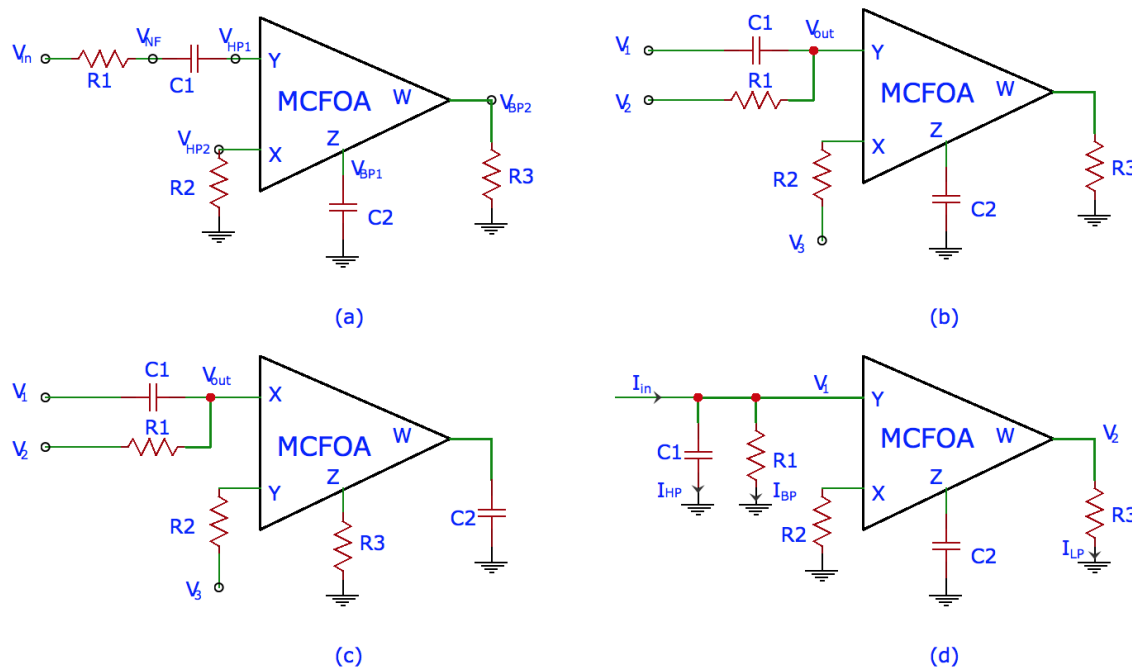


Figure 2.10: Biquad filters proposed in [7]
 (a) VM SITO filter (b) VM TISO filter at terminal Y
 (c) VM TISO filter at terminal X (d) CM SITO filter

In article [25], Swamy showed that given a system function realization using an ideal MCFOA, then three other alternative realizations can be found using the same MCFOA by appropriate port connection between the MCFOA and the external elements. Using this principle, for the circuit of Figure 2.10 (b) repeated as Figure 2.11 (a), three other equivalent configurations can be found and all these are shown in Figure 2.11 (a) – (d). Specifically, circuits of Figure 2.11 (a) and (c), two of the circuits proposed in [7], are the same as the configurations shown in Figure 2.10 (b) and (c), respectively. The circuits of Figure 2.11 (b) and (d) are two new configurations. All these configurations exhibit the same performance under ideal conditions (i.e., MCFOA is ideal) and the output is given by

$$V_{out} = \frac{V_1 s^2 + V_2 \frac{1}{C_1 R_1} s + V_3 \frac{1}{C_1 C_2 R_2 R_3}}{s^2 + \frac{1}{C_1 R_1} s + \frac{1}{C_1 C_2 R_2 R_3}} \quad (2.9)$$

Depending on the applied voltages $V_i, i = 1, 2, 3$, we can realize high pass filter (HPF), low pass filter (LPF), band pass filter (BPF), notch filter (NF) and all pass filter (APF). However, in reality, the non-ideal factors lead to different performances for each of the configurations. Thus, it is felt necessary to evaluate and compare their performances. Detailed discussion is presented in Section 2.3.3 - 2.4.3.

2.3.2 Procedure for the Simulation

The purpose of the following simulation is to evaluate what impact the parasitic components have on the filter performance. The steps used in these simulations are:

- Simulate the circuit of one of the configurations to get the simulation results.
- Use the transfer function of that configuration to get the numerical results.
- Compare the simulation results with the numerical results.

- Analyze how the parasitic parameters influence the behavior of the filters.

The four configurations shown in Figure 2.11 are all TISO universal VM filters. In other words, as mentioned previously, they are able to realize different types of VM filters, such as HPF, LPF, BPF, NF and APF, by manipulating the voltage inputs V_1 , V_2 , and V_3 .

Usually, BPF and NF are the most critical types of filters. Hence, in this thesis we will restrict our discussion to only BPF and NF. In the following section, detailed simulation procedure and discussion are given for the BPF and NF of Figure 2.11 (a). Derivation of BPF and NF transfer functions for the rest of the configurations, are given in Appendices A and B, respectively.

2.3.3 Simulation Results for VM Band-pass Filter

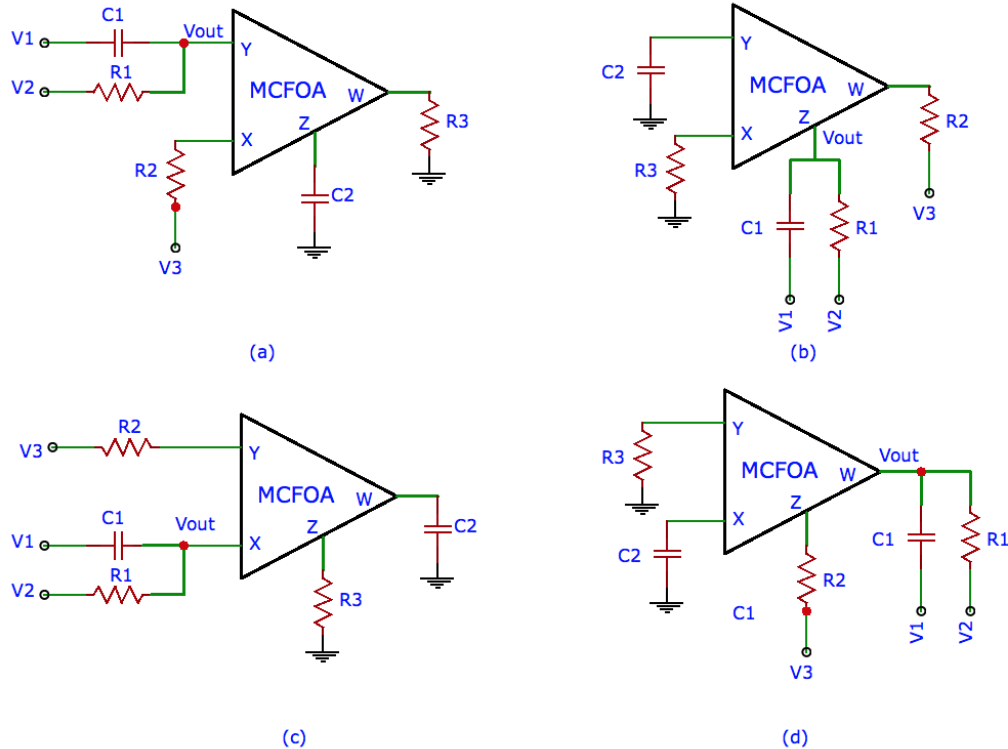


Figure 2.11: VM filter with triple inputs and single output [25]
 (a) configuration (a), (b) configuration (b), (c) configuration (c), (d) configuration (d)

The configuration of Figure 2.11 (a) can realize a BPF with $V_1 = 0$, $V_2 = V_{in}$ and $V_3 = 0$. The schematic is shown in Figure 2.12.

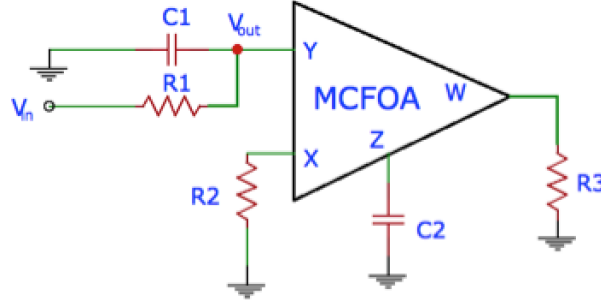


Figure 2.12: Schematic of VM BPF of configuration (a) of Figure 2.11

Assuming MCFOA to be ideal, the VM BPF transfer function is

$$T_{(s)} = \frac{V_{out}}{V_{in}} = \frac{\frac{1}{C_1 R_1} s}{s^2 + \frac{1}{C_1 R_1} s + \frac{1}{C_1 C_2 R_2 R_3}} \quad (2.10)$$

$$\omega_p = \frac{1}{\sqrt{C_1 C_2 R_2 R_3}}, Q_p = R_1 \sqrt{\frac{C_1}{C_2 R_2 R_3}} \quad (2.11)$$

We now replace the ideal MCFOA by the non-ideal MCFOA model shown in Figure 2.8. In this analysis, the parasitic capacitances and inductances are ignored, because their values are much smaller than C_1 and C_2 , and hence can be ignored at low frequencies. Therefor the non-ideal transfer function is

$$T(s) = \frac{V_{out}}{V_{in}} = \frac{(Ry(C2 R2 R3 Rz s + C2 R2 Rw Rz s + C2 R3 Rx Rz s + C2 R w Rx Rz s + R2 R3 + R2 R w + R3 Rx + R w Rx)) / (C1 C2 R1 R2 R3 Ry Rz s^2 + C1 C2 R1 R2 R w Ry Rz s^2 + C1 C2 R1 R3 Rx Ry Rz s^2 + C1 C2 R1 R w Rx Ry Rz s^2 + C1 R1 R2 R3 Ry s + C1 R1 R2 R w Ry s + C1 R1 R3 Rx Ry s + C1 R1 R w Rx Ry s + C2 R1 R2 R3 Rz s + C2 R1 R2 R w Rz s + C2 R1 R3 Rx Rz s + C2 R1 R w Rx Rz s + C2 R2 R3 Ry Rz s + C2 R2 R w Ry Rz s + C2 R3 Rx Ry Rz s + C2 R w Rx Ry Rz s + R1 R2 R3 + R1 R2 R w + R1 R3 Rx + R1 R w Rx + R1 Ry Rz + R2 R3 Ry + R2 R w Ry + R3 Rx Ry + R w Rx Ry)}{(C1 C2 R1 R2 R3 Ry Rz s^2 + C1 C2 R1 R2 R w Ry Rz s^2 + C1 C2 R1 R3 Rx Ry Rz s^2 + C1 C2 R1 R w Rx Ry Rz s^2 + C1 R1 R2 R3 Ry s + C1 R1 R2 R w Ry s + C1 R1 R3 Rx Ry s + C1 R1 R w Rx Ry s + C2 R1 R2 R3 Rz s + C2 R1 R2 R w Rz s + C2 R1 R3 Rx Rz s + C2 R1 R w Rx Rz s + C2 R2 R3 Ry Rz s + C2 R2 R w Ry Rz s + C2 R3 Rx Ry Rz s + C2 R w Rx Ry Rz s + R1 R2 R3 + R1 R2 R w + R1 R3 Rx + R1 R w Rx + R1 Ry Rz + R2 R3 Ry + R2 R w Ry + R3 Rx Ry + R w Rx Ry)} \quad (2.12)$$

The non-ideal transfer function shows that the parasitic resistances not only change the values of ω_p and Q_p , but also move the zero of the BPF from zero to a non-zero frequency.

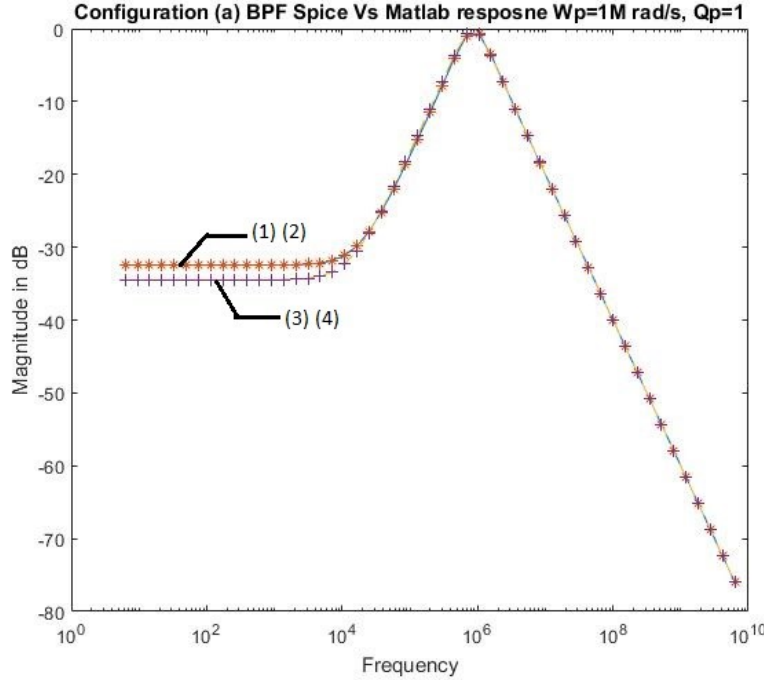


Figure 2.13: Simulation and numerical results for BPF of Figure 2.12 (VM) and Figure 2.17 (CM)

- (1) ‘-’: numerical VM response from Equation (2.12);
- (2) ‘*’: the transposed CM numerical result from Equation (2.18);
- (3) ‘- -’ : VM response from SPICE simulation of Figure 2.12;
- (4) ‘+’: the transposed CM response from SPICE simulation Figure 2.17

Assuming MCFOA to be ideal, let $R_1 = R_2 = R_3 = 1K \text{ Ohm}$ and $C_1 = C_2 = 1nF$; then $\omega_p = 1M \text{ rad/s}$ and $Q_p=1$ according to Equation (2.11). Simulation and numerical results are shown in Figure 2.13, where the simulation results are obtained from SPICE simulation of the circuit shown in Figure 2.12, and the numerical results are obtained using Equation (2.12). Figure 2.13 shows that Equation (2.12) can approximately model the circuit’s behavior. A critical limitation is observed from both the transfer function (2.12) and the frequency response plots. Obviously, the BPF is not actually a BPF, but behaves as a LPF with a high Q. From Equation (2.10), the BPF should have a zero at $\omega = 0 \text{ rad/s}$; however, the non-ideal terminal parasitic resistances move

the zero from origin, and produce a non-zero value at low frequencies. This causes a finite gain at low frequency. From the circuit point of view, this finite gain has an equivalent effect of giving a DC offset at low frequencies. A DC offset is a critical factor that should be avoided in IC design, because it can lead to a malfunction when building a large system.

2.3.4 Simulation Results for VM Notch Filter

The configuration of Figure 2.11 (a) can realize a NF with $V_1 = V_3 = V_{in}, V_2 = 0$. The schematic is shown in Figure 2.14.

Assuming MCFOA to be ideal, the VM NF transfer function is

$$T_{(s)} = \frac{V_{out}}{V_{in}} = \frac{s^2 + \frac{1}{C_1 C_2 R_2 R_3}}{s^2 + \frac{1}{C_1 R_1} s + \frac{1}{C_1 C_2 R_2 R_3}} \quad (2.13)$$

$$\omega_p = \frac{1}{\sqrt{C_1 C_2 R_2 R_3}}, Q_p = R_1 \sqrt{\frac{C_1}{C_2 R_2 R_3}} \quad (2.14)$$

We now replace the ideal MCFOA by the non-ideal MCFOA model shown in Figure 2.8. In this analysis, the parasitic capacitances and inductances are ignored, because their values are much smaller than C_1 and C_2 , and can be ignored at low frequencies. Therefore, the non-ideal transfer function is

$$T(s) = \frac{V_{out}}{V_{in}} = \left(R1 Ry (C1 C2 R2 R3 Rz s^2 + C1 C2 R2 Rw Rz s^2 + C1 C2 R3 Rx Rz s^2 + C1 C2 Rw Rx Rz s^2 + C1 R2 R3 s + C1 R2 Rws + C1 R3 Rx s + C1 Rws Rx s + Rz) \right) / (C1 C2 R1 R2 R3 Ry Rz s^2 + C1 C2 R1 R2 Rws Ry Rz s^2 + C1 C2 R1 R3 Rx Ry Rz s^2 + C1 C2 R1 Rws Rx Ry Rz s^2 + C1 R1 R2 R3 Rys + C1 R1 R2 Rws Rys + C1 R1 R3 Rx Rys + C1 R1 Rws Rx Rys + C2 R1 R2 R3 Rzs + C2 R1 R2 Rws Rzs + C2 R1 R3 Rx Rzs + C2 R1 Rws Rx Rzs + C2 R2 R3 Ry Rzs + C2 R2 Rws Ry Rzs + C2 R3 Rx Ry Rzs + C2 Rws Rx Ry Rzs + R1 R2 R3 + R1 R2 Rws + R1 R3 Rx + R1 Rws Rx + R1 Ry Rz + R2 R3 Ry + R2 Rws Ry + R3 Rx Ry + Rws Rx Ry) \quad (2.15)$$

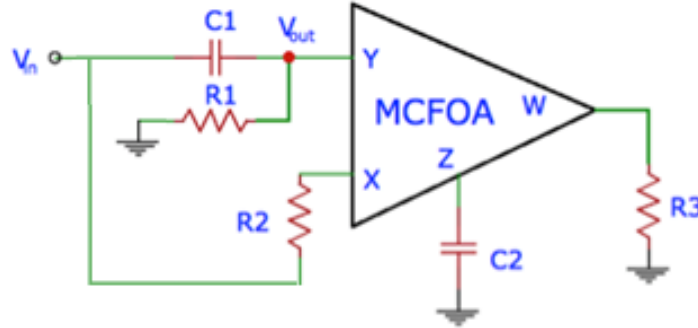


Figure 2.14: Schematic of VM NF of configuration (a) of Figure 2.11

The non-ideal transfer function shows that the parasitic resistances change the values of ω_p and Q_p . In addition, they also make $\omega_z \neq \omega_p$. This will degrade the performance of the NF by decreasing the attenuation at $\omega = \omega_p$.

Assuming MCFOA to be ideal, let $R_1 = R_2 = R_3 = 1K\text{ Ohm}$ and $C_1 = C_2 = 1nF$; then $\omega_p = 1M\text{ rad/s}$ and $Q_p=1$ according to Equation (2.13). Simulation and numerical results are shown in Figure 2.15, where the simulation results are obtained from SPICE simulation of the circuit shown in Figure 2.14, and the numerical results are obtained from Equation (2.15). Figure 2.15 shows that Equation (2.15) can approximately model the circuit's behavior. The VM NF has an attenuation of about 11dB at $\omega = \omega_p$.

In a nutshell, the existence of terminal parasitic resistances also alters the position of the zeros of the other types of filters, which can be seen from finding their transfer functions. In short, there is a non-infinity zero for the low pass filters and a non-zero zero for the high pass filters in their transfer functions. The positions of the zeros are decided by the capacitors C_1 or C_2 and the corresponding terminal parasitic resistances. The above behavior has not been reported yet in the open literature [7, 26-30]. This is an important contribution of the present work. It may be

mentioned in this context that the authors in [31] mentioned the effect of parasitic resistances to the filter high frequency limitations, but did not mention about the low frequencies effects.

In addition, the terminal parasitic resistances also cause deviations of ω_p and Q_p from the design values. How large the deviations are from the ideal values depends on how ‘non-ideal’ the parasitic resistances are. The more ideal the parasitic resistances are, the smaller are the deviations.

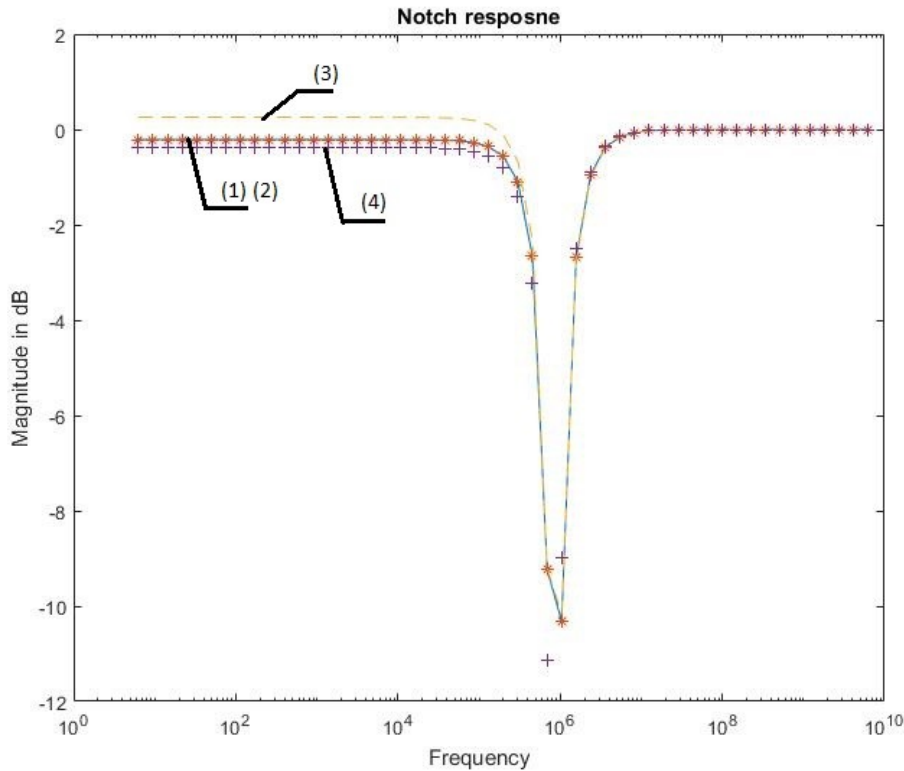


Figure 2.15: Simulation and numerical results for NF of Figure 2.14 (VM) and Figure 2.18 (CM) .

- (1) ‘-’: numerical VM response from Equation (2.15);
- (2) ‘-*’: the transposed CM numerical result from Equation (2.21);
- (3) ‘- -’ : VM response from SPICE simulation of Figure 2.14;
- (4) ‘+’: the transposed CM response from SPICE simulation of Figure 2.18

2.3.5 Performance Comparison of VM Band-pass and Notch Filters

As mentioned earlier, BPF and NF are the most critical types of filters. Therefore, the ω_p and Q_p errors of BPF and NF are tabulated through Table 2.4 to Table 2.7. The schematics for the rest of the three BPFs and the three NFs can be found in Appendices A and B, respectively. The component values are the same as those used in the previous section for $Q_p=1$ and $Q_p=3$.

Table 2.4: $\omega_p=1\text{M rad/s}=159\text{K Hz}$, $Q_p=1$, VM BPF with MCFOA

Configuration	VM			
	ω_p (rad/s)	Q_p	Error_ ω_p (%)	Error_ Q_p (%)
a	843832.365	0.821	-15.617	-17.928
b	868252.597	0.849	-13.175	-15.117
c	1088792.651	0.812	8.879	-18.767
d	1108824.231	0.824	10.882	-17.566

Table 2.5: $\omega_p=1\text{M rad/s}=159\text{K Hz}$, $Q_p=3$, VM BPF with MCFOA

Configuration	VM			
	ω_p (rad/s)	Q_p	Error_ ω_p (%)	Error_ Q_p (%)
a	854364.861	2.366	-14.564	-21.133
b	864507.639	2.407	-13.549	-19.778
c	1045345.187	1.546	4.535	-48.482
d	1053061.065	1.554	5.306	-48.197

Table 2.6: $\omega_P=1M$ rad/s=159K Hz, $Q_P=1$, VM NF with MCFOA

Configuration	VM			
	ω_P (rad/s)	Q_P	Error_ ω_P (%)	Error_ Q_P (%)
a	786153.793	0.947	-21.385	-5.343
b	869020.993	0.869	-13.098	-13.122
c	990505.043	0.898	-0.949	-10.170
d	1015978.45	0.898	1.598	-10.237

Table 2.7: $\omega_P=1M$ rad/s=159K Hz, $Q_P=3$, VM NF with MCFOA

Configuration	VM			
	ω_P (rad/s)	Q_P	Error_ ω_P (%)	Error_ Q_P (%)
a	877201.811	2.477	-12.280	-17.446
b	889891.731	2.482	-11.011	-17.278
c	971668.422	2.192	-2.833	-26.948
d	973851.243	2.193	-2.615	-26.887

By taking a close look at the four configurations shown in Figure 2.11, it can be seen that configurations (a) and (b) are filters that output from the high impedance terminals Y and Z, and configurations (c) and (d) are filters that output from the low impedance terminals X and W. By taking into consideration both the errors of ω_P and Q_P , one finds that the two high impedance

output configurations have very similar performance, and so do the two low impedance output configurations. Specifically,

- For VM BPF $Q_P = 1$, the four configurations exhibit similar performance, where configurations (c) and (d) have a minor advantage over configurations (a) and (b).
- For VM BPF $Q_P = 3$, configurations (a) and (b) have better performance.
- For VM NF $Q_P = 1$, configurations (c) and (d) have better performance.
- For VM NF $Q_P = 3$, all the four configurations have similar performances.

2.4 CTF Implementation

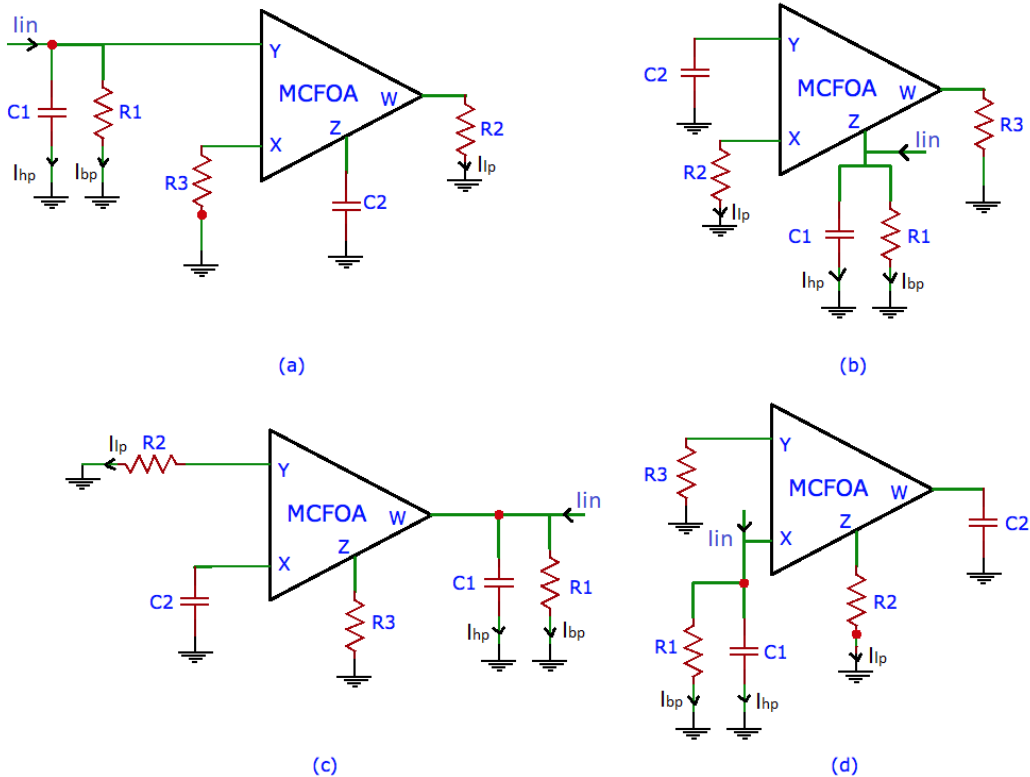


Figure 2.16: Transposed CTF with current input at terminal
 (a) configuration (a), (b) configuration (b), (c) configuration (c), (d) configuration (d)

It has been shown in [25] that by using the principle of transposition, the VM circuits of Figure 2.11 can be converted to CM circuits using the same MCFOA as in Figure 2.11, but by interchanging the passive elements connected to terminals X and W. Then, the TISO VM filters transform to single input and triple outputs (SITO) CM filters. The output voltage V_{out} terminal becomes the input current terminal I_{in} in the CM circuits, and the three input voltage terminals become the output current terminals in the CM circuits, i.e. LP response through R_2 , HP response through C_1 , and BP response through R_1 . The CM filters are shown in Figure 2.16 (a) – (d). The transfer functions of these I_{lp} , I_{hp} and I_{bp} are identical to those of V_{lp} , V_{hp} and V_{bp} except possibly for a multiplicative constant.

Table 2.8 gives the current TFs for the four configurations shown in Figure 2.16. It is seen from this table that the TFs for the CM HPFs, all the configurations are identical, with a similar statement holding for CM BPF TFs. However, it is observed that in the case of LPFs, the TFs for configurations (a) and (c) are identical, and so are for those of configurations (b) and (d), but these two sets of TFs differ by a negative sign.

Table 2.8: Transfer functions of CM filters for the four configurations shown in Figure 2.16 using ideal MCFOA

Configurations	LPF	HPF	HPF
Figure 2.16 (a)	$\frac{1}{C_1 C_2 R_2 R_3} \frac{1}{D(s)}$	$\frac{1}{C_1 R_1} \frac{s}{D(s)}$	$\frac{s^2}{D(s)}$
Figure 2.16 (b)	$-\frac{1}{C_1 C_2 R_2 R_3} \frac{1}{D(s)}$	$\frac{1}{C_1 R_1} \frac{s}{D(s)}$	$\frac{s^2}{D(s)}$
Figure 2.16 (c)	$\frac{1}{C_1 C_2 R_2 R_3} \frac{1}{D(s)}$	$\frac{1}{C_1 R_1} \frac{s}{D(s)}$	$\frac{s^2}{D(s)}$
Figure 2.16 (d)	$-\frac{1}{C_1 C_2 R_2 R_3} \frac{1}{D(s)}$	$\frac{1}{C_1 R_1} \frac{s}{D(s)}$	$\frac{s^2}{D(s)}$

$D(s) = s^2 + \frac{1}{C_1 R_1} s + \frac{1}{C_1 C_2 R_2 R_3}$

2.4.1 Simulation Results for CM Band-pass Filter

The same procedures used in the VM filter simulation are also applied to the transposed CM filter simulation. Detailed analysis and results on the transposed CM BPF corresponding to that shown in Figure 2.16 (a) is given in this section. The derivations of the transfer functions for the BP CM filters of Figure 2.16 (b) – (d) are given in Appendix A.

The schematic of the transposed CM BPF corresponding to configuration (a) of Figure 2.16 is shown in Figure 2.17.

Ideally, the transfer function of the BPF is

$$T_{(s)} = \frac{I_{BP}}{I_{in}} = \frac{\frac{1}{C_1 R_1} s}{s^2 + \frac{1}{C_1 R_1} s + \frac{1}{C_1 C_2 R_2 R_3}} \quad (2.16)$$

$$\omega_P = \frac{1}{\sqrt{C_1 C_2 R_2 R_3}}, Q_P = R_1 \sqrt{\frac{C_1}{C_2 R_2 R_3}} \quad (2.17)$$

which is the same as the VTF of Figure 2.12 given by (2.10).

Considering the non-ideal terminal resistances, the transfer function becomes

$$T(s) = \frac{I_{BP}}{I_{in}} = C_2 R_2 R_3 R_y R_z s + C_2 R_2 R_x R_y R_z s + C_2 R_3 R_w R_y R_z s + C_2 R_w R_x R_v R_z s + R_2 R_3 R_y + R_2 R_x R_y + R_3 R_w R_y + R_w R_x R_y / (C_1 C_2 R_1 R_2 R_3 R_y R_z s^2 + C_1 C_2 R_1 R_2 R_x R_y R_z s^2 + C_1 C_2 R_1 R_3 R_w R_y R_z s^2 + C_1 C_2 R_1 R_w R_x R_y R_z s^2 + C_1 R_1 R_2 R_3 R_y s + C_1 R_1 R_2 R_x R_y s + C_1 R_1 R_3 R_w R_y s + C_1 R_1 R_w R_x R_y s + C_2 R_1 R_2 R_3 R_z s + C_2 R_1 R_2 R_x R_z s + C_2 R_1 R_3 R_w R_z s + C_2 R_1 R_w R_x R_z s + C_2 R_2 R_3 R_y R_z s + C_2 R_2 R_x R_y R_z s + C_2 R_3 R_w R_y R_z s + C_2 R_w R_x R_y R_z s + R_1 R_2 R_3 + R_1 R_2 R_x + R_1 R_3 R_w + R_1 R_w R_x + R_1 R_y R_z + R_2 R_3 R_y + R_2 R_x R_y + R_3 R_w R_y + R_w R_x R_y) \quad (2.18)$$

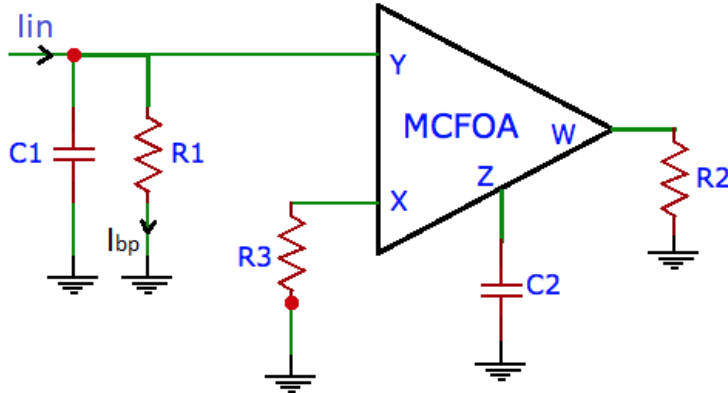


Figure 2.17: Schematic of CM BPF as the transpose of VM BPF of Figure 2.12 and using the same MCFOA as in Figure 2.12

Similar to its VM counterpart, the non-ideal transfer function shows that the parasitic resistances not only change the values of ω_p and Q_p , but also move the zero of the BPF from zero to a non-zero frequency.

With the same settings as for the VM BPF considered in Section 2.3.3, i.e. $R_1 = R_2 = R_3 = 1K\text{ Ohm}$ and $C_1 = C_2 = 1nF$, $\omega_p = 1M\text{ rad/s}$ and $Q_p=1$, simulation and numerical results are shown in Figure 2.13. This shows that Equation (2.18) can approximately model the circuit's behavior at low frequencies. A DC offset is also observed at low frequencies, which makes the BPF not a real BPF but more like a LPF with a high Q.

2.4.2 Simulation Results for CM Notch Filter

As mentioned earlier, CM NF can be realized by combining the outputs I_{lp} and I_{hp} corresponding to the configuration (a) of Figure 2.16; the resulting CM NF is shown in Figure 2.18.

Ideally, the transfer function of the NF is

$$T_{(s)} = \frac{I_{NF}}{I_{in}} = \frac{s^2 + \frac{1}{C_1 C_2 R_2 R_3}}{s^2 + \frac{1}{C_1 R_1} s + \frac{1}{C_1 C_2 R_2 R_3}} \quad (2.19)$$

$$\omega_P = \frac{1}{\sqrt{C_1 C_2 R_2 R_3}}, Q_P = R_1 \sqrt{\frac{C_1}{C_2 R_2 R_3}} \quad (2.20)$$

which is the same as the VTF of Figure 2.14 given by Equation (2.13).

Considering the non-ideal terminal resistances, the transfer function becomes

$$\begin{aligned} T(s) = \frac{I_{NTCH}}{I_{in}} = & \left(R_y R_1 (C_1 C_2 R_2 R_3 R_z s^2 + C_1 C_2 R_2 R_x R_z s^2 + C_1 C_2 R_3 R_w R_z s^2 + C_1 C_2 R_w R_x R_z s^2 \right. \\ & + C_1 R_2 R_3 s + C_1 R_2 R_x s + C_1 R_3 R_w s + C_1 R_w R_x s + R_z) / (C_1 C_2 R_1 R_2 R_3 R_y R_z s^2 \\ & + C_1 C_2 R_1 R_2 R_x R_w R_z s^2 + C_1 C_2 R_1 R_3 R_w R_y R_z s^2 + C_1 C_2 R_1 R_w R_x R_y R_z s^2 \\ & + C_1 R_1 R_2 R_3 R_y s + C_1 R_1 R_2 R_x R_y s + C_1 R_1 R_3 R_w R_y s + C_1 R_1 R_w R_x R_y s \\ & + C_2 R_1 R_2 R_3 R_z s + C_2 R_1 R_2 R_x R_z s + C_2 R_1 R_3 R_w R_z s + C_2 R_1 R_w R_x R_z s \\ & + C_2 R_2 R_3 R_y R_z s + C_2 R_2 R_x R_y R_z s + C_2 R_3 R_w R_y R_z s + C_2 R_w R_x R_y R_z s \\ & + R_1 R_2 R_3 + R_1 R_2 R_x + R_1 R_3 R_w + R_1 R_w R_x + R_1 R_y R_z + R_2 R_3 R_y + R_2 R_x R_y \\ & \left. + R_3 R_w R_y + R_w R_x R_y \right) \end{aligned} \quad (2.21)$$

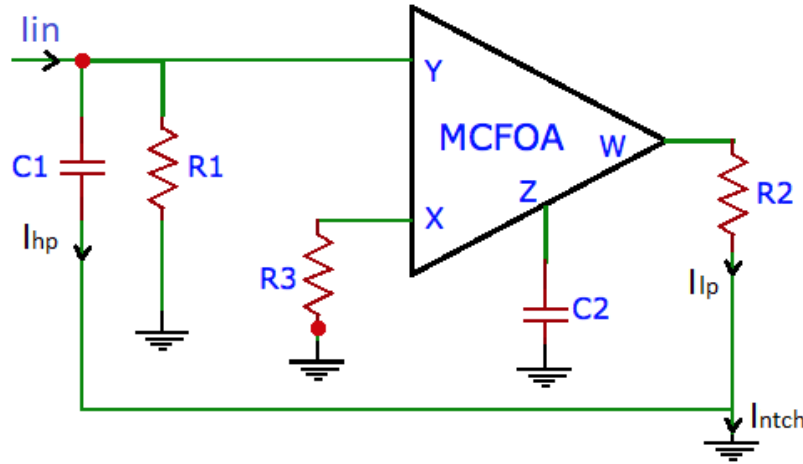


Figure 2.18: Schematic of CM NF as the transpose of VM NF of Figure 2.14

Similar to its VM counterpart, the non-ideal transfer function shows that the parasitic resistances not only change the values of ω_p and Q_p , but also decrease the attenuation at $\omega = \omega_p$.

With the same settings as for the VM NF considered in Section 2.3.4, i.e. $R_1 = R_2 = R_3 = 1K\text{ Ohm}$ and $C_1 = C_2 = 1nF$, $\omega_p = 1M\text{ rad/s}$ and $Q_p=1$, simulation and numerical results are shown in Figure 2.15. This shows that Equation (2.21) can approximately model the circuit's behavior at low frequencies.

2.4.3 Performance Comparison of CM Band-pass and Notch Filters

Similar to its VM counterpart, the ω_p and Q_p errors of the BPF and NF CM filters are tabulated through Table 2.9 to Table 2.12. Details regarding the rest of the three CM BPFs and the CM NFs can be found in Appendices A and B, respectively. The component values are the same as those used in above simulation for $Q_p=1$. The performances for $Q_p=3$ are also compared by letting $R_1=3K\text{ Ohm}$.

Table 2.9: $\omega_p=1M\text{ rad/s}=159K\text{ Hz}$, $Q_p=1$, CM BPF with MCFOA

Configuration	CM			
	ω_p (rad/s)	Q_p	Error_ ω_p (%)	Error_ Q_p (%)
a	843832.365	0.821	-15.617	-17.928
b	868252.597	0.849	-13.175	-15.117
c	1108768.458	0.824	10.877	-17.574
d	1088792.651	0.812	8.879	-18.767

Table 2.10: $\omega_P=1\text{M rad/s}=159\text{K Hz}$, $Q_P=3$, CM BPF with MCFOA

Configuration	CM			
	ω_P (rad/s)	Q_P	Error_ ω_P (%)	Error_ Q_P (%)
a	854364.861	2.366	-14.564	-21.133
b	862962.495	2.386	-13.704	-20.478
c	1053061.065	1.554	5.306	-48.197
d	1045345.187	1.546	4.535	-48.482

Table 2.11: $\omega_P=1\text{M rad/s}=159\text{K Hz}$, $Q_P=1$, CM NF with MCFOA

Configuration	CM			
	ω_P (rad/s)	Q_P	Error_ ω_P (%)	Error_ Q_P (%)
a	826782.812	0.818	-17.322	-18.151
b	--	--	--	--
c	1051711.487	0.902	5.171	-9.793
d	--	--	--	--

Table 2.12: $\omega_P=1\text{M rad/s}=159\text{K Hz}$, $Q_P=3$, CM NF with MCFOA

Configuration	CM			
	ω_P (rad/s)	Q_P	Error_ ω_P (%)	Error_ Q_P (%)
a	808963.946	2.329	-19.104	-22.353
b	--	--	--	--
c	1042790.169	2.250	4.279	-25.000
d	--	--	--	--

Observing the four CM configurations shown in Figure 2.16, one can find that the current input is connected to high impedance terminals in (a) and (b), and to low impedance terminals in (c) and (d).

The above simulation result shows that

- For CM BPF $Q_P = 1$, the four configurations exhibit similar performances, where configurations (c) and (d) have a minor advantage over configurations (a) and (b).
- For CM BPF $Q_P = 3$, configurations (a) and (b) have better performance.
- For CM NF $Q_P = 1$ and $Q_P = 3$, configurations (b) and (d) fail to implement NF. See Appendix B for explanation.
- For CM NF $Q_P = 1$ and $Q_P = 3$, configuration (c) has a better performance.

2.5 Comparison of VTF with its Transposed CTF

2.5.1 Comparison of Transfer Functions

By comparing Equations (2.18) and (2.12) for BPF, and Equations (2.21) and (2.15) for NF, one can see that the CM transfer functions are the same as their VM counterparts if R_2 and R_3 are interchanged. This results from the fact that the passive elements connected to terminals X and W have been interchanged in the transposed CM circuits. Although their symbolic transfer functions are different, their numerical results are the same, due to $R_X = R_W$, and since we have assumed $R_2 = R_3$. Both the CM and VM transfer functions will reach the same ideal transfer function when MCFOA becomes ideal, i.e. $R_X = R_W = 0$ and $R_Y = R_Z = \infty$.

2.5.2 Comparison of Simulation Results

Table 2.13: VM and CM BPF performance comparison

Configurations	Total error of BPF $Q_p=1$				Total error of BPF $Q_p=3$			
	VM		CM		VM		CM	
	Error ω_P (%)	Error Q_P (%)	Error ω_P (%)	Error Q_P (%)	Error ω_P (%)	Error Q_P (%)	Error ω_P (%)	Error Q_P (%)
a	-15.617	-17.928	-15.617	-17.928	-14.564	-21.133	-14.564	-21.133
b	-13.175	-15.117	-13.175	-15.117	-13.549	-19.778	-13.704	-20.478
c	8.879	-18.767	10.877	-17.574	4.535	-48.482	5.306	-48.197
d	10.882	-17.566	8.879	-18.767	5.306	-48.197	4.535	-48.482

Table 2.14: VM and CM NF performance comparison

Configurations	Total error of NF $Q_p=1$				Total error of NF $Q_p=3$			
	VM		CM		VM		CM	
	Error ω_P (%)	Error Q_P (%)	Error ω_P (%)	Error Q_P (%)	Error ω_P (%)	Error Q_P (%)	Error ω_P (%)	Error Q_P (%)
a	-21.385	-5.343	-17.322	-18.151	-12.280	-17.446	-19.104	-22.353
b	-13.098	-13.122	--	--	-11.011	-17.278	--	--
c	-0.949	-10.170	5.171	-9.793	-2.833	-26.948	4.279	-25.000
d	1.598	-10.237	--	--	-2.615	-26.887	--	--

The ‘- -’ and ‘+ +’ symbols shown in Figure 2.13 are the circuit simulation results for VM BPF and the transposed CM BPF, respectively. It indicates that the two responses are very similar. A detailed comparison on ω_p and Q_p is made in Table 2.13.

The results for the BPF confirm the similarity in performance of VM and its transposed CM filters. Some deviations are observed between the performance of VM and CM notch filters.

The detailed comparison results are as follows.

- For all the four BPF configurations, VM and CM exhibit very similar performance.
- For NF configurations (b) and (d), the performance cannot be compared due to the inability to realize CM NF. See Appendix B for explanation.
- For NF configurations (a) and (c), VM has a weak advantage over CM.

2.6 Limitation of MCFOA Based Filters

The VTF and CTF given by Equations (2.10) and (2.16) are used to model the ideal behavior of filters, assuming MCFOA to be ideal. In practice, the non-idealities of MCFOA change the behavior of the filters. Take the circuit shown in Figure 2.12 for example. To realize a VM BPF, the terminal X should be resistive. However, the terminal X becomes more inductive with increase of frequency, according to the non-ideal MCFOA model shown in Figure 2.8, and starts to be dominated by the parasitic inductor at a certain frequency. After that frequency, Equation (2.10) cannot model the behavior of the filter accurately. Therefore, it is necessary to design a filter with Equations (2.10) and (2.16) knowing the limitations of the MCFOA. They mainly result from parasitic parameters and can be categorized in two aspects: frequency limitations and unexpected poles or zeros. More discussions follow.

2.6.1 Frequency Limitations

The first cause of frequency limitation comes from the current gain and voltage gain factors of the MCFOA. This is easy to determine from Figure 2.6 and Figure 2.7. This limitation is caused by

the parasitic capacitances. For simplified analysis, the gains can be modeled as single pole transfer functions, as shown in Equations (2.22) - (2.25). Their gain magnitudes are not ideal, i.e. unity, but very close to unity, and have poles at frequencies greater than 1.3G Hz.

$$\alpha_1 = \frac{0.9747}{s + 10.5838 * 10^9} \quad (2.22)$$

$$\alpha_2 = \frac{1.013}{s + 8.7292 * 10^9} \quad (2.23)$$

$$\beta_1 = \frac{0.9428}{s + 10.946 * 10^9} \quad (2.24)$$

$$\beta_2 = \frac{0.9428}{s + 11.034 * 10^9} \quad (2.25)$$

The second issue regarding frequency limitation is caused by terminal capacitances and inductances, i.e. C_Y and C_Z , L_X and L_W . Their values are given in Table 2.2, and can be determined from frequency responses shown in Figure 2.4 and Figure 2.5. It can be inferred that the parasitic capacitors are dominant for frequencies greater than about 200M Hz at terminals Y and Z, and parasitic inductances are dominant for frequencies greater than about 36M Hz at terminals X and W.

From the above observations, it appears that the frequency limitations of current and voltage gain factors are at much higher frequencies than those due to the terminal parasitic parameters. Therefore, the primary frequency limitations are those resulting from terminal parasitic parameters, and the voltage and current gains can be seen as frequency-independent parameters at lower frequencies.

2.6.2 Effect of Terminal Parasitic Resistances

For frequencies under 36M Hz, all of the frequency-dependent parasitic parameters of MCFOA can be neglected, and all of the terminals exhibit resistive characteristics. However, these terminal resistances still interact with the design capacitances that are connected to these terminals, and produce unexpected zeros or poles in their transfer functions. Consequently, the shapes of their frequency response change accordingly. In summary, the terminal resistances modify the transfer functions in the following ways:

- (a) For a second order HPF, one of the two zeros is moved from the origin to a finite frequency.
- (b) For a second order BPF, the zero is moved from the origin to a finite frequency.
- (c) For a second order NF, the positions of zeros are different from that of the poles.
- (d) Terminal resistances modify the values of ω_p and Q_p from the design values.

2.7 Sensitivity

2.7.1 Sensitivity of VM filters

The transfer function of Figure 2.11 (a) considering non-ideal current gains (α_1 and α_2) and voltage gains (β_1 and β_2) is

$$V_{out} = \frac{V_1 s^2 + V_2 s \frac{1}{R_1 C_1} + V_3 \frac{\alpha_1 \alpha_2 \beta_2}{R_2 R_3 C_1 C_2}}{s^2 + s \frac{1}{R_1 C_1} + \frac{\alpha_1 \alpha_2 \beta_1 \beta_2}{R_2 R_3 C_1 C_2}} \quad (2.26)$$

The rest of the configurations in Figure 2.11 should have different numerators, but they have the exactly same denominator. As a result, they have the same ω_p and Q_P expressions, given by

$$\omega_p = \sqrt{\frac{\alpha_1 \alpha_2 \beta_1 \beta_2}{R_2 R_3 C_1 C_2}} \quad (2.27)$$

$$Q_p = R_1 \sqrt{\frac{\alpha_1 \alpha_2 \beta_1 \beta_2 C_1}{C_2 R_2 R_3}} \quad (2.28)$$

So, the sensitivities of w_p and Q_p with respect to $\alpha_1, \alpha_2, \beta_1$ and β_2 for all VM filters are

$$s_{a1}^\omega = s_{a2}^\omega = s_{b1}^\omega = s_{b2}^\omega = \frac{1}{2} \quad (2.29)$$

$$s_{a1}^Q = s_{a2}^Q = s_{b1}^Q = s_{b2}^Q = \frac{1}{2} \quad (2.30)$$

2.7.2 Sensitivity of CM filters

CM filters have similar results as VM filters. For example, the transfer function considering $\alpha_1, \alpha_2, \beta_1$ and β_2 for BPF of configuration (a) shown in Figure 2.16 is

$$\frac{I_{BP}}{I_{in}} = \frac{s \frac{1}{R_1 C_1}}{s^2 + s \frac{1}{R_1 C_1} + \frac{\alpha_1 \alpha_2 \beta_1 \beta_2}{R_2 R_3 C_1 C_2}} \quad (2.31)$$

The transfer function for the other types of filters, for all the configurations have the same denominator, although their numerators are different. Therefore, their w_p and Q_p can be expressed as

$$\omega_p = \sqrt{\frac{\alpha_1 \alpha_2 \beta_1 \beta_2}{R_2 R_3 C_1 C_2}} \quad (2.32)$$

$$Q_p = R_1 \sqrt{\frac{\alpha_1 \alpha_2 \beta_1 \beta_2 C_1}{C_2 R_2 R_3}} \quad (2.33)$$

And their sensitivities with respect to $\alpha_1, \alpha_2, \beta_1$ and β_2 for all CM filters are

$$s_{a1}^\omega = s_{a2}^\omega = s_{b1}^\omega = s_{b2}^\omega = \frac{1}{2} \quad (2.34)$$

$$s_{a1}^Q = s_{a2}^Q = s_{b1}^Q = s_{b2}^Q = \frac{1}{2} \quad (2.35)$$

2.8 Conclusions

In this chapter, VM filters and CM filters obtained from the associated VM filters by transposition have been implemented using MCFOA published in [7]. The performance of the four equivalent filter configurations have been investigated and compared. The parasitic resistances of MCFOA have been considered in all the filter implementations, and some deviations from ideal performance observed. In particular, the non-ideal terminal resistances change a BPF into a LPF with a high Q. In theory, the deviation can be reduced by making the terminal resistances more ideal. In the next chapter, an improved MCFOA is presented. The performance of filters implemented with the improved MCFOA is also investigated.

Chapter 3

Improved MCFOA

From the results of Chapter 2, we learn that the non-ideal characteristics of an MCFOA bring several issues on the performance of the analog filter. The issues include deviations from the design values of ω_p and Q_p , and undesired frequency responses. All of these drawbacks resulted from non-ideal terminal resistances and the situation can be improved by making them more ideal, i.e., increasing the resistances at terminals Y and Z, and decreasing the resistances at terminals X and W as much as possible. In this chapter, an improved MCFOA is proposed. Some simulations, which have been presented in Chapter 2, are repeated for both the VM and CM BPFs and NFs implemented with the improved MCFOA, and their performance compared with those implemented with the old version of MCFOA.

3.1 Implementation of Improved MCFOA

3.1.1 Decreasing the Resistances at Terminals X and W

Ideally, the terminal resistances at X and W should be zero. In practice, they should be as low as possible. Equations (2.7) and (2.8) in Chapter 2 can be used to approximately estimate the resistances at terminal X and W, respectively. They show that the resistance at terminal X can be reduced by increasing the transconductances g_{m10} and g_{m13} , and the resistance at terminal W can be reduced by increasing the transconductances g_{m12} and g_{m14} . Assuming that all of the transistors work in the saturation region, the drain current I_D is constant and decided only by the overdrive voltage. According to the first order approximation of I_D and g_m , we have

$$I_D = \frac{1}{2} C_{ox} \mu_p \left(\frac{W}{L}\right)_P V_{OV}^2 \quad (3.1)$$

$$g_m = C_{ox} \mu_p \left(\frac{W}{L}\right)_P V_{OV} = \frac{2I_D}{V_{OV}} \quad (3.2)$$

where C_{ox} is the gate oxide capacitance per unit area, μ_p is the charge-carrier effective mobility for PMOS, and the overdrive voltage $V_{OV} = V_{GS} - V_{TH}$, V_{TH} being the threshold voltage of the field-effect transistor (FET). It is the minimum gate-to-source voltage required to create a conducting path between the drain and source terminals.

Thus, g_m can be increased by reducing the overdrive voltage V_{OV} , and V_{OV} can be reduced by increasing the aspect ratios of $\frac{W}{L}$ when bias current I_D is constant. Theoretically, V_{OV} should be larger than 100mV to keep the transistors in the strong inversion mode. Otherwise, the transistors will work in the weak inversion mode, and the square-law given by Equation (3.1) loses its accuracy to predict the behavior of the transistors. With the above considerations, the aspect ratios of some transistors are adjusted, and the overdrive voltages V_{OV} of all the transistors are kept larger than 100mV all the time.

The schematic of the old version of MCFOA is shown in Figure 3.1. Table 3.1 shows the aspect ratio changes of some transistors.

Table 3.1: Aspect ratio change of some transistors

Transistors with aspect ratio change	Old	New
PMOS Transistors	$W(\mu\text{m})/L(\mu\text{m})$	$W(\mu\text{m})/L(\mu\text{m})$
M_9, M_{10}, M_{11} and M_{12}	1.0/0.25	2.0/0.25
M_{13} and M_{14}	4.0/0.25	10.0/0.25

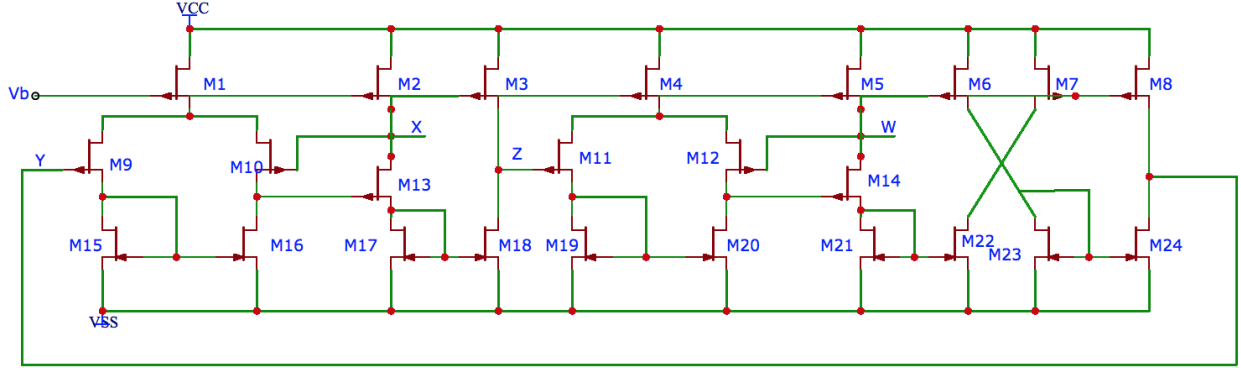


Figure 3.1: Schematic of the old version of MCFOA

3.1.2 Increasing the Resistances at Terminals Y and Z

The resistances at terminals Y and Z can be calculated from Equations (2.5) and (2.6), respectively. They show that the resistances are equal to the output resistances of the PMOS current mirror and the NMOS current mirror in parallel. As a result, their resistances can be increased through enhancing the output resistances of the current mirrors. There are several types of current mirrors in CMOS technology [32]: (i) simple current mirror, (ii) cascode current mirror, (iii) high-swing cascode current mirror, i.e. modified current mirror, (iv) self-biased cascode current mirror and (v) Wilson current mirror. The choice of the current mirror basically depends on the design requirements, such as linear current gain, range of voltage swing, bias voltage, output impedance and frequency response. The performance of the five types of current mirror are compared in the following section [32, 33].

3.1.2.1 Simple Current Mirror

Current mirrors can be seen as current sources, and they should have the same characteristic as current sources, such as zero input impedance, infinite output impedance, and output current linearly related to the input current, i.e. $i_{out} = Ai_{in}$. Figure 3.2 shows a simple current mirror.

Assume that all of the transistors in this section are identical with threshold voltage V_{TH} , overdrive voltage V_{OV} , transconductance g_m and drain-source resistance r_{ds} . The characteristics of the simple current mirror can be summarized by inspecting the circuit [32], [33]:

- Minimum input voltage is $V_{MIN(in)}=V_{TH} + V_{OV}$
- Minimum output voltage is $V_{MIN(out)}=V_{OV}$
- Input resistance is $R_{in} \approx \frac{1}{g_m}$
- Output resistance is $R_{out} = r_{ds}$

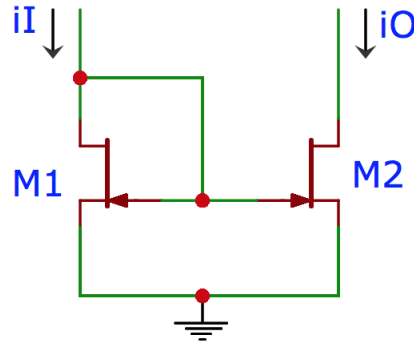


Figure 3.2: Simple current mirror

3.1.2.2 Cascode Current Mirror

Cascode current mirror, shown in Figure 3.3, has the following characteristics [32], [33]:

- Minimum input voltage is $V_{MIN(in)}=V_{TH} + 2V_{OV}$
- Minimum output voltage is $V_{MIN(out)}=2(V_{TH} + V_{OV})$
- Input resistance is $R_{in} \approx \frac{2}{g_m}$
- Output resistance is $R_{out} = r_{ds4} + r_{ds2} + g_m r_{ds4} r_{ds2} \approx g_m r_{ds}^2$

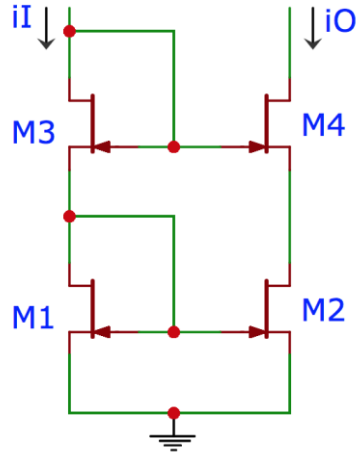


Figure 3.3: Cascode Current Mirror

3.1.2.3 High-Swing Cascode Current Mirror

Figure 3.4 shows the schematic of a high-swing cascode current mirror. It is obvious that the high-swing cascode current mirror has a structure similar to that of a cascode current mirror. The diode connection of M_1 is not to the drain of M_1 , but to that of M_3 . The characteristics of a high-swing cascode current mirror are [32], [33]:

- Minimum input voltage is $V_{MIN(in)} = V_{TH} + V_{OV}$
- Minimum output voltage is $V_{MIN(out)} = 2V_{OV}$
- Input resistance is $R_{in} = \frac{r_{ds4} + r_{ds2} + r_{ds2}g_{m4}r_{ds4}}{g_{m2}r_{ds2}(1+g_{m4}r_{ds4})} \approx \frac{1}{g_m}$
- Output resistance is $R_{out} = r_{ds4} + r_{ds2} + g_{m4}r_{ds4}r_{ds2} \approx g_m r_{ds}^2$

3.1.2.4 Self-Biased Cascode Current Mirror

The self-biased cascode current mirror, as shown in Figure 3.5, is improved based on a high-swing cascode current mirror. The bias voltage of high-swing cascode current mirror is not provided by an external voltage source, but through a resistor in its circuit. The characteristics of a self-biased cascode current mirror are [32], [33]:

- Minimum input voltage is $V_{MIN(in)} = V_{TH} + 2V_{OV}$
- Minimum output voltage is $V_{MIN(out)} = 2V_{OV}$
- Input resistance is $R_{in} = \frac{R + r_{ds1} + r_{ds3} + r_{ds1}g_{m3}r_{ds3} + g_{m1}r_{ds1}g_{m3}r_{ds3}R}{1 + g_{m3}r_{ds3} + g_{m1}r_{ds1}g_{m3}r_{ds3} + g_{m1}r_{ds1}} \approx \frac{1}{g_m} + R$
- Output resistance is $R_{out} = r_{ds4} + r_{ds2} + g_{m4}r_{ds4}r_{ds2} \approx g_m r_{ds}^2$

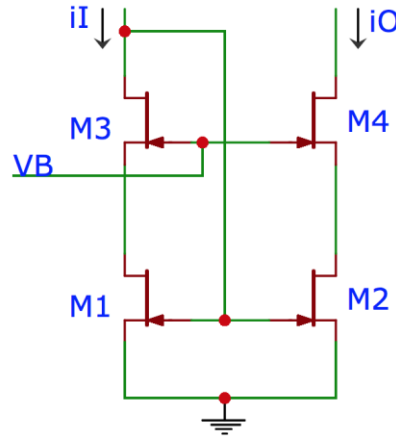


Figure 3.4: High-swing cascode current mirror

3.1.2.5 Wilson Current Mirror

The Wilson current mirror was first used in BJT circuit to make a precise copy of the output current from the input current. Figure 3.6 shows the CMOS version of the Wilson current mirror. The characteristics of the Wilson current mirror are [32], [33]:

- Minimum input voltage is $V_{MIN(in)} = 2(V_{TH} + V_{OV})$
- Minimum output voltage is $V_{MIN(out)} = V_{TH} + 2V_{OV}$
- Input resistance is $R_{in} = \frac{g_{m2} + g_{m3}}{g_{m1}g_{m3}} = \frac{1}{g_m}$
- Output resistance is $R_{out} = r_{ds3} + r_{ds2}\left(\frac{1+g_{m3}r_{ds2}+g_{m1}r_{ds1}g_{m3}r_{ds3}}{1+g_{m2}r_{ds2}}\right) \approx \frac{g_{m1}r_{ds1}g_{m3}r_{ds3}}{g_{m2}} = g_m r_{ds}^2$

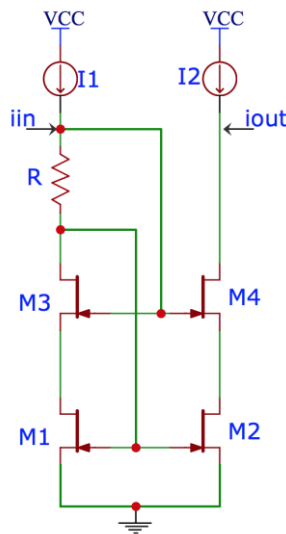


Figure 3.5: Self-biased cascode current mirror

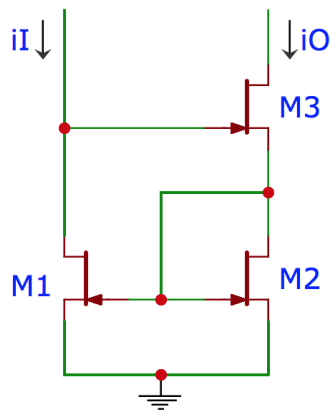


Figure 3.6: Wilson current mirror

In a nutshell, four of the five types of the current mirror have similar level of output resistances. Any one of them can bring a similar enhancement for the output impedances. However, their minimum input and output voltages are different. Considering the small rail-to-rail voltage in this design, the current mirror with the maximum input and output swing will be chosen for the current mirror load, namely, the wide output swing cascode current mirror. The cascode current mirror will be adopted for the implementation of current source.

3.1.3 Choice of the Current Mirror to Enhance the Resistances at Terminals

Y and Z

The current mirrors used in the MCFOA proposed by [7] are all simple current mirrors. In our improvement, the main interest is on the AC small signal and how to eliminate the side effect caused by terminal resistances. Therefore, the current mirrors are adjusted to increase the terminal resistances with $-1.5V - +1.5V$ rail-to-rail voltage.

From the block diagram shown in Figure 2.2, there are basically two functions realized in MCFOA, differential amplifiers (DA) and current mirrors. The output resistances at terminals Y and Z are primarily decided by the output resistances of the current mirrors. In other words, the resistances at terminal Y and Z can be enhanced by increasing the output resistances of the current mirrors. After comparing the performance of the five types of current mirrors theoretically and also through SPICE simulations, it was found that combining cascode current mirror source and modified cascode current mirror load can meet the requirement of output resistance enhancement, and make all the transistors work in the saturation region with $\pm 1.5V$ power supply. Therefore, all the current mirrors, as shown in Figure 2.2, are replaced by cascode current mirrors and modified cascode current mirrors, which are shown in Figure 3.7 [34]. Specifically, the PMOS current mirrors that

provide the biasing function are substituted by cascode current mirrors (as shown in Figure 3.7(a)), and the NMOS current mirrors are substituted by modified current mirrors (as shown in Figure 3.7 (b)). I_{REF} in Figure 3.7 (b) is the bias current derived from in Figure 3.7 (a), where V_a and V_b are the bias voltages.

Figure 3.7 (b) shows that the modified current mirrors have the same topology as cascode current mirrors, but connect the gate of M_{17} to the drain of M_{103} . Now the problem is as to how to choose the bias voltages V_a , V_b and V_c to make both M_{17} and M_{103} to be in the saturation mode. To keep M_{17} and M_{103} remain in saturation, the following two equations should be satisfied:

$$V_X - V_{TH17} \leq V_c - V_{GS103} \quad (3.3)$$

$$V_c - V_X \leq V_{TH103} \quad (3.4)$$

So, $V_X - V_{TH17} + V_{GS103} \leq V_c \leq V_X + V_{TH103}$. A solution exists for this inequality only when $V_X - V_{TH17} + V_{GS103} \leq V_X + V_{TH103}$, which is $V_{GS103} - V_{TH103} \leq V_{TH17}$. Therefore, we need make V_{ov} of M_{103} smaller than the threshold voltage of M_{17} . From Equation (3.1), it is seen that V_{ov} can be reduced by either increasing the W/L ratio of M_{103} or by reducing the bias current I_D (I_{REF} of Figure 3.7 (c)). Here we choose to decrease the bias current by increasing the bias voltage of V_a on PMOS transistors, and keeping the aspect ratios of the transistors unchanged. The bias voltages are determined empirically to make all the transistors to work in the saturation region, and their final values are $V_a = 940m\text{V}$, $V_b = 700m\text{V}$, and $V_c = 670m\text{V}$. The new current mirror schematics are shown in Figure 3.7 (c).

Similar modification on current mirrors could also be applied to DA sub-block, i.e. replace the biasing current mirror with the circuit in Figure 3.7 (a), and replace the current mirror load with Figure 3.7 (b). Theoretically, the gain of the DA will increase with the cascode current mirror and

the modified cascode current mirror load, which will make the voltage gain (β_1 and β_2) more ideal, i.e. make V_X or V_W more close to V_Y or V_Z . This change is not included in the current work, and could be part of future research.

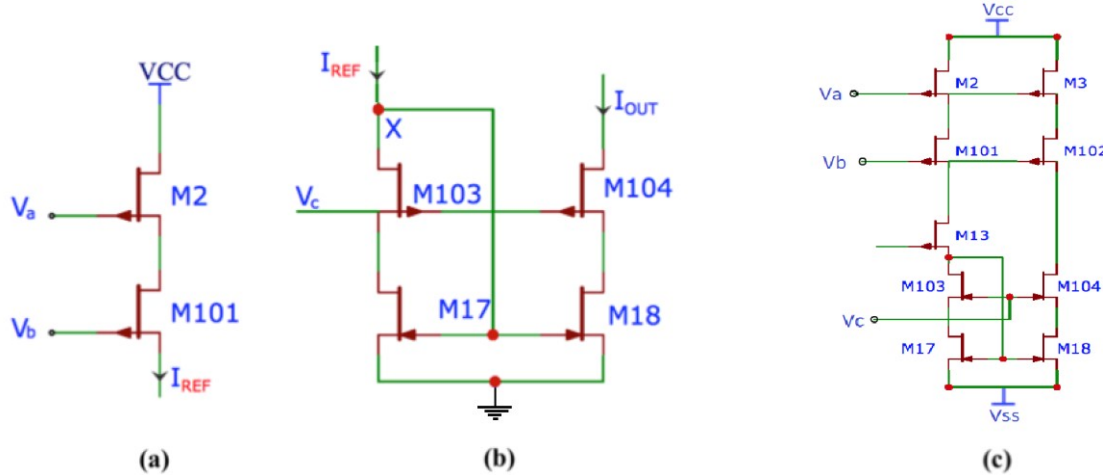


Figure 3.7: Cascade current mirror used in the improved MCFOA
 (a) Cascode current mirror (b) Modified cascode current mirror load
 (c) Schematic of new current mirrors

According to the above discussion, the schematic of the improved MCFOA with the cascode current-mirror loads is shown in Figure 3.8.

Table 3.2 shows the aspect ratio of the newly added transistors.

Table 3.2: Aspect ratios of new added transistors

PMOS Transistors	W(μm)/L(μm)
$M_{101}, M_{102}, M_{105}, M_{106}, M_{109}, M_{110}$	2/0.25
NMOS Transistors	
$M_{103}, M_{104}, M_{107}, M_{108}, M_{111}, M_{112}$	0.5/0.25

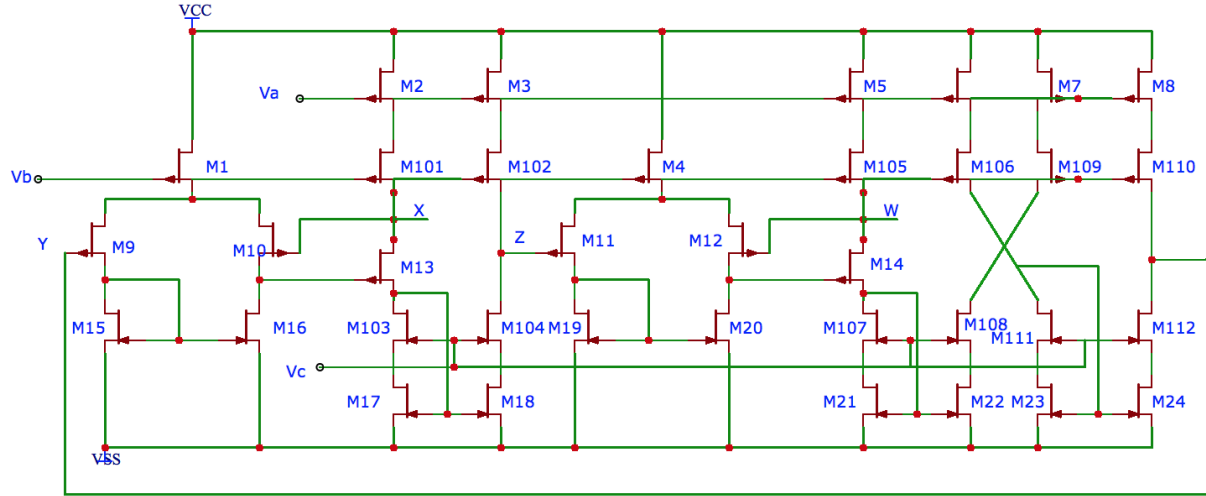


Figure 3.8: The schematics of the improved MCFOA

3.2 Parasitic Parameters of Improved MCFOA

The method to measure the terminal parasitic parameters has been described in Section 2.2. By using the same method, the terminal resistances, capacitances and inductances of the improved MCFOA can be determined. The frequency responses of the resistances at terminals X and W are shown in Figure 3.9, and that at terminals Y and Z are shown in Figure 3.10. The current and voltage gains are shown in Figure 3.11 and Figure 3.12, respectively. Table 3.3 gives the terminal parasitic parameters of both the old MCFOA (of Chapter 2) and the improved MCFOA. The table shows that the low resistance terminals have moderate reductions, whereas the high resistance terminals have dramatic enhancements. However, the enhancement is different at terminals Y and Z. The resistance at terminal Y is almost twice that at terminal Z. It also shows that the improvement on terminal resistances is at the price of increasing the terminal capacitances and inductances. Table 3.4 gives the bandwidth comparison between the improved and old MCFOA.

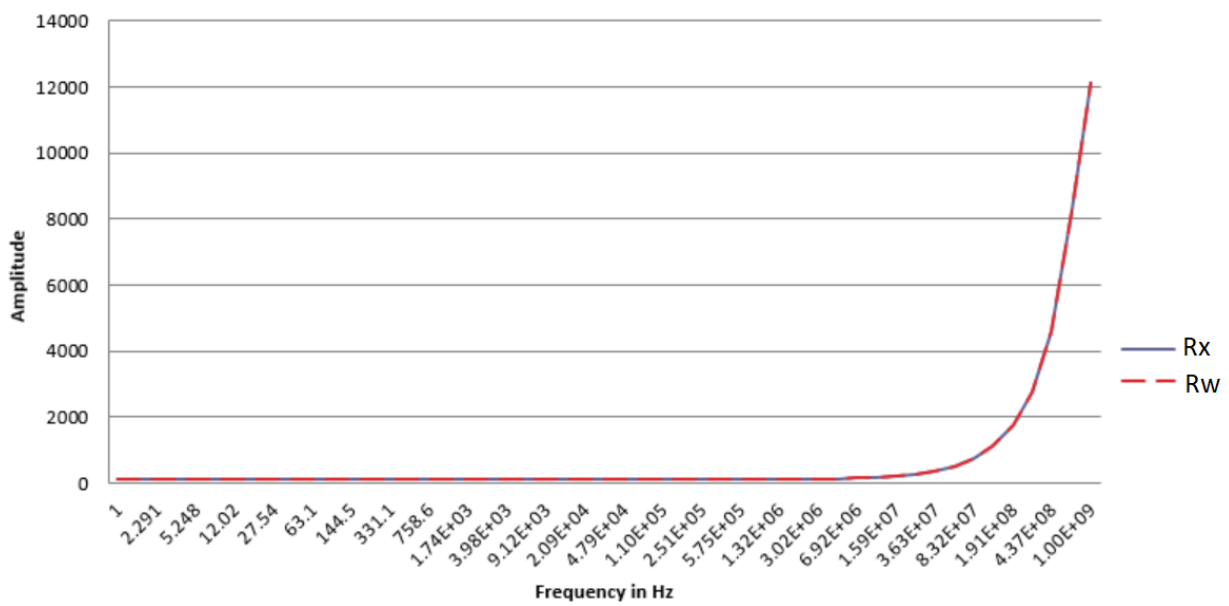


Figure 3.9: Terminal resistances at terminals X and W of the improved MCFOA

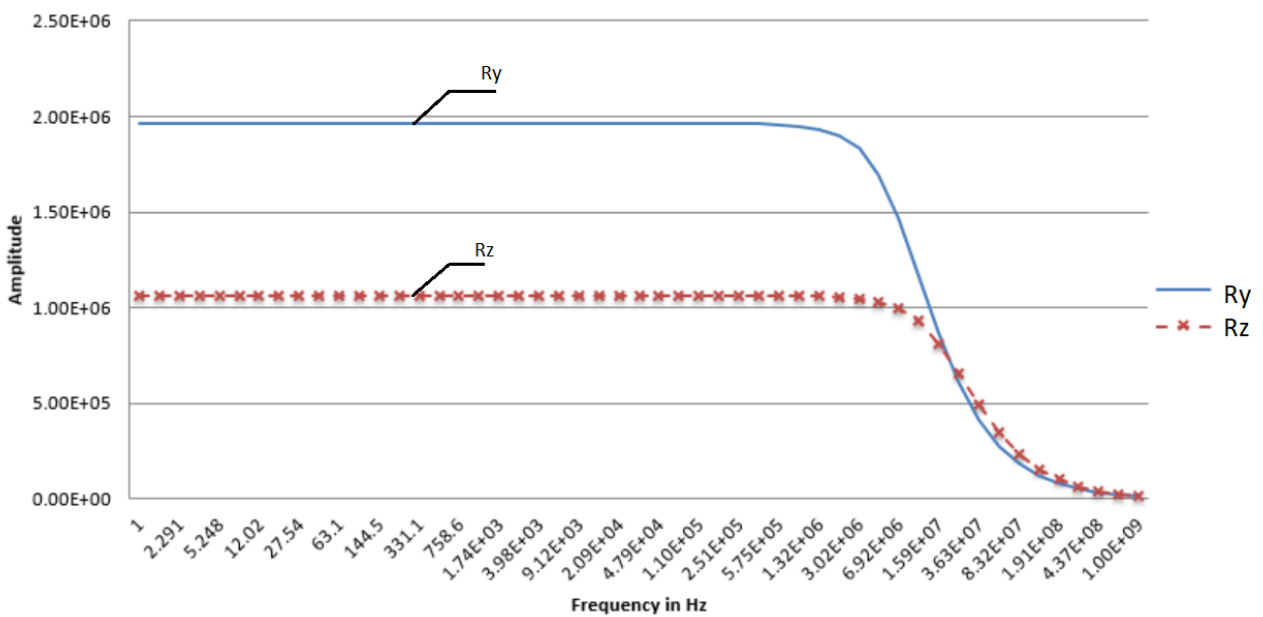


Figure 3.10: Terminal resistances at terminals Y and Z of the improved MCFOA

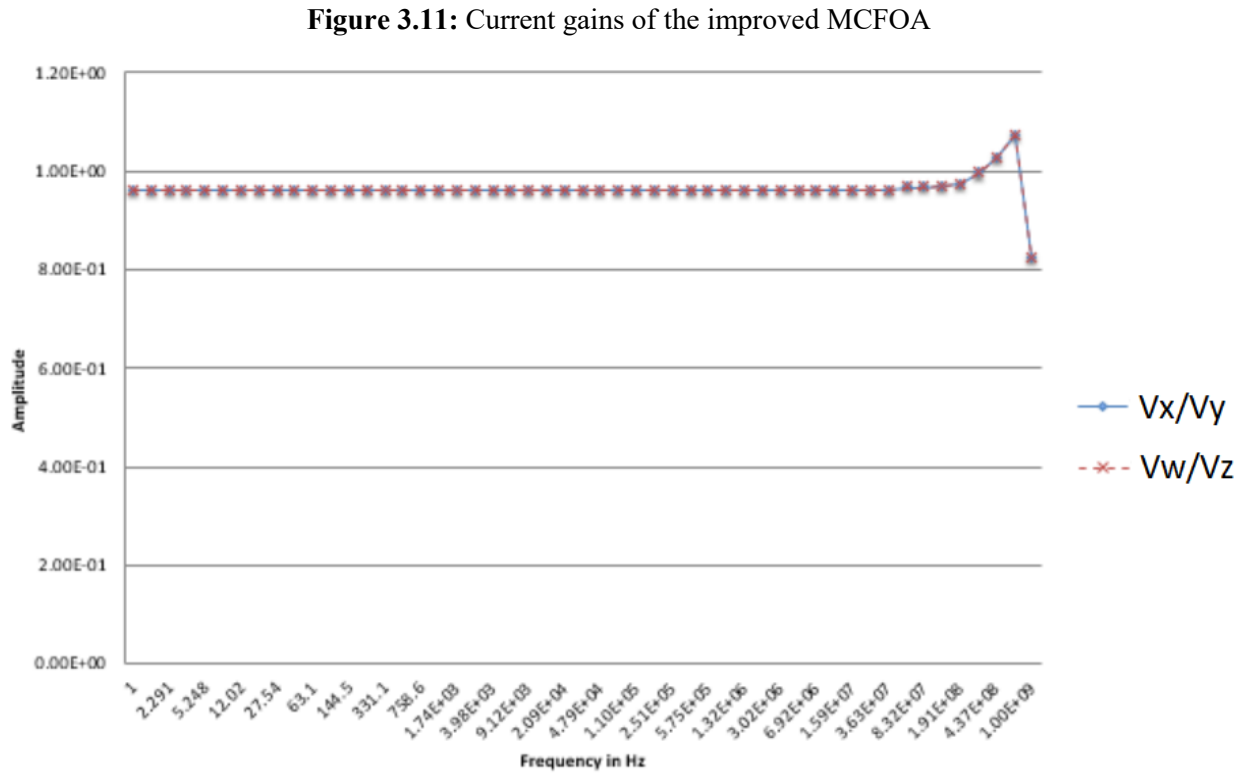
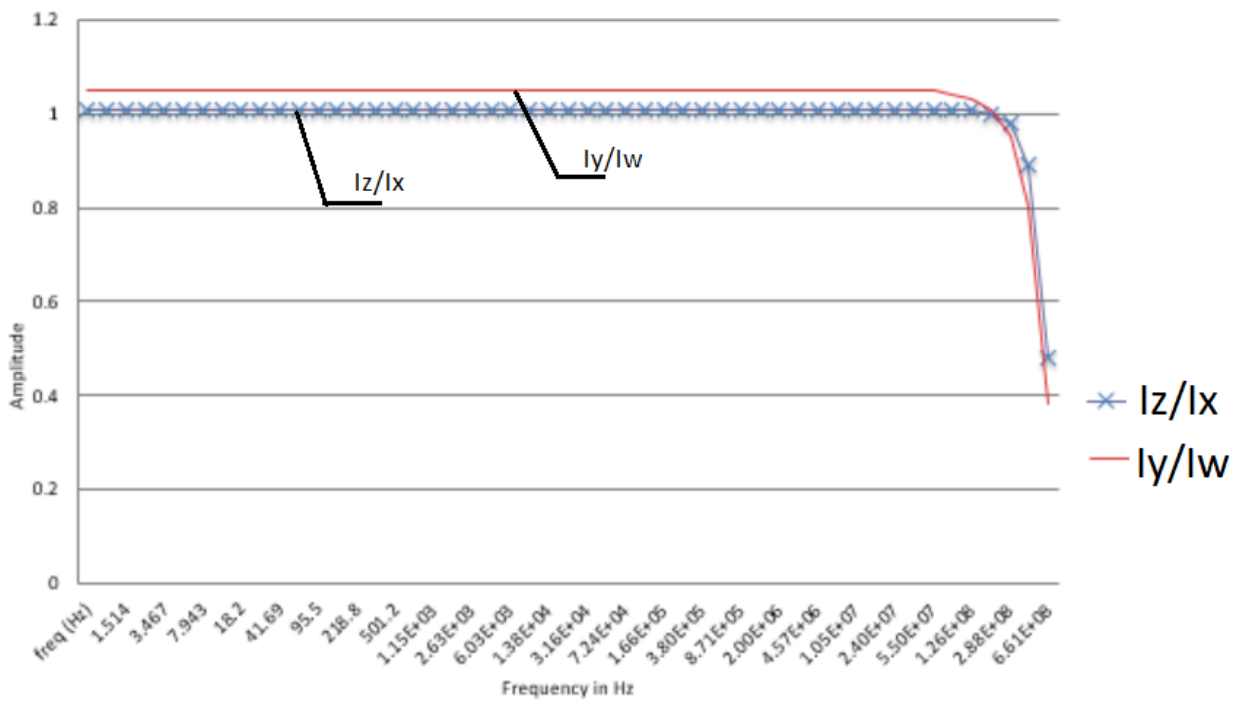


Table 3.3: Comparison of the parasitic parameters of the improved and old MCFOA

	New	Old
R_X	131.4 ohm	159.5 ohm
R_W	131.4 ohm	159.5 ohm
R_Y	1.962M ohm	53.62K ohm
R_Z	1.061M ohm	55.01K ohm
C_Y	105×10^{-15} F	14×10^{-15} F
C_Z	200×10^{-15} F	11×10^{-15} F
L_X	1.45μ H	$699n$ H
L_W	1.45μ H	$699n$ H

Table 3.4: Comparison of the bandwidth of the improved and old MCFOA

	New (Hz)	Old (Hz)
R_X	14.7M	36.31M
R_W	14.7M	36.31M
R_Y	7.947M	212.8M
R_Z	19.17M	262M
I_z/I_x	1.128G	1.685G
I_y/I_w	838.9M	1.39G
V_x/V_y	1.261G	1.73G
V_w/V_z	1.261G	1.757G

The hybrid matrix of the improved MCFOA is

$$\begin{bmatrix} I_Z \\ I_Y \\ V_X \\ V_W \end{bmatrix} = \begin{bmatrix} 0.62 * 10^{-6}S & 0S & 1.01 & 0 \\ 0S & 0.51 * 10^{-6}S & 0 & -1.051 \\ 0 & 0.9627 & 131.40\text{Ohm} & 0\text{Ohm} \\ 0.9627 & 0 & 0\text{Ohm} & 131.40\text{Ohm} \end{bmatrix} \begin{bmatrix} V_Z \\ V_Y \\ I_X \\ I_W \end{bmatrix} \quad (3.5)$$

3.3 VTF Implemented with Improved MCFOA

3.3.1 Simulation Results for VM Band-pass Filter

The VM BPF shown in Figure 2.12 is tested by replacing the original MCFOA with the improved MCFOA. We let $R_1 = R_2 = R_3 = 3K \text{ Ohm}$, and $C_1 = C_2 = 0.33nF$, $\omega_p=1\text{M rad/s}$, $Q_p=1$. These values are different from those used in Figure 2.12 with the old MCFOA. The component values that work well on old MCFOA cannot work properly on the improved MCFOA circuits. The reason is that both the old and improved MCFOA can only work appropriately within a very small DC voltage range around zero volts. Once the DC offset is different from zero, some of the transistors will work in the triode region, and the circuit cannot function properly as a MCFOA. The old component values on improved MCFOA circuit cause large DC offset from zero volts at some terminals, and make some of the transistors to work in the triode region.

The star line and dashed line shown in Figure 3.13 are the SPICE simulation results of the VM BPF implemented using the old MCFOA and the improved MCFOA, respectively. Table 3.5 and Table 3.6 present the ω_p and Q_p errors of the four configurations of Figure 2.11 for $Q_p = 1$ and $Q_p = 3$, respectively. The simulation result is obtained by using the same schematics as used in Section 2.3.3, but by replacing the MCFOA by the improved MCFOA, and changing the passive component values to $R_1 = R_2 = R_3 = 3K \text{ Ohm}$, and $C_1 = C_2 = 0.33nF$ for $Q_p = 1$. Specifically, the schematics for configurations (a) – (d) are as shown in Figure 2.12, Figure A.1 (a), Figure A.4

(a) and Figure A.7 (a), respectively. The performance for $Q_p=3$ is also studied by letting $R_1=9K$ Ohm.

Table 3.5: $\omega_p=1M$ rad/s=159K Hz, $Q_p=1$, VM BPF with improved MCFOA

Configuration	VM			
	ω_p (rad/s)	Q_p	Error_ ω_p (%)	Error_ Q_p (%)
a	1001696.481	0.993	0.170	-0.700
b	908512.7792	0.901	-9.148	-9.876
c	991870.3466	0.874	-0.813	-12.590
d	980278.0507	0.868	-1.972	-13.227

Table 3.6: $\omega_p=1M$ rad/s=159K Hz, $Q_p=3$, VM BPF with improved MCFOA

Configuration	VM			
	ω_p (rad/s)	Q_p	Error_ ω_p (%)	Error_ Q_p (%)
a	961069.0065	2.834	-3.893	-5.533
b	929543.9528	2.746	-7.045	-8.462
c	1005267.753	2.39	0.197	-20.307
d	1001941.281	2.113	0.264	-19.247

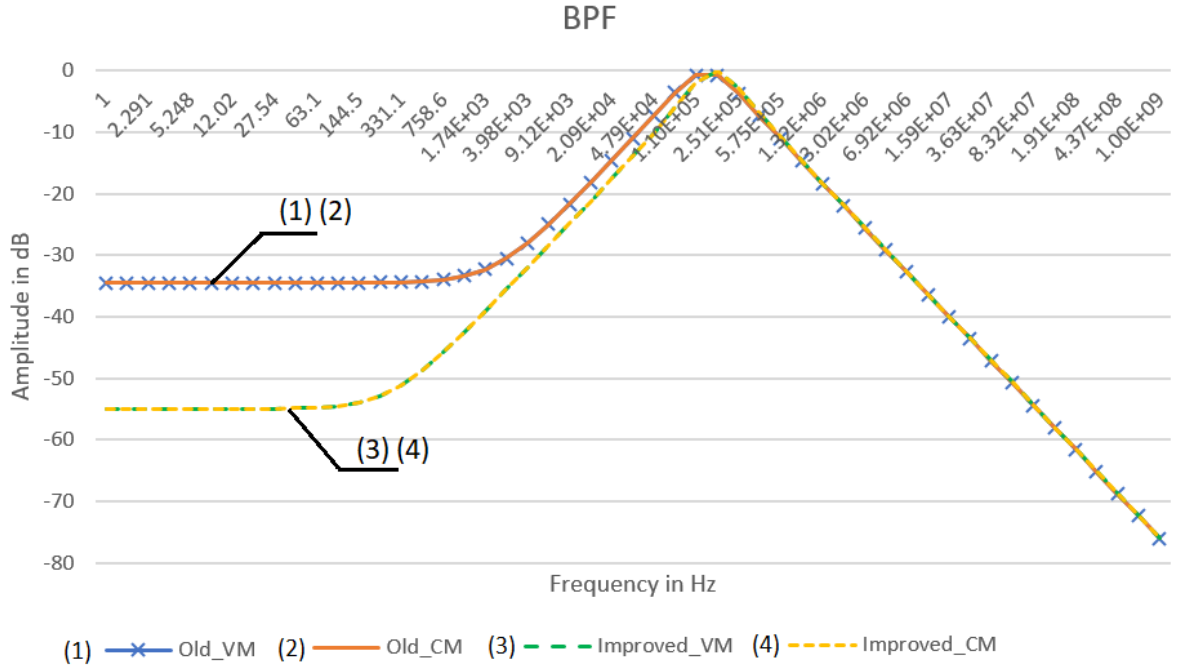


Figure 3.13: Comparison of VM and CM BPF using the old and improved MCFOA

3.3.2 Simulation Results for VM Notch Filter

Figure 3.14 shows the SPICE simulation results of the VM NF of configuration (a), which is obtained by replacing the MCFOA with the improved MCFOA in Figure 2.14, and letting $R_1 = R_2 = R_3 = 3K\text{ Ohm}$, and $C_1 = C_2 = 0.33nF$, $\omega_p = 1\text{M rad/s}$, $Q_p = 1$. These values are also different from those used in Figure 2.14 with the old MCFOA due to the same reason mentioned in Section 3.3.1.

The star line and dashed line shown in Figure 3.14 are the SPICE simulation results of the VM NF implemented using the old MCFOA and the improved MCFOA. The ω_p and Q_p errors of the four configurations (a) – (d) of Figure 2.11 are tabulated in Table 3.7 and Table 3.8 for $Q_p = 1$ and $Q_p = 3$, respectively. The simulation result is obtained by using the same schematics as used in

Section 2.3.4, but by replacing the MCFOA by the improved MCFOA, and changing the passive component values to $R_1 = R_2 = R_3 = 3K \text{ Ohm}$, and $C_1 = C_2 = 0.33nF$. Specifically, the schematics for configurations (a) – (d) are as shown in Figure 2.14, Figure B.1 (a), Figure B.4 (a) and Figure B.7 (a), respectively. The performance for $Q_p=3$ is also studied by letting $R_1=9\text{K Ohm}$.

Table 3.7: $\omega_p=1\text{M rad/s}=159\text{K Hz}$, $Q_p=1$, VM NF with improved MCFOA

Configuration	VM			
	ω_p (rad/s)	Q_p	Error_ ω_p (%)	Error_ Q_p (%)
a	1025897.541	0.988	2.590	-1.234
b	929145.2608	0.897	-7.085	-10.331
c	940209.0194	0.882	-5.979	-11.751
d	929342.4025	0.875	-7.065	-12.497

Table 3.8: $\omega_p=1\text{M rad/s}=159\text{K Hz}$, $Q_p=3$, VM NF with improved MCFOA

Configuration	VM			
	ω_p (rad/s)	Q_p	Error_ ω_p (%)	Error_ Q_p (%)
a	980376.3892	3.122	-1.962	4.074
b	950850.9001	2.963	-4.915	-1.233
c	952231.7026	2.290	-4.776	-23.651
d	948764.8097	2.286	-5.123	-23.814

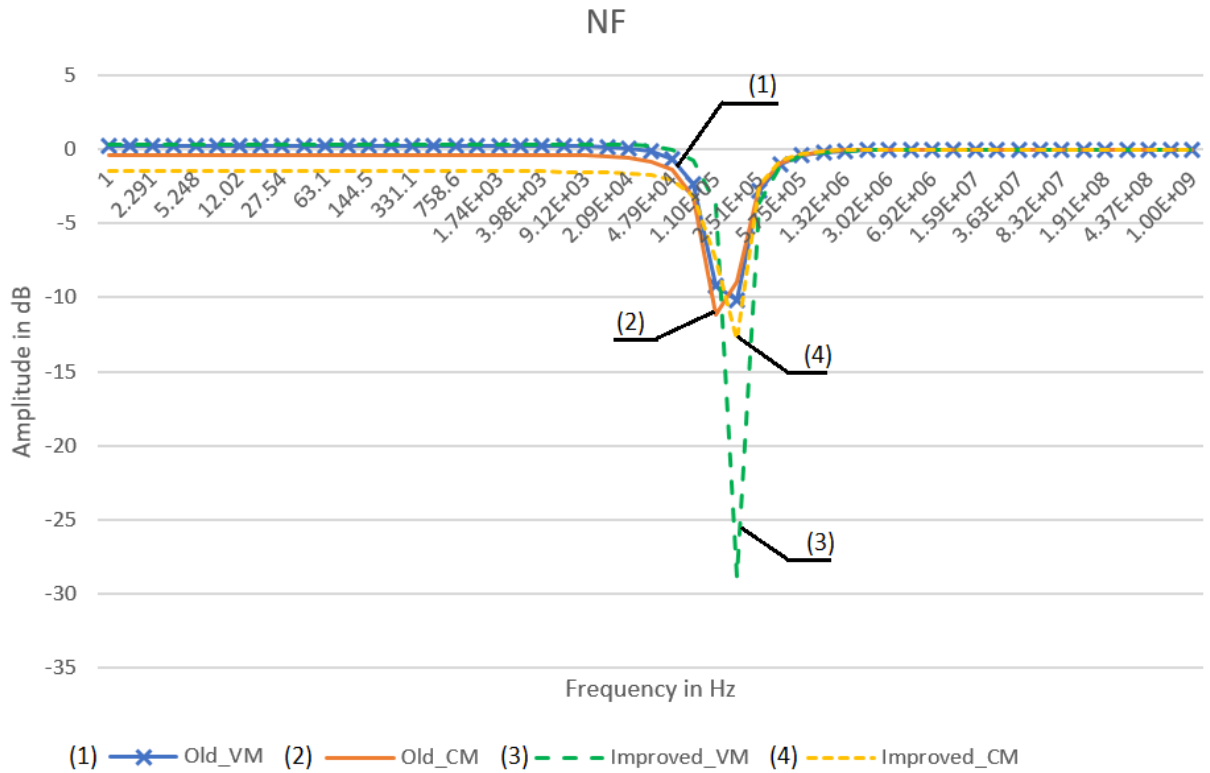


Figure 3.14: Comparison of VM and CM NF using the old and improved MCFOA

3.3.3 Performance Comparison of VM Band-pass and Notch Filters

Similar to Section 2.3.5, the ω_p and Q_p errors are compared among the four configurations shown in Figure 2.11. In Section 2.3.5, we observed that the two configurations at high impedance terminals have similar performance, and so do the two configurations at low impedance terminals. The reason lies on their similar terminal resistances, i.e., resistances at high impedance terminals Y and Z are 53.62K Ohm and 55.01K Ohm, respectively, while resistances at low impedance terminals X and W are both 159.5 Ohm. Similar terminal resistance values lead to similar coefficients in their transfer functions, and result in similar performance. The improved MCFOA has similar terminal resistances at the two low impedance terminals, whereas the high impedance

terminal Y has a resistance that is almost twice that at terminal Z. This causes a difference in the performance between the configurations at the two high impedance terminals. As a result, we can see better performance at terminal Y because of its larger terminal resistance. Specifically,

- For VM BPF, $Q_p=1$ and $Q_p=3$, and NF, $Q_p=1$, configuration (a) has an obvious advantage over the rest of configurations.
- For VM NF, $Q_p=3$, the performance of configuration (b) is very close to that of configuration (a), and it is better than that of configurations (c) and (d).
- For VM BPF and NF, $Q_p=1$ and $Q_p=3$, the two configurations whose outputs are at the low impedance terminals, i.e. configurations (c) and (d), exhibit very similar performance

3.3.4 Comparison of ω_p and Q_p Errors with Old and New MCFOA for VM

BPF and NF

The reduction of ω_p and Q_p errors of VM BPF and NF are tabulated in Table 3.9 and Table 3.10, respectively. The percentage reduction is calculated using the equation

$$Reduction = 100 \frac{(|Error_{old}| - |Error_{new}|)}{|Error_{old}|} \quad (3.6)$$

Table 3.9: Reduction in VM BPF ω_p and Q_p errors

Configurations	Reduction in ω_p errors (%)		Reduction in Q_p errors (%)	
	$Q_p = 1$	$Q_p = 3$	$Q_p = 1$	$Q_p = 3$
a	98.91	73.27	96.10	73.82
b	30.57	48.00	34.67	57.22
c	90.84	95.66	32.91	58.11
d	81.88	95.02	24.70	60.07

Table 3.10: Reduction in VM NF ω_p and Q_p errors

Configurations	Reduction in ω_p errors (%)		Reduction in Q_p errors (%)	
	$Q_p = 1$	$Q_p = 3$	$Q_p = 1$	$Q_p = 3$
a	87.89	84.02	76.90	76.65
b	45.91	55.36	21.27	92.86
c	-530.03	-68.58	-15.55	12.23
d	-342.12	-95.91	-22.08	11.43

It can be seen that there is an enormous reduction of ω_p and Q_p errors in VM BPF, ranging from 31% to 99% reduction in ω_p errors, and 25% to 96% in Q_p errors. For VM NF, ω_p and Q_p errors are reduced for configurations (a) and (b), while they are increased for configurations (c) and (d). The VM NF has 46% to 87% reduction in ω_p errors, and 21% to 93% reduction in Q_p errors. The reason for the increase of ω_p and Q_p errors for configurations (c) and (d) needs further investigation.

Besides the considerable reduction of ω_p and Q_p errors, there are also some other improvements that can be observed from Figure 3.13 and Figure 3.14. For VM BPF, they are: (i) the zero frequency moves closer to the origin, and (ii) the gain at low frequency is much lower. For VM NF, we also see that the attenuation at $\omega = \omega_p$ increases dramatically.

3.4 CTF Implemented with Improved MCFOA

3.4.1 Simulation Results for CM Band-pass Filter

The comparison of the SPICE CM BPF simulation results with the old MCFOA and the improved MCFOA are shown in Figure 3.13. The SPICE simulations are carried out on circuit of Figure 2.17 with $Q_p = 1$.

The ω_p and Q_p errors of configurations (a) – (d) are tabulated in Table 3.11 and Table 3.12 for CM BPF $Q_p = 1$ and $Q_p = 3$, respectively. These simulation results are obtained using the same schematics for the four CM BPF configurations that were used in Section 2.4.1, but by replacing the MCFOA with the improved MCFOA, and changing the values of the passive components to $R_1 = R_2 = R_3 = 3K\text{ Ohms}$, and $C_1 = C_2 = 0.33nF$ for $Q_p=1$. Specifically, the schematics for configurations (a) – (d) are shown in Figure 2.17, Figure A.1 (b), Figure A.4 (b) and Figure A.7 (b), respectively. The performance for $Q_p=3$ is also studied by letting $R_1=9K\text{ Ohm}$.

Table 3.11: $\omega_p=1\text{M rad/s}=159\text{K Hz}$, $Q_p=1$, CM BPF with the improved MCFOA

Configuration	CM			
	ω_p (rad/s)	Q_p	Error_ ω_p (%)	Error_ Q_p (%)
a	1001696.481	0.993	0.170	-0.700
b	908512.7792	0.901	-9.148	-9.876
c	980223.7161	0.868	-1.977	-13.237
d	991924.4802	0.874	-0.807	-12.580

Table 3.12: $\omega_p=1\text{M rad/s}=159\text{K Hz}$, $Q_p=3$, CM BPF with the improved MCFOA

Configuration	CM			
	ω_p (rad/s)	Q_p	Error_ ω_p (%)	Error_ Q_p (%)
a	961069.0065	2.834	-3.893	-5.533
b	929543.9528	2.746	-7.045	-8.462
c	1001941.281	2.113	0.195	-29.561
d	1005267.753	2.112	0.527	-29.607

3.4.2 Simulation Results for CM Notch Filter

A comparison of the SPICE CM NF simulation results on the old MCFOA and the improved MCFOA are given in Figure 3.14. The SPICE simulations are carried out on the circuit of Figure 2.18 with $Q_p = 1$. The ω_p and Q_p errors of configuration (a) – (d) are tabulated in Table 3.13 and Table 3.14 for CM NF $Q_p = 1$ and $Q_p = 3$, respectively. These simulation results are obtained using the same schematics for the four CM NF configurations that were used in Section 2.4.2, but replacing the MCFOA with the improved MCFOA, and changing the values of the passive components to $R_1 = R_2 = R_3 = 3\text{K Ohms}$, and $C_1 = C_2 = 0.33\text{nF}$ for $Q_p = 1$. Specifically, the schematics for configurations (a) – (d) are shown in Figure 2.18, Figure B.1 (b), Figure B.4 (b) and Figure B.7 (b), respectively. The performance for $Q_p=3$ is also studied by letting $R_1=9\text{K Ohm}$.

Table 3.13: $\omega_p=1\text{M rad/s}=159\text{K Hz}$, $Q_p=1$, CM NF with the improved MCFOA

Configuration	CM			
	ω_p (rad/s)	Q_p	Error_ ω_p (%)	Error_ Q_p (%)
a	912147.2915	0.983	-8.785	-1.668
b	--	--	--	--
c	1035502.688	0.875	3.551	-12.479
d	--	--	--	--

Table 3.14: $\omega_p=1\text{M rad/s}=159\text{K Hz}$, $Q_p=3$, CM NF with the improved MCFOA

Configuration	CM			
	ω_p (rad/s)	Q_p	Error_ ω_p (%)	Error_ Q_p (%)
a	891863.9214	2.747	-10.813	-8.435
b	--	--	--	--
c	1052850.943	2.290	5.286	-23.656
d	--	--	--	--

3.4.3 Performance Comparison of CM Band-pass and Notch Filters

The transposed CM filters have improvements that are similar to that of the VM counterparts, such as different performances at the two high impedance terminals, and similar performance at the two low impedance terminals. Specifically,

- For CM BPF and NF, $Q_p=1$ and $Q_p=3$, configuration (a) exhibits the best performance.

- For CM BPF, the two configurations whose input currents are at the low impedance terminals, i.e. configurations (c) and (d), exhibit very similar performance.
- Configuration (b) and (d) are not able to realize NF using new MCFOA due to the same reason as with the old MCFOA. See Appendix B for explanation.

3.4.4 Comparison of ω_p and Q_p Errors with Old and New MCFOA for CM Band-pass and Notch Filters

The reduction in ω_p and Q_p errors for BPF and NF are tabulated in Table 3.15 and Table 3.16, respectively. The percentage reduction is calculated using Equation (3.6).

CM BPF has an enormous reduction of ω_p and Q_p errors, and the reduction range is exactly the same as in the case of its VM counterpart, i.e. ranging from 31% to 99% reduction in ω_p errors, and 25% to 96% in Q_p errors. For CM NF, configurations (b) and (d) are not able to realize NF due to the reasons mentioned in Section 2.4.3 (see Appendix B for explanation). ω_p and Q_p errors are reduced for configuration (a), while they are increased for configuration (c). The ω_p error of CM NF configuration (a) is reduced by 49% and 43% for $Q_p = 1$ and $Q_p = 3$, respectively. The Q_p error is reduced by 91% and 62% for $Q_p = 1$ and $Q_p = 3$, respectively. The reason for the increase of ω_p and Q_p errors for configuration (c) needs further investigation.

Similar to the VM counterpart, besides the considerable reduction in ω_p and Q_p errors, there are also some other improvements that can be observed from Figure 3.13 and Figure 3.14. For CM BPF, they are: (i) the zero frequency moves closer to the origin, and (ii) the gain at low frequency is much lower. For CM NF, we also see that there is a minor increase of the attenuation at $\omega = \omega_p$.

Table 3.15: Reduction in CM BPF ω_p and Q_p errors

Configurations	Reduction in ω_p errors (%)		Reduction in Q_p errors (%)	
	$Q_p = 1$	$Q_p = 3$	$Q_p = 1$	$Q_p = 3$
a	98.91	73.27	96.10	73.81
b	30.57	48.59	34.67	58.68
c	81.82	96.32	24.68	38.67
d	90.91	88.38	32.97	38.93

Table 3.16: Reduction in CM NF ω_p and Q_p errors

Configurations	Reduction in ω_p errors (%)		Reduction in Q_p errors (%)	
	$Q_p = 1$	$Q_p = 3$	$Q_p = 1$	$Q_p = 3$
a	49.28	43.40	90.81	62.26
b	--	--	--	--
c	31.33	-23.53	-27.43	5.38
d	--	--	--	--

3.5 Comparison of VTF with the Transposed CTF

A comparison of ω_p and Q_p errors between the VM filters and the corresponding transposed CM filters are shown in Tables 3.17 and 3.18.

From the data shown in Tables 3.17 and 3.18, we can conclude the following,

- For BPF, VM and CM exhibit very close performance, except for configurations (c) and (d) when $Q_P=3$. The performance of VM is better than that of CM.

- For NF, it is not possible to compare the performance of CM with the VM counterpart for configurations (b) and (d) due to their inability to realize NF. See Appendix B for explanation.
- For NF configuration (a), VM has better performance.
- For NF configuration (c), VM and CM have very similar performance.

Table 3.17: Comparison of performance of VM and CM BPF using improved MCFOA

Configurations	Total error of BPF $Q_p=1$ (%)				Total error of BPF $Q_p=3$ (%)			
	VM		CM		VM		CM	
	Error ω_P (%)	Error Q_P (%)	Error ω_P (%)	Error Q_P (%)	Error ω_P (%)	Error Q_P (%)	Error ω_P (%)	Error Q_P (%)
a	0.170	-0.700	0.170	-0.700	-3.893	-5.533	-3.893	-5.533
b	-9.148	-9.876	-9.148	-9.876	-7.045	-8.462	-7.045	-8.462
c	-0.813	-12.590	-1.977	-13.237	0.197	-20.307	0.195	-29.561
d	-1.972	-13.227	-0.807	-12.580	0.264	-19.247	0.527	-29.607

Table 3.18: Comparison of performance of VM and CM NF using improved MCFOA

Configurations	Total error of NF $Q_p=1$ (%)				Total error of NF $Q_p=3$ (%)			
	VM		CM		VM		CM	
	Error ω_P (%)	Error Q_P (%)	Error ω_P (%)	Error Q_P (%)	Error ω_P (%)	Error Q_P (%)	Error ω_P (%)	Error Q_P (%)
a	2.590	-1.234	-8.785	-1.668	-1.962	4.074	-10.813	-8.435
b	-7.085	-10.331	--	--	-4.915	-1.233	--	--
c	-5.979	-11.751	3.551	-12.479	-4.776	-23.651	5.286	-23.656
d	-7.065	-12.497	--	--	-5.123	-23.814	--	--

3.6 Conclusion

The improved MCFOA presented in this chapter has more ideal terminal resistances than the old one presented in Chapter 2. The terminal resistances at terminals X and W were reduced by changing the dimensions of some of the transistors, while those at terminals Y and Z increased by adopting modified cascode current mirror structure. The proposed MCFOA has resulted in several improvements on the performance of both the VM and CM BPFs, such as more attenuation at low frequencies, and drastic reduction in the ω_p and Q_p errors. Both the VM and CM BPF have the same amount of improvement, ranging from 31% to 99% reduction on ω_p errors, and 25% to 96% reduction on Q_p errors. The largest improvement happens for configuration (a) of Figure. 2.11 for both the VM and CM BPFs. For NF, we see the reduction for ω_p and Q_p errors on configurations (a) and (b) of the VM filter, and for configuration (a) of the CM filter.

In the next chapter, the transposition theory is applied to BPF realized using CCII and FTFN. The non-ideal terminal resistances are taken into consideration and their effects on filters are investigated.

Chapter 4

Voltage and Current Transfer Function Realizations with CCII and FTFN

In Chapters 2 and 3, the VTF and CTF realized using the MCFOA implemented in [7] and the proposed improved MCFOA, respectively, have been investigated. CCII and FTFN are two other popular devices frequently applied in current-mode filter design. In this chapter, BPFs implemented with CCII and FTFN are studied, and the corresponding transposed VM or CM BPFs explored as well.

4.1 VTF and CTF Realized with CCII

Some prevailing implementations of CCII and its transposes have been briefly introduced in Section 1.3.1. In this section, VTF and the transposed CTF realized with CCII are investigated.

4.1.1 The Implementation of CCII

As mentioned in Section 1.3.1, an MCFOA is actually made up of two composite connected CCII_s (CCII- and CCII+), as shown in Figure 1.11 (b). Figure 4.1 shows the schematics of CCII+ and CCII-.

The hybrid matrix of CCII_± is:

$$\begin{bmatrix} i_y \\ i_z \\ v_x \end{bmatrix} = \begin{bmatrix} 0 & 0 & 0 \\ 0 & h_{22} & \pm\beta \\ \alpha & 0 & h_{33} \end{bmatrix} \begin{bmatrix} v_y \\ v_z \\ i_x \end{bmatrix} \quad (4.1)$$

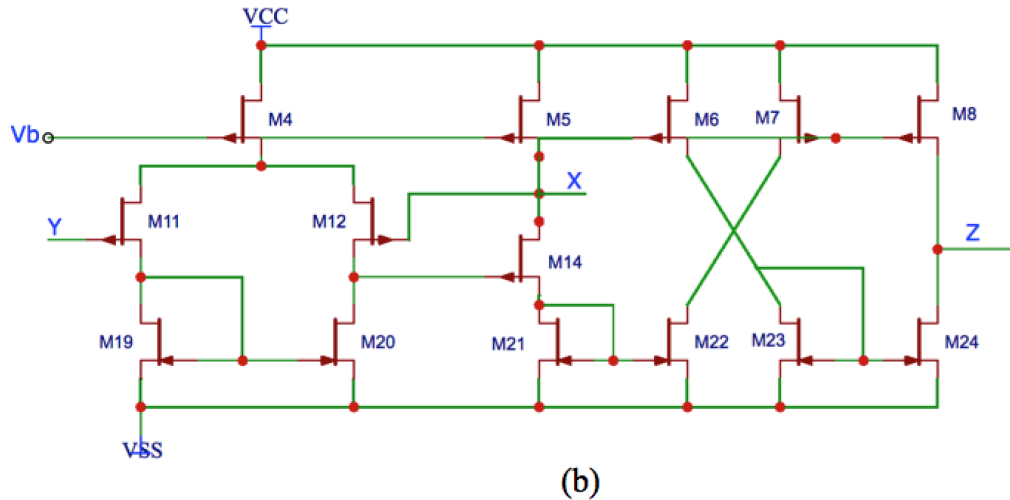
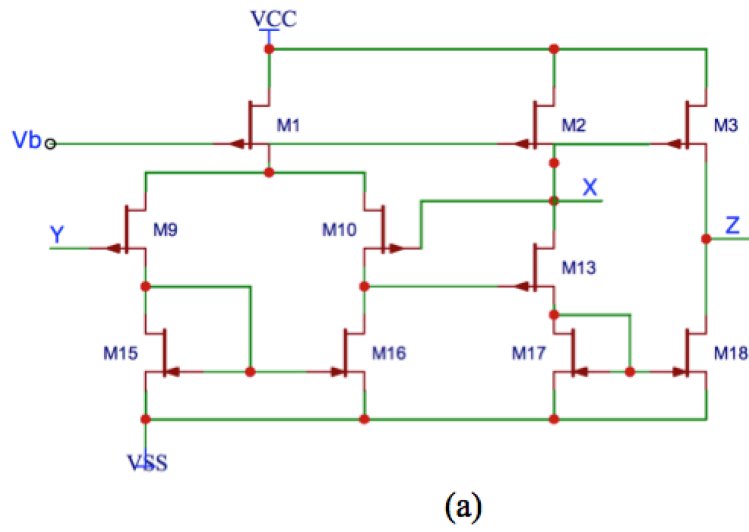


Figure 4.1: The implementation of CCII
 (a) CCII+ (b) CCII-

In Equation (4.1), h_{22} is the parasitic admittance of the terminal Z, and h_{33} is the parasitic impedance of the terminal X, and α and β are the voltage and current gains, respectively. These parameters can be determined by simulating the circuit shown in Figure 4.2. The rest of the elements are small enough to be neglected.

The current gain β is determined by injecting an ideal test current source to the terminal X through a 1000F capacitor, and measuring the current generated at the terminal Z through a 1000F capacitor. The voltage gain α is determined by applying an ideal test voltage source to the terminal Y, and measuring the voltage generated at the terminal X. The results from the above tests are: $\alpha=0.943$ and $\beta=0.975$ for CCII+, and $\alpha=0.943$ and $\beta=-1.013$ for CCII-. The frequency responses of the current and voltage gains of CCII+/- are shown in Figure 4.3 and Figure 4.4, respectively.

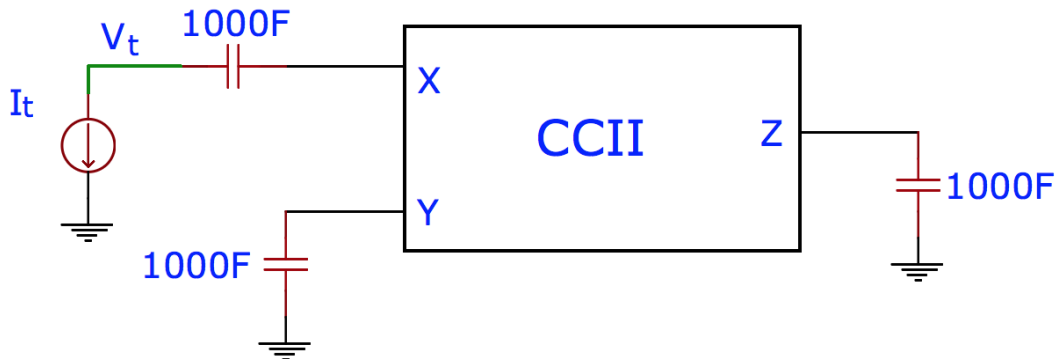


Figure 4.2: Circuit setup to determine the CCII parasitic parameters

To determine the terminal impedances Z_x and Z_z , i.e. h_{33} and $\frac{1}{h_{22}}$, an ideal test current source is connected to the terminal X or Z through a 1000F capacitor, and the voltage generated at the terminals X or Z is measured as the case may be. The frequency responses of Z_x and Z_z for CCII+ are shown in Figures 4.5 and 4.6, respectively, and the corresponding responses for CCII- are shown in Figures 4.7 and 4.8, respectively. Assuming Z_x and Z_z to be both first order transfer functions, Z_x appears as R_x and L_x in series, while Z_z appears as R_z and C_z in parallel. The values of R_x and R_z are those around very low frequencies of the frequency responses, and L_x and C_z can be determined by finding the cutoff frequency of each of the frequency responses. Table 4.1 lists the parasitic parameters of CCII+ and CCII-.

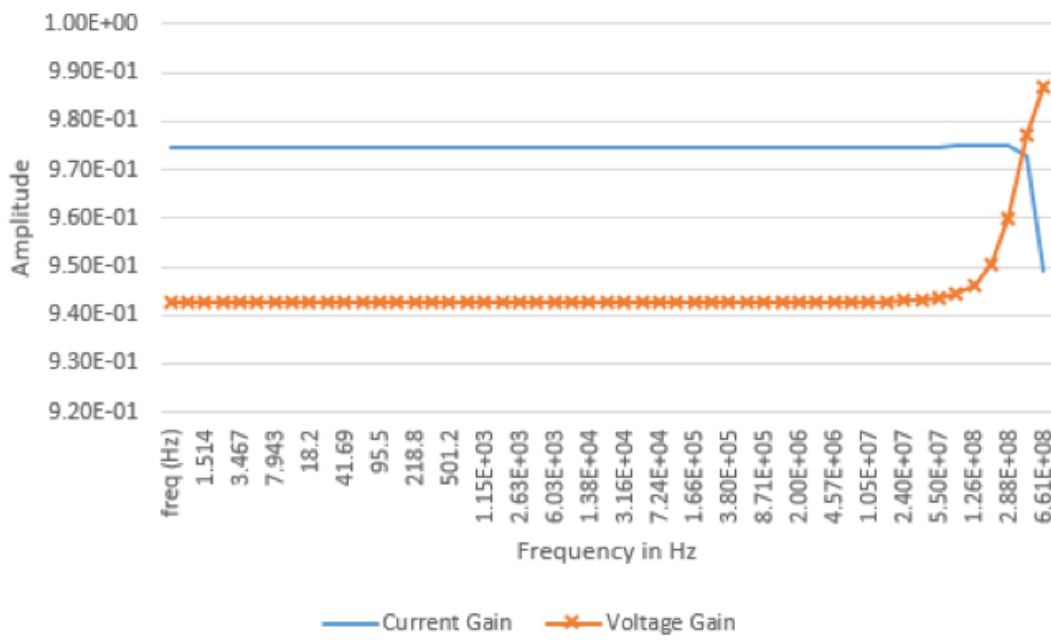


Figure 4.3: Current/voltage gain frequency response of CCII+

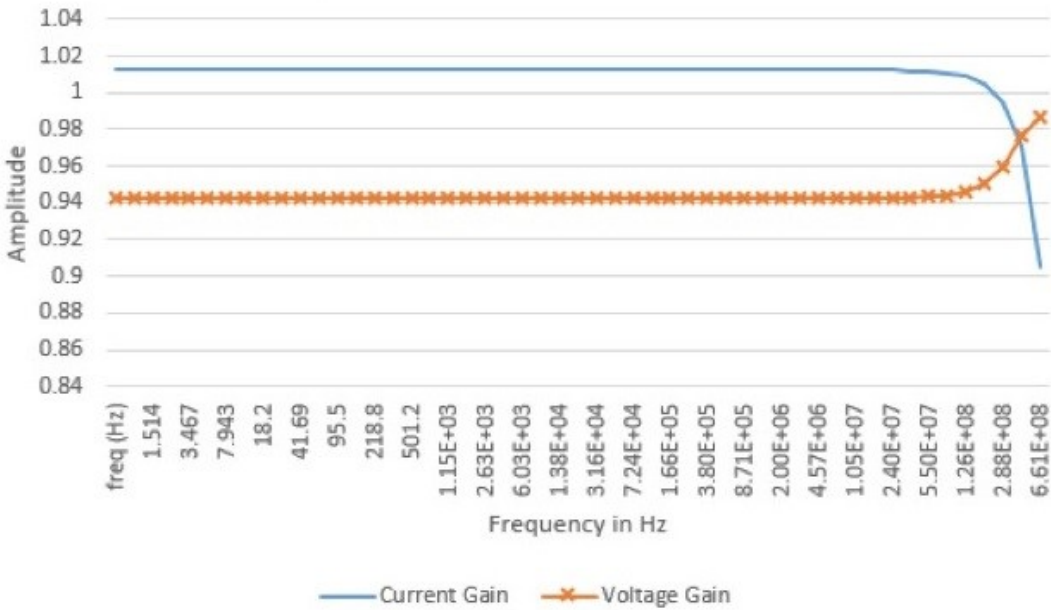


Figure 4.4: Current/voltage gain frequency response of CCII-

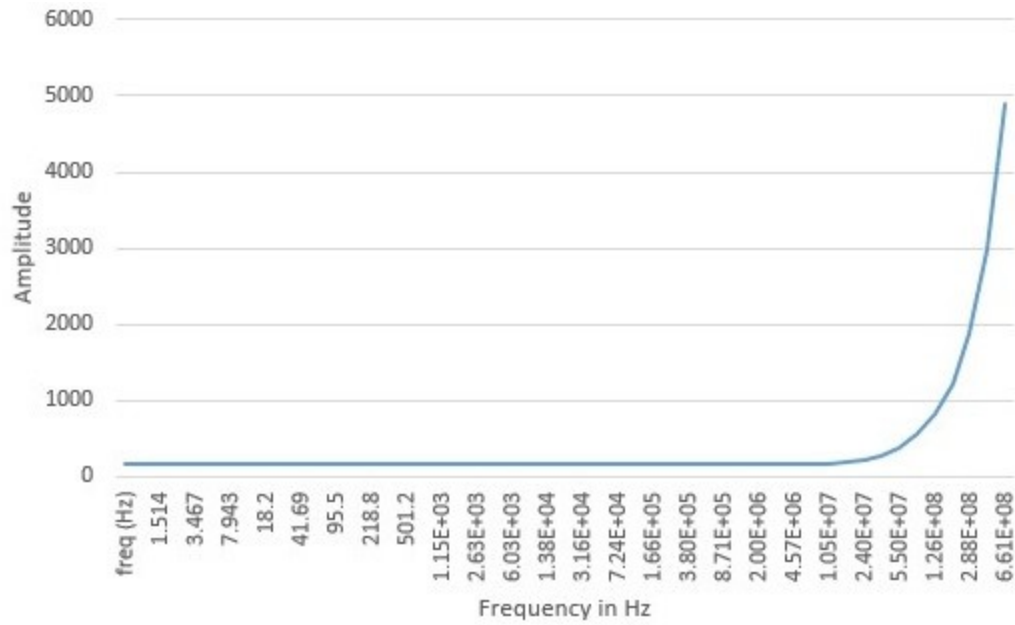


Figure 4.5: Frequency response of Z_x of CCII+

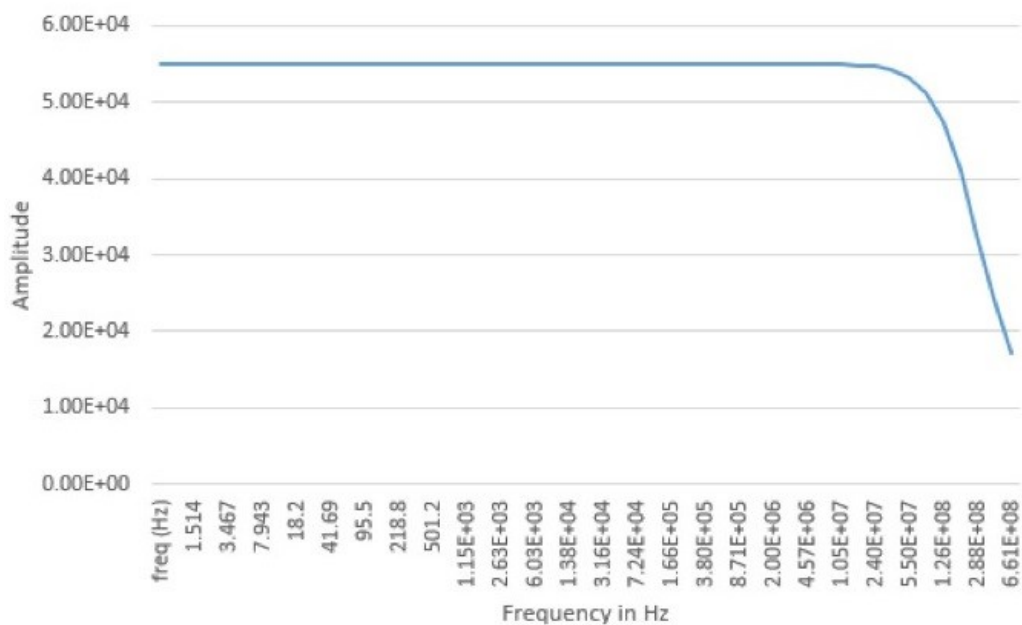


Figure 4.6: Frequency response of Z_z of CCII+

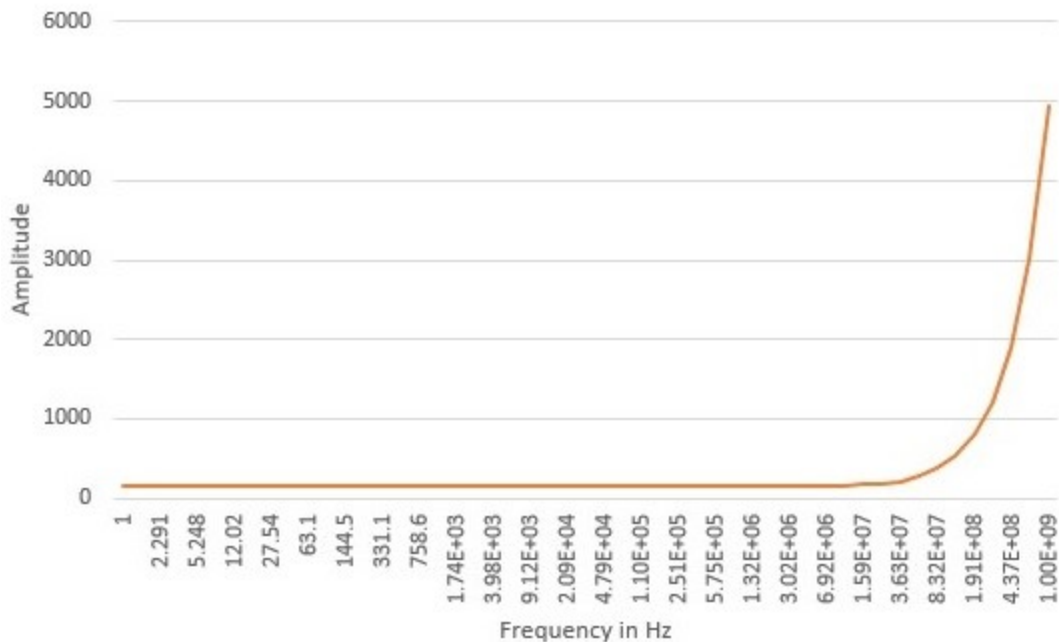


Figure 4.7: Frequency response of Z_x of CCII-

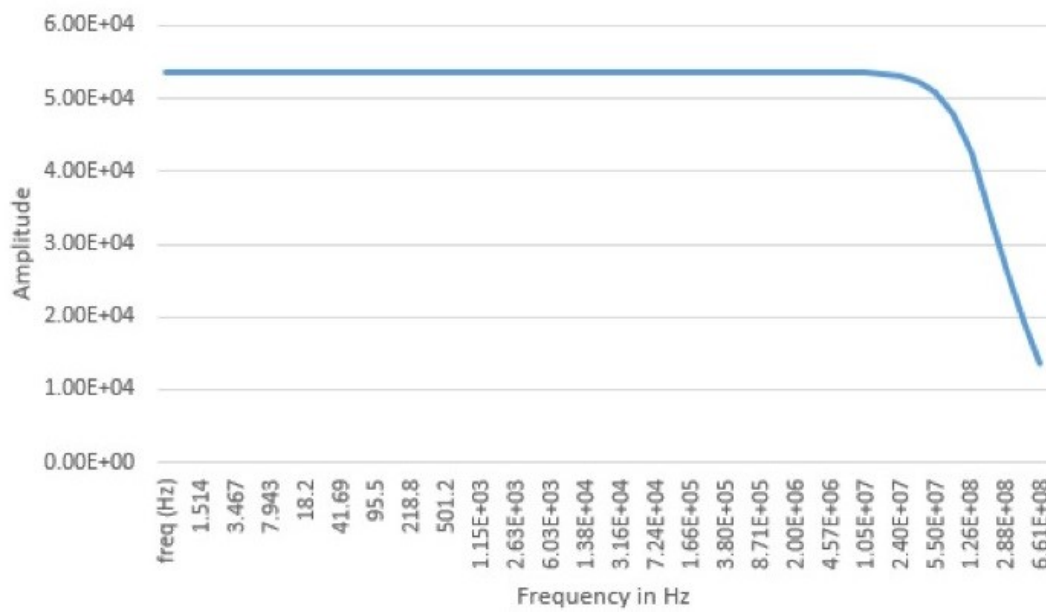


Figure 4.8: Frequency response of Z_z of CCII-

Table 4.1: Parasitic parameters of CCII- and CCII+

	Terminal	Resistance (ohm)	Capacitance (F)	Inductance (H)
CCII+	X	159.5	--	666n
	Y	Infinity	--	--
	Z	55.01K	9f	--
CCII-	X	159.5	--	663n
	Y	Infinity	--	--
	Z	53.62K	12f	--

According to the port relations given in Equation (4.1) and the terminal parasitic parameters shown in Table 4.1, a non-ideal CCII can be modeled as shown in Figure 4.9 [35].

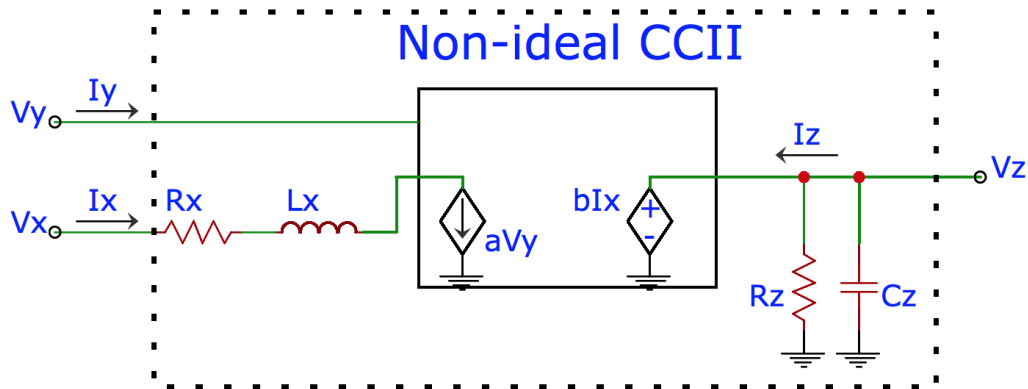


Figure 4.9: Non-ideal model of CCII

4.1.2 Filter Implemented with CCII

Many voltage-mode universal filters using CCIIIs have been proposed in the recent past. Some TISO filters have been realized using two CCIIIs [26, 27, 36-38]. Some authors have used three CCIIIs to connect each input directly to the high impedance terminal of a CCII (usually this is for

cascade application) [39, 40]. In this chapter, we wish to compare the performance of VTF and its transposed CTF implemented with CCII-s with those implemented with MCFOA in Chapter 2. Based on the fact that the MCFOA is actually realized by interconnecting two CCII-s, it is reasonable to choose a TISO filter using two CCII-s. From the perspective of transposition, the transpose of a CCII- is CCII- itself, just like the MCFOA, but with the terminals Y and Z interchanged (with all passive element positions unchanged). whereas that of CCII+ is ICCII-, which is another device. Clearly, it will be convenient to find the corresponding transposed circuits if a filter is implemented with two CCII-s, such as the circuit proposed in [27], since the same device can be used to realize the corresponding CTF. In the following section, some results concerning the VM BPF proposed in [27] and its transposed CM BPF are presented.

The schematics of the VM BPF proposed in [27] and its transposed CM BPF are shown in Figure 4.10 (a) and (b), respectively.

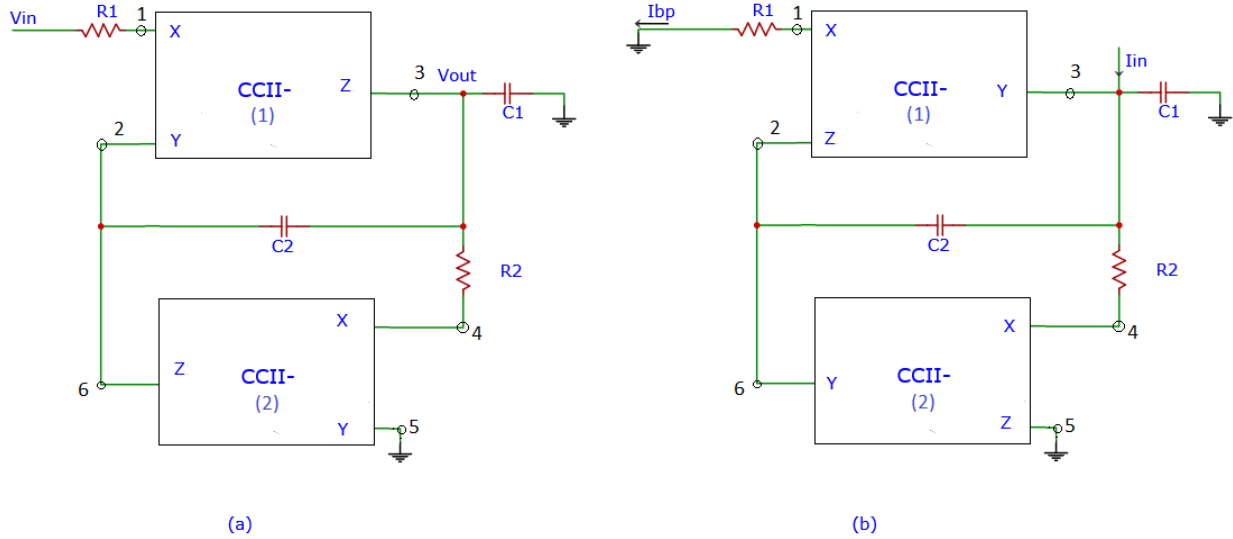


Figure 4.10: VM and transposed CM BPF with two CCII-
 (a) VM BPF proposed in [27] (b) corresponding transposed CM BPF

Considering the non-ideal model of CCII- shown in Figure 4.9, the transfer functions of the VM and the transposed CM BPF are derived as

$$\begin{aligned} \frac{V_{out}}{V_{in}} = & R'_2 R_{z1} (C_2 R_{y1} R_{z2} s + R_{y1} + R_{z2}) / (C_1 C_2 R'_1 R'_2 R_{y1} R_{z1} R_{z2} s^2 + \\ & C_1 R'_1 R'_2 R_{y1} R_{z1} s + C_1 R'_1 R'_2 R_{z1} R_{z2} s + C_2 R'_1 R'_2 R_{y1} R_{z1} s + \\ & C_2 R'_1 R'_2 R_{y1} R_{z2} s + C_2 R'_1 R'_2 R_{z1} R_{z2} s + C_2 R'_2 R_{y1} R_{z1} R_{z2} s + R'_1 R'_2 R_{y1} + \\ & R'_1 R'_2 R_{z2} + R'_1 R_{y1} R_{z1} + R'_1 R_{z1} R_{z2} + R_{y1} R_{z1} R_{z2}) \\ & R'_1 = R_1 + R_{x1}, R'_2 = R_2 + R_{x2} \end{aligned} \quad (4.2)$$

$$\begin{aligned} \frac{I_{out}}{I_{in}} = & R'_2 R_{y1} (C_2 R_{z1} R_{y2} s + R_{z1} + R_{y2}) / (C_1 C_2 R'_1 R'_2 R_{z1} R_{y1} R_{y2} s^2 + \\ & C_1 R'_1 R'_2 R_{z1} R_{y1} s + C_1 R'_1 R'_2 R_{y1} R_{y2} s + C_2 R'_1 R'_2 R_{z1} R_{y1} s + \\ & C_2 R'_1 R'_2 R_{z1} R_{y2} s + C_2 R'_1 R'_2 R_{y1} R_{y2} s + C_2 R'_2 R_{z1} R_{y1} R_{y2} s + R'_1 R'_2 R_{z1} + \\ & R'_1 R'_2 R_{y2} + R'_1 R_{z1} R_{y1} + R'_1 R_{y1} R_{y2} + R_{z1} R_{y1} R_{y2}) \\ & R'_1 = R_1 + R_{x1}, R'_2 = R_2 + R_{x2} \end{aligned} \quad (4.3)$$

To derive the non-ideal VTF and CTF, it is necessary to consider the resistance at the terminal Y, although it is infinity as shown in Table 4.1. Otherwise, it is not obvious to see the connection between the CTF and VTF. The reason is that the transposed CCII- is itself with the position of passive components unchanged, but only the terminals Y and Z interchanged. For example, the positions of passive components C_1, C_2 and R_1 connected to node 3 in Figure 4.10 (a) do not change in the transposed circuit of Figure 4.10 (b). The only difference is that node 3 is connected to terminal Y in the transposed CM circuit of Figure 4.10 (b) instead of terminal Z as in its VM counterpart of Figure 4.10 (a) is. However, the resistances of terminals Y and Z do not change, since it is the same CCII- used in both VM and transposed CM circuits. As a result, in place of R_z that interacts with passive components connected to the node 3 in VM circuit, R_y interacts with them in transposed CM circuit. For the same reason, the grounded terminal Y_2 (node 5) in the VM circuit of Figure 4.10 (a) becomes the grounded terminal Z_2 (node 5) in the transposed CM circuit of Figure 4.10 (b), and the terminal resistance R_{y2} shows up in CTF of Equation (4.3) instead of

R_{z2} in VTF of Equation (4.2). Therefore, we have to take R_{y1} and R_{y2} into consideration to see the connection between VTF and transposed CTF. Comparing Equations (4.2) and (4.3), one can see that the CTF is the same as its VTF, except that the positions of R_{Y1} and R_{z1} , R_{Y2} and R_{z2} are interchanged, respectively. The two equations also show that the terminal resistances create a non-zero zero, and make the BPF to behave as a LPF with a high Q, just as in the case of BPFs realized using MCFOA.

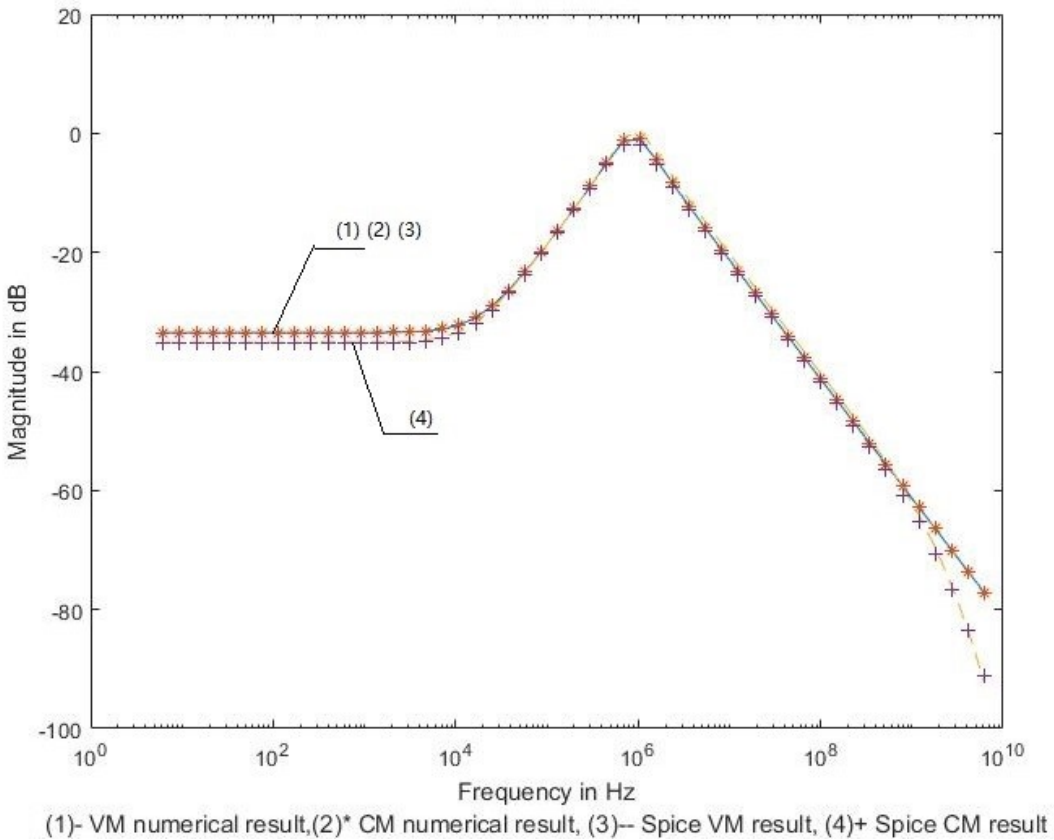


Figure 4.11: Results for BPF of the circuits of Figure 4.10

Assuming the CCII- to be ideal, both the VM and the transposed CM transfer function become

$$\frac{V_{out}}{V_{in}} = \frac{I_{out}}{I_{in}} = \frac{sC_2R_2}{s^2C_1C_2R_1R_2 + sC_2R_2 + 1} \quad (4.4)$$

$$\omega_p = \frac{1}{\sqrt{R_1 R_2 C_1 C_2}}, Q = \sqrt{\frac{R_1 C_1}{R_2 C_2}} \quad (4.5)$$

where $R_{y1} = \infty, R_{z1} = R_{z2} = \infty, R_{x1} = R_{x2} = 0$.

Circuit simulation and numerical simulation results for the VM and CM BPF responses are shown in Figure 4.11. Circuit simulation results are obtained from simulating the circuits in Figure 4.10 (a) and (b), while the numerical simulation results are calculated using the transfer functions given by Equations (4.2) and (4.3). These results are obtained with the circuit component values of $R_1 = R_2 = 1K \text{ ohm}$, and $C_1 = C_2 = 1 nF$. The specified ω_p is $1M \text{ rad/s}$, $Q_p=1$. The plots in Figure 4.11 show that the simulation results are very close to the numerical simulation results. Thus, Equations (4.2) and (4.3) can be used to model the behavior of BPFs.

Table 4.2 shows the deviations of ω_p and Q_p from the specified values for both the VM and the transposed CM circuits. For $Q_p = 3$, we let $R_1 = 3K \text{ ohm}, R_2 = 1K \text{ ohm}$, and $C_1 = 1n F, C_2 = 330p F$. It is seen that the deviations in ω_p and Q_p from the specified values are higher in the transposed CM filter circuit compared to that of VM circuit.

Table 4.2: CCII- BPF ω_p and Q_p errors

		ω_p (rad/s) (rad/s)	Q	Error_ ω_p (%)	Error_Q (%)
VM	$\omega_p = 1M \text{ rad/s } Q_p = 3$	1.022M	3.01	2.2	1
	$\omega_p = 1M \text{ rad/s } Q_p = 1$	925.67K	0.903	-7.4	-9.7
CM	$\omega_p = 1M \text{ rad/s } Q_p = 3$	933.71K	1.75	-6.62	41.7
	$\omega_p = 1M \text{ rad/s } Q_p = 1$	856.8K	0.794	-14.3	20.6

4.1.3 Performance Comparison of Band-pass Filters Implemented Using CCII- and MCFOA

As discussed in Chapter 2, there are four configurations of VM BPF and their corresponding transposed CM BPFs. We choose the BPF configuration that has the best performance using the original MCFOA to compare with that of the BPF using CCII-. Thus, BPF configurations (c) of Figure A.4 (a) and (b) are used for the comparison of $Q_p = 1$ for VM and CM, respectively, and BPF configurations (b) of Figure A.1 (a) and (b) are used for the comparison of $Q_p = 3$ for VM and CM, respectively. The results are presented in Table 4.3. It shows that the performance of VM BPF using CCII- is better than that using MCFOA for both $Q_p = 1$ and $Q_p = 3$. On the contrary, the performance of CM BPF using MCFOA is better than that using CCII- for both $Q_p = 1$ and $Q_p = 3$. Similar results for the BPFs when the proposed MCFOA is used are also given in Table 4.3. These results show that the BPFs using the proposed MCFOA have far more superior performance to those using the original MCFOA and CCII- except VM BPF with $Q_p=3$, in which case BPF using CCII- has the best performance.

Table 4.3: Comparison of BPF performance implemented using MCFOA and CCII-

		BPF using original MCFOA		BPF using proposed MCFOA		BPF using CCII-	
		Error_ω _p (%)	Error_Q (%)	Error_ω _p (%)	Error_Q (%)	Error_ω _p (%)	Error_Q (%)
VM	ω _p = 1M rad/s Q _p = 3	-13.549	-19.778	-3.893	-5.533	2.2	1
	ω _p = 1M rad/s Q _p = 1	8.879	-18.767	0.170	-0.700	-7.4	-9.7
CM	ω _p = 1M rad/s Q _p = 3	-13.704	-20.478	-3.893	-5.533	-6.62	41.7
	ω _p = 1M rad/s Q _p = 1	10.877	-17.574	0.170	-0.700	-14.3	20.6

4.2 VTF And CTF of BPF Using FTFN

4.2.1 Transpose of FTFN

FTFN has been briefly introduced in section 1.3.4. The block diagram of FTFN is shown in Figure 4.12, and the port relations are shown in Equation (4.6) [10]. The hybrid matrix of FTFN needs to be determined to find the transpose of FTFN. It is impossible to write the hybrid matrix directly from its port relations, and there is no report of a hybrid matrix for FTFN in the literature. A possible approach is to determine the admittance matrix of FTFN through its port relations, and find its transpose from the transposed admittance matrix directly [1].

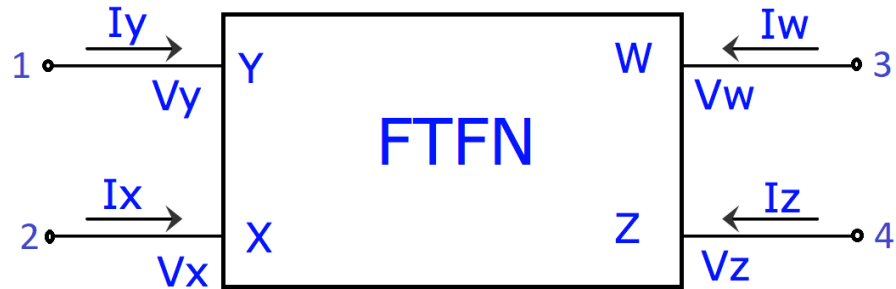


Figure 4.12: The block diagram of FTFN

$$I_x = I_y = 0, \quad V_x = V_y, \quad I_z = -I_w \quad (4.6)$$

Assuming the admittance matrix of FTFN is

$$\begin{bmatrix} I_x \\ I_y \\ I_w \\ I_z \end{bmatrix} = \begin{bmatrix} 0 & 0 & 0 & 0 \\ 0 & 0 & 0 & 0 \\ g_{31} & g_{32} & g_{33} & g_{34} \\ g_{41} & g_{42} & g_{43} & g_{44} \end{bmatrix} \begin{bmatrix} V_x \\ V_y \\ V_w \\ V_z \end{bmatrix} \quad (4.7)$$

According to one of the port relations of FTFN, $I_z = -I_w$, the following equation should be satisfied:

$$g_{31}V_x + g_{32}V_y + g_{33}V_w + g_{34}V_z = -(g_{41}V_x + g_{42}V_y + g_{43}V_w + g_{44}V_z) \quad (4.8)$$

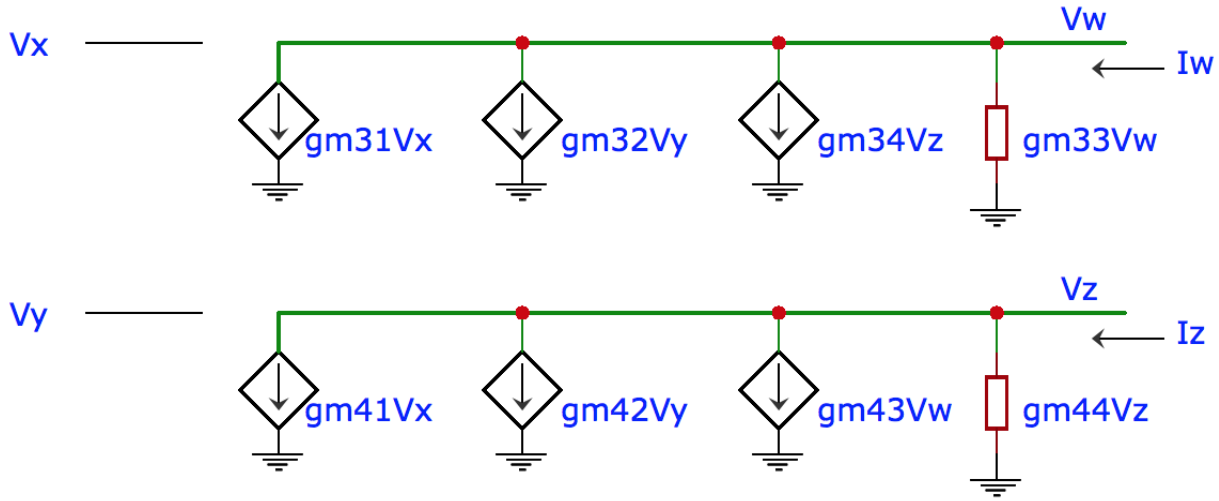


Figure 4.13: AC equivalent circuit of FTFN

This equation can be represented by the AC equivalent circuit shown in Figure 4.13. There are many possible solutions for the four variables from the single Equation (4.8). The simplest solution that can be assumed for Equation (4.8) is $g_{31} = -g_{41}$, $g_{32} = -g_{42}$, $g_{33} = -g_{43}$ and $g_{34} = -g_{44}$. However, it can be seen that g_{33} and g_{44} are in fact the passive conductances at the terminals W and Z, and for practical CMOS circuits, they are usually at the level of 10^{-5} . It is very difficult, if impossible, to make $g_{33}=g_{43}$ or $g_{34}=g_{44}$ in practice, since the transconductances g_{34} and g_{43} are often at the level of 10^{-4} . Therefore, a reasonable solution for Equation (4.8) could be $g_{31} = -g_{41}$, $g_{32} = -g_{42}$, $g_{33} = -g_{44}$ and $g_{34} = -g_{43}$. In addition, the terminals X and Y have a characteristic similar to that of an ideal Op-Amp, i.e., $I_z = -I_w = G(V_x - V_y)$, where $G=\infty$ and $V_x = V_y$ for ideal FTFN. Thus, it is reasonable to assume that $g_{31} = -g_{41} = -g_{32} = g_{42} = G$. A FTFN that satisfies these relations is a FTFN with symmetrical output resistances, which has been introduced in section 1.3.4 [10].

However, V_w must equal to V_z to make Equation (4.8) valid. This may be difficult to satisfy, because the terminals W and Z are two independence terminals, and the voltage at these nodes are uncertain.

The aforesaid situation could be resolved if we let $g_{34} = -g_{43} = 0$, i.e. the current I_z or I_w does not depend on V_w or V_z , respectively.

Now assuming $g_{33} = -g_{44} = \alpha$, $g_{34} = -g_{43} = 0$, and $g_{31} = -g_{41} = -g_{32} = g_{42} = \gamma$, where α should be very small, whereas γ should be large, the admittance matrix given by Equation (4.7) becomes

$$\begin{bmatrix} I_x \\ I_y \\ I_w \\ I_z \end{bmatrix} = \begin{bmatrix} 0 & 0 & 0 & 0 \\ 0 & 0 & 0 & 0 \\ \gamma & -\gamma & \alpha & 0 \\ -\gamma & \gamma & 0 & -\alpha \end{bmatrix} \begin{bmatrix} V_x \\ V_y \\ V_w \\ V_z \end{bmatrix} \quad (4.9)$$

The transposed admittance matrix with respect to Equation (4.9) is

$$\begin{bmatrix} I_x' \\ I_y' \\ I_w' \\ I_z' \end{bmatrix} = \begin{bmatrix} 0 & 0 & \gamma & -\gamma \\ 0 & 0 & -\gamma & \gamma \\ 0 & 0 & \alpha & 0 \\ 0 & 0 & 0 & -\alpha \end{bmatrix} \begin{bmatrix} V_x' \\ V_y' \\ V_w' \\ V_z' \end{bmatrix} \quad (4.10)$$

From Equation (4.10), we can conclude several characteristics of the transpose of FTFN:

- $I_x' = -I_y' = A(V_w' - V_z')$, where $A = \gamma = \infty$ ideally.
- $V_w' = V_z'$ as long as A is very large.
- $Y_x' = Y_y' = 0$, resulting in $R_x' = R_y' = \infty$.
- $Y_w' = Y_z' = \alpha$, where α has been assumed to be very small, resulting in $R_w' = R_z' = \infty$ ideally.

The original as well as the transpose of FTFN is an infinite gain transconductance amplifier which has two current outputs of the same magnitude, but in opposite directions. Resistances at all the terminals should be large, and be infinity ideally. It can be seen that the transpose of FTFN is itself with X and Y terminals interchanged with W and Z terminals, respectively, under the condition $\alpha \rightarrow 0$, i.e., the resistances at terminals W and Z are infinitely large. The transpose of the FTFN is shown in Figure 4.14.

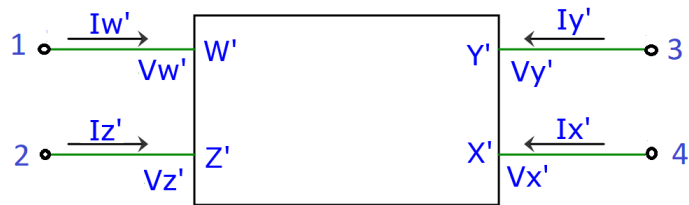


Figure 4.14: The diagram of transposed FTFN

4.3 Band-pass Filters Using FTFN

4.3.1 Current-Mode Band-pass Filter

From the time FTFN has been proposed, it has been considered as an active element that is more flexible, versatile and stable than Op-amp or CCII. Many efforts have been devoted to finding versatile CM filters implemented with FTFN [18, 28-30, 41, 42]. The universal current-mode filter with single FTFN proposed in [28], as shown in Figure 4.15, can realize different types of filters with different passive elements chosen for Y_1-Y_6 , such as first-order all pass filter, second-order low-pass filter, high-pass filter, band-pass filter and notch filter. In the following section, the BPF is studied.

The current transfer function derived from the circuit shown Figure 4.15 [28] is

$$\frac{I_o}{I_{in}} = \frac{y_5 + y_2 \left(\frac{y_5}{y_1} - \frac{y_4}{y_3} \right)}{y_4 + y_2 \left(\frac{y_4}{y_3} - \frac{y_5}{y_1} \right) + y_6 \left(1 + \frac{y_4}{y_3} \right)} \quad (4.11)$$

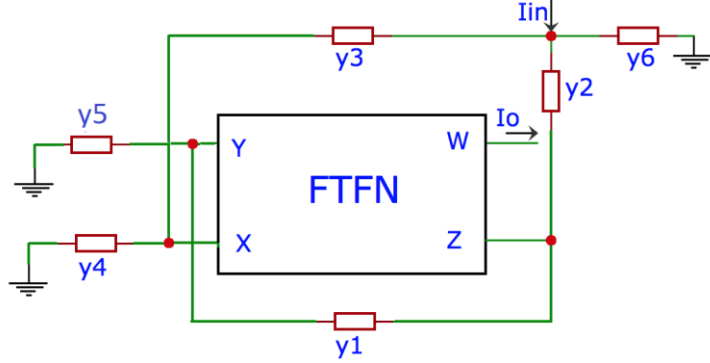


Figure 4.15: Current-mode filter using single FTFN

If $y_1 = sC_1 + \frac{1}{R_1}$, $y_2 = y_3 = y_6 = \frac{1}{R_2}$, $y_5 = y_4 = sC_4$, Equation (4.11) reduces to

$$\frac{I_o}{I_{in}} = \frac{R_1 C s}{3C_1 C R_1 R s^2 + ((-C + C_1)R_1 + 3CR)s + 1} \quad (4.12)$$

which is a BPF, with ω_p and Q_p given by

$$\omega_p = \frac{1}{\sqrt{3C_1 C R_1 R}} \quad (4.13)$$

$$Q_p = \frac{\sqrt{3C_1 C R_1 R}}{3CR + C_1 R_1 - CR_1} \quad (4.14)$$

The schematic of the second order BPF is shown in Figure 4.16.

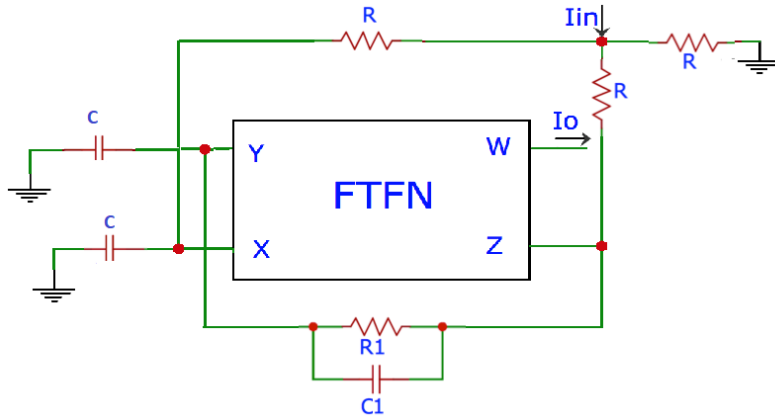


Figure 4.16: Current-mode second-order BPF with single FTFN

4.3.2 Voltage-mode Band-pass Filter Using FTFN

The BPF using the same FTFN with input and output terminals interchanged is shown in Figure 4.17.

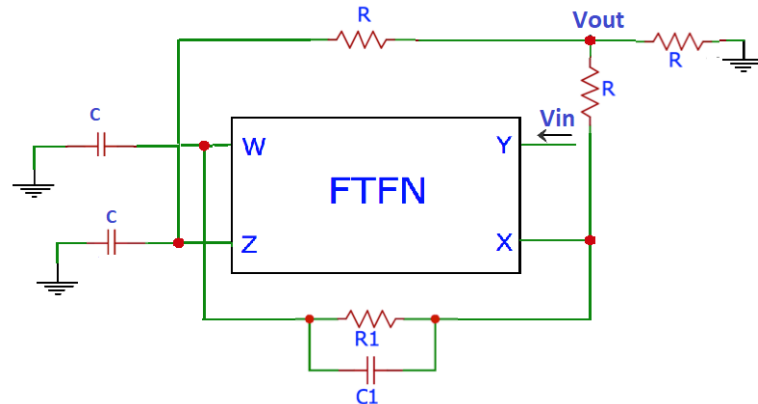


Figure 4.17: VM BPF corresponding to CM BPF using the same FTFN

It can be shown that

$$\frac{V_o}{V_{in}} = \frac{R_1 Cs}{3C_1 CR_1 s^2 + ((-C + C_1)R_1 + 3CR)s + 1} \quad (4.15)$$

Equation (4.15) shows that the VTF using the same FTFN but with its input and output interchanged has exactly the same expression as its original CTF.

4.4 Conclusion

In this Chapter, we have investigated BPF implemented with two other popular CM devices, CCII- and FTFN. Their corresponding transposed BPF circuits are also explored.

CCII- could be a promising device since the transposed CCII- is itself just with the terminals Y and Z interchanged. This property simplifies the design procedure when we switch a filter between VM and CM circuits. The study of BP VTF and transposed CTF using CCII- took into consideration the non-ideal terminal resistances. The results show that the BPF using two CCII- also suffers from finite attenuation at low frequencies, resulting in the BPF behaving as a LPF with a high Q.

FTFN has drawn a lot of attention in CM circuit design since it was first proposed. However, its admittance matrix has never been proposed in any literature, which is critical to find the transposed FTFN. We have managed to propose an admittance matrix of FTFN theoretically. It shows that the transposed FTFN is approximately itself with input and output terminals interchanged when its output resistances at terminals W and Z are very large. A BP VTF has been realized from a BP CTF using the same FTFN. There are no simulation results presented in this thesis regarding realization of BPFs with FTFN. The reason is that there is no satisfactory implementation for FTFN. Although there are many proposed implementations of FTFN in the literature, their performance has not been studied in this thesis. This can be a part of future work.

Comparing the ω_p and Q_p errors of BPFs and their transposes using original MCFOA, proposed MCFOA, and CCII-, one can see that the BPFs using the proposed MCFOA have far more superior

performance than those using MCFOA and CCII- except for VM BPF with $Q_p=3$, in which case BPF using CCII- has the best performance.

Chapter 5

Conclusion and Scope for Future Work

5.1 Conclusion

The concept of network transposition is an elegant, simple and powerful one that connects current and voltage-mode transfer functions. The knowledge based on voltage-mode circuits in the past several decades can be easily transferred to current-mode circuits without significant performance deterioration using transposition. Transposition technique is especially convenient to apply on circuits that use active devices whose transposes are themselves. Examples of such active devices are: OTA, CCII- and MCFOA. In this thesis, substantial work has been carried out to demonstrate the application of transposition to create voltage-mode and current-mode band-pass filters and notch filters using MCFOA, band-pass filters using CCII- and FTFN. The work has established the feasibility of VM to CM (or vice versa) transfer function synthesis and should motivate researchers for future work towards related/associated analysis and performance evaluation.

It has been shown in the literature that for any system function realized with an ideal MCFOA, there are three additional alternative realizations using the same MCFOA by appropriate connections between the terminals of MCFOA and the external passive elements. Thus, there are four voltage-mode configurations for each system function, and four corresponding transposed current-mode configurations. The four VM configurations of BPF and NF using MCFOA and their transposed CM counterparts using the same MCFOA have been investigated in this thesis. Performance comparisons among the four configurations and between VM and CM filters have been presented. The non-ideal parasitic resistances play an important role on the performance of

both VM and CM filters at low frequencies. Theoretically, the effects from non-ideal parasitic resistances can be eliminated by making them ideal. Thus, an improved MCFOA with comparatively more ideal parasitic resistances has been proposed. The proposed MCFOA has resulted in several improvements on the performance of both the VM and CM BPFs, such as more attenuation at low frequencies, and drastic reduction in the ω_p and Q_p errors.

Besides, band-pass filters using two other active devices, CCII- and FTFN, have also been studied. As mentioned before, the transpose of CCII- is itself with terminal Y and Z interchanged. However, no transpose of FTFN exists in the literature. An attempt has been made to define an admittance matrix for FTFN and obtain its transpose. It is shown that the transposed FTFN is itself with input and output terminals interchanged, when the resistances at terminals W and Z are infinitely large. No practical implementation of a FTFN satisfying the ideal terminal characteristics has yet been reported in the literature. Filters using FTFN proposed in the literature are all in current-mode. By determining the transpose of an ideal FTFN, a transposed voltage-mode filter could be obtained.

Results on VM BPF realized using two CCII-s and its transposed CM counterpart using the same two CCII-s have been presented. Similar to the BPF using MCFOA, the parasitic resistances affect the performance of BPFs using CCII- as well. Simulation results show that these BPFs also suffer from finite attenuation at low frequencies.

Finally, a comparison of the ω_p and Q_p errors of BPFs and their transposes using original MCFOA, new improved MCFOA, and CCII- is given. It shows that the BPFs using the proposed improved MCFOA offer the best performance.

In summary, the following contributions have been made in the thesis.

- Thoroughly studied the performance of voltage-mode BPF and NF realized using the original MCFOA, and their corresponding transposed (i.e., current-mode) circuits using the same MCFOA. The performance of the four different equivalent configurations of voltage- and current-mode BPF and NF have been verified by circuit simulation (i.e. Cadence Virtuoso Spectre), as well as numerical (i.e. Matlab) simulations.
- Theoretically analyzed the effect of parasitic resistances on the performance of the filters at low frequencies.
- Proposed an improved MCFOA with more ideal parasitic resistances, and studied the performance improvements of BPF and NF using the proposed MCFOA.
- Proposed an admittance matrix for FTFN, with a goal to arrive at a practical implementation of the device.
- Arrived at a voltage-mode BPF using ideal FTFN from a reported current-mode BPF using the transposition theory.
- The simulation results of BPFs using MCFOA, the improved MCFOA and CCII- are compared.

5.2 Future Work

The implementation of MCFOA in this thesis adopted a Class A output stage, which has a relatively low dynamic range for currents. This causes some transistors of the MCFOA work in the triode mode for some configurations, resulting in degrading the performance of the filters. Moreover, the implementation of FTFN in a practical technological process remains an open challenge. Another open problem is to be able to find or define the transpose of an FTFN. It is also worth studying the design of VM and CM oscillator circuits using MCFOA.

Appendix A

Voltage Mode and Current Mode Band-Pass Filters

In Section 2.3.3, four VM configurations realizing a BPF using an MCFOA were shown in Figure 2.11, and transfer function as well as simulation results for configuration (a) were presented. The corresponding four CM configurations realizing a BPF were shown in Figure 2.16, along with their transfer functions and simulation results for configuration (a) were presented in Section 2.4.1.

In this section, the transfer functions and simulation results of the VM BPF for configurations (b) – (d) of Figure 2.11, along with those for the corresponding CM BPFs shown in Figure 2.16 (b) – (d), are presented. All the numerical and simulation results are obtained by using the same circuit settings as being used in the VM and CM configurations (a) of Figure 2.11 and Figure 2.16 in Sections 2.3 and 2.4, respectively, i.e. $R_1 = R_2 = R_3 = 1K\text{ Ohm}$ and $C_1 = C_2 = 1nF$ for $\omega_p = 1M\text{ rad/s}$ and $Q_p=1$. The only difference for $Q_p=3$ is to let $R_1 = 3K\text{ Ohm}$.

A.1. Configurations (b) of Figure 2.11 and Figure 2.16

Figure A.1 (a) and (b) are the schematics of the VM and the corresponding CM BPF of Configurations (b) shown in Figure 2.11 and Figure 2.16, respectively.

The transfer function is the same for both the VM and CM BPFs, when the MCFOA is ideal, and given by

$$T_{(s)} = \frac{V_{out}}{V_{in}} = \frac{I_{bp}}{I_{in}} = \frac{\frac{1}{C_1 R_1} s}{s^2 + \frac{1}{C_1 R_1} s + \frac{1}{C_1 C_2 R_2 R_3}} \quad (\text{A.1})$$

$$\omega_p = \frac{1}{\sqrt{C_1 C_2 R_2 R_3}}, Q_p = R_1 \sqrt{\frac{C_1}{C_2 R_2 R_3}} \quad (\text{A.2})$$

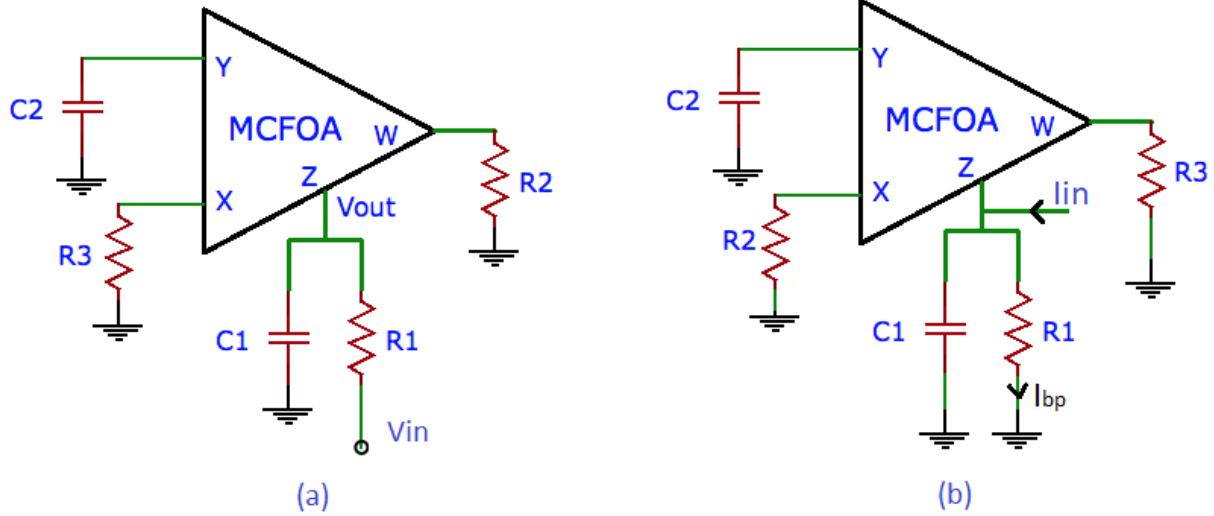


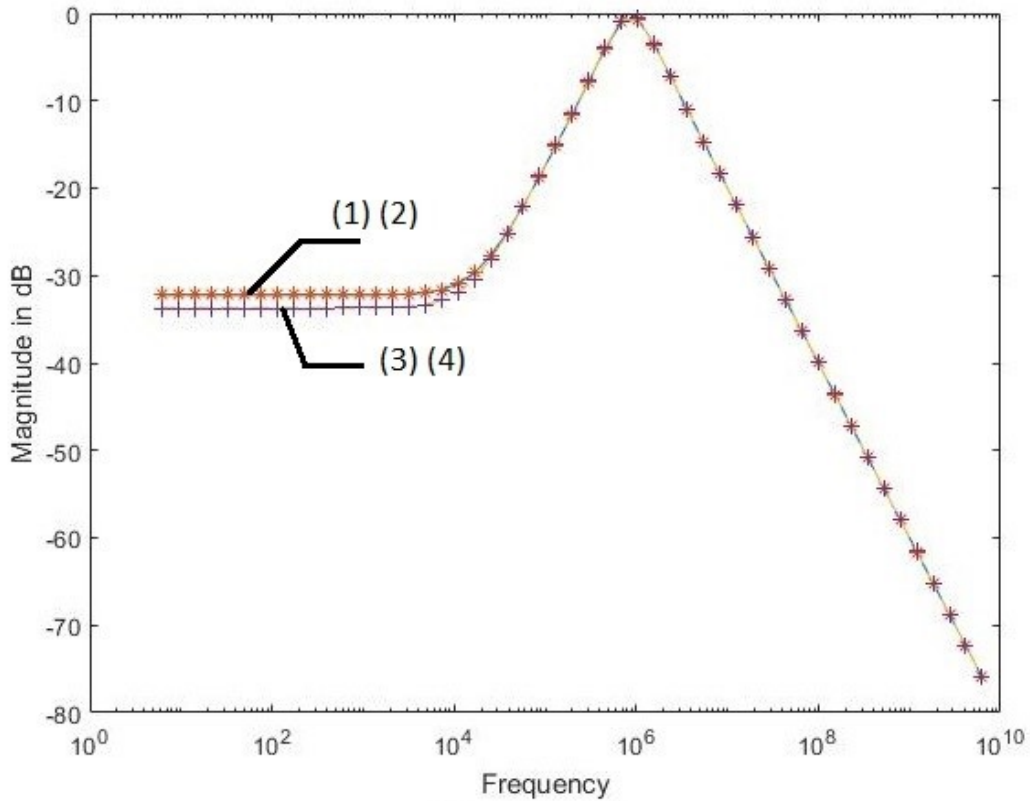
Figure A.1: Schematics of BPF configuration (b)
(a) VM BPF **(b)** CM BPF

The transfer function of the VM BPF taking the terminal resistances of the MCFOA into consideration is

$$T(s) = \frac{V_{out}}{V_{in}} = \frac{(Rz(C2 R2 R3 Ry s + C2 R2 Rx Ry s + C2 R3 Rz Ry s + C2 Rz Rx Ry s + R2 R3 + R2 Rx + R3 Rz + Rz Rx)) / (C1 C2 R1 R2 R3 Ry Rz s^2 + C1 C2 R1 R2 Rx Ry Rz s^2 + C1 C2 R1 R3 Rz Ry Rz s^2 + C1 C2 R1 Rx Ry Rz s^2 + C1 R1 R2 R3 Rz s + C1 R1 R2 Rx Ry Rz s + C1 R1 R3 Ry Rz s + C1 R1 Rx Ry Rz s + C2 R1 R2 R3 Ry s + C2 R1 R2 Rx Ry s + C2 R1 R3 Ry Rz s + C2 R1 Rx Ry Rz s + C2 R2 R3 Ry Rz s + C2 R2 Rx Ry Rz s + C2 R3 Rz Ry Rz s + C2 Rz Rx Ry Rz s + R1 R2 R3 + R1 R2 Rx + R1 R3 Rz + R1 Rx Ry Rz + R2 R3 Rz + R2 Rx Ry Rz + R3 Rz Ry Rz + Rz Rx Ry Rz)}{(C1 C2 R1 R2 R3 Ry Rz s^2 + C1 C2 R1 R2 Rx Ry Rz s^2 + C1 C2 R1 R3 Rz Ry Rz s^2 + C1 C2 R1 Rx Ry Rz s^2 + C1 R1 R2 R3 Rz s + C1 R1 R2 Rx Ry Rz s + C1 R1 R3 Ry Rz s + C1 R1 Rx Ry Rz s + C2 R1 R2 R3 Ry s + C2 R1 R2 Rx Ry s + C2 R1 R3 Ry Rz s + C2 R1 Rx Ry Rz s + C2 R2 R3 Ry Rz s + C2 R2 Rx Ry Rz s + C2 R3 Rz Ry Rz s + C2 Rz Rx Ry Rz s + R1 R2 R3 + R1 R2 Rx + R1 R3 Rz + R1 Rx Ry Rz + R2 R3 Rz + R2 Rx Ry Rz + R3 Rz Ry Rz + Rz Rx Ry Rz)}$$

The transfer function of the CM BPF taking the terminal resistances of the MCFOA into consideration is

$$\begin{aligned}
T(s) = \frac{I_{BP}}{I_{in}} = & C_2 R_2 R_3 R_y R_z s + C_2 R_2 R_w R_y R_z s + C_2 R_3 R_x R_y R_z s + C_2 R_w R_x R_y R_z s + R_2 R_3 R_z \\
& + R_2 R_w R_z + R_3 R_x R_z + R_w R_x R_z / (C_1 C_2 R_1 R_2 R_3 R_y R_z s^2 + C_1 C_2 R_1 R_2 R_w R_y R_z s^2 \\
& + C_1 C_2 R_1 R_3 R_x R_y R_z s^2 + C_1 C_2 R_1 R_w R_x R_y R_z s^2 + C_1 R_1 R_2 R_3 R_z s + C_1 R_1 R_2 R_w R_z s \\
& + C_1 R_1 R_3 R_x R_z s + C_1 R_1 R_w R_x R_z s + C_2 R_1 R_2 R_3 R_y s + C_2 R_1 R_2 R_w R_y s \\
& + C_2 R_1 R_3 R_x R_y s + C_2 R_1 R_w R_x R_y s + C_2 R_2 R_3 R_y R_z s + C_2 R_2 R_w R_y R_z s \\
& + C_2 R_3 R_x R_y R_z s + C_2 R_w R_x R_y R_z s + R_1 R_2 R_3 + R_1 R_2 R_w + R_1 R_3 R_x \\
& + R_1 R_w R_x + R_1 R_y R_z + R_2 R_3 R_z + R_2 R_w R_z + R_3 R_x R_z + R_w R_x R_z)
\end{aligned} \tag{A.4}$$

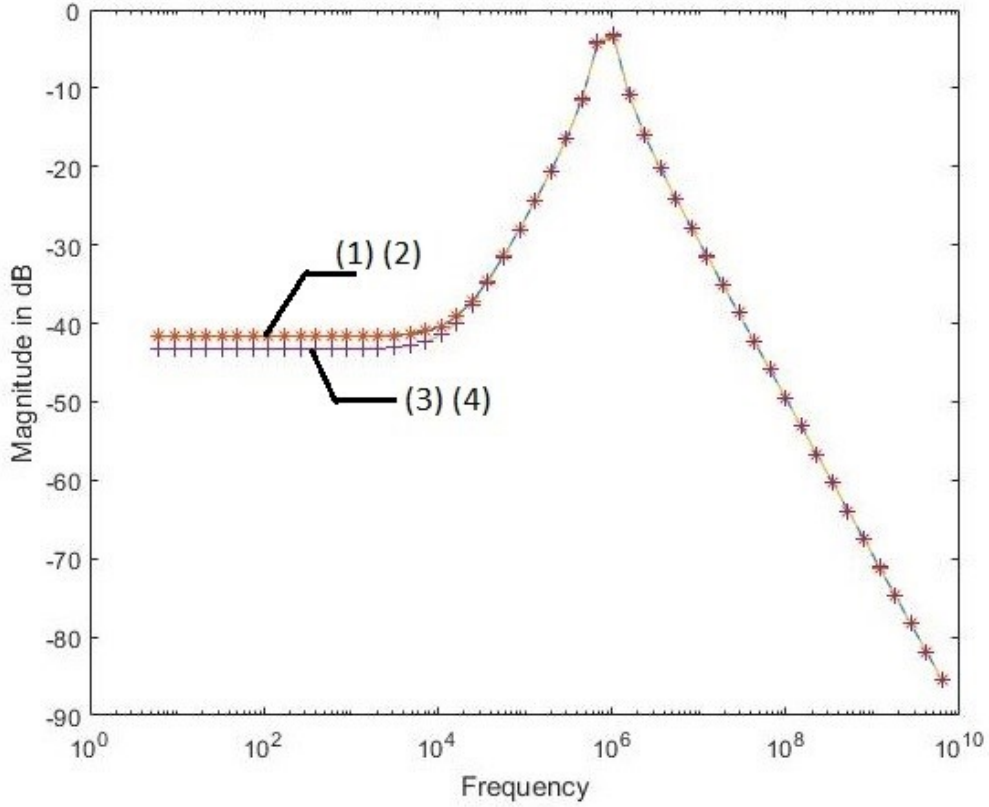


(1)- VM numerical result,(2)* CM numerical result, (3)-- Spice VM result, (4)+ Spice CM result

Figure A.2: Simulation and numerical results for BPF $Q_p = 1$ of Figures A.1 (a) and A.1 (b)

- (1) '-': numerical VM response from Equation (A.3);
- (2) '*': the transposed CM numerical result from Equation (A.4);
- (3) '--': VM response from SPICE simulation of Figure A.1 (a);
- (4) '+': the transposed CM response from SPICE simulation of Figure A.1 (b)

Comparing the VM and CM TFs of Equations (A.3) and (A.4), one can see that they are exactly the same equations, except that the positions of R_2 and R_3 are interchanged. The reason is that the passive components connected to terminals X and W are interchanged as a result of transposition, as has been explained earlier in Section 2.4.



(1)- VM numerical result,(2)* CM numerical result, (3)-- Spice VM result, (4)+ Spice CM result

Figure A.3: Simulation and numerical results for BPF $Q_p = 3$ of Figures A.1 (a) and A.1 (b)

- (1) '-': numerical VM response from Equation (A.3);
- (2) '*': the transposed CM numerical result from Equation (A.4);
- (3) '--': VM response from SPICE simulation of Figure A.1 (a);
- (4) '+': the transposed CM response from SPICE simulation of Figure A.1 (b)

Simulation and numerical results are shown in Figures A.2 and A.3 for $Q_p=1$ and 3, respectively.

The former results are obtained from SPICE simulations of the circuits shown in Figures A.1 (a) and A.1 (b), and the numerical results are obtained using Equations (A.3) and (A.4) for VM and CM BPF, respectively. Figures A.2 and A.3 show that Equations (A.3) and (A.4) can very well model the circuits' behavior. Both the TFs and SPICE simulation results show that the BPF is not actually a BPF, but behaves as a LPF with a high Q, just as in the case of Configuration (a).

A.2. Configurations (c) of Figure 2.11 and Figure 2.16

Figures A.4 (a) and A.4 (b) are the schematics of the VM and the corresponding CM BPF of Configurations (c) shown in Figure 2.11 and Figure 2.16, respectively.

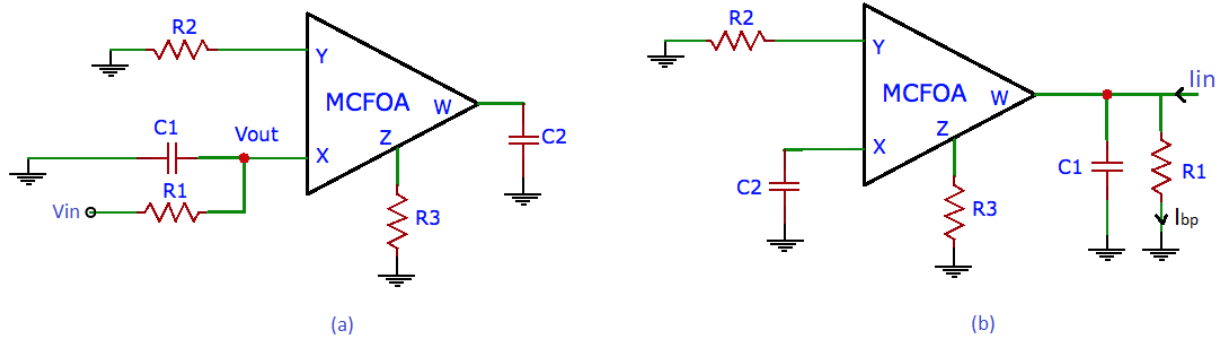


Figure A.4: Schematics of BPF configuration (c)
 (a) VM BPF (b) CM BPF

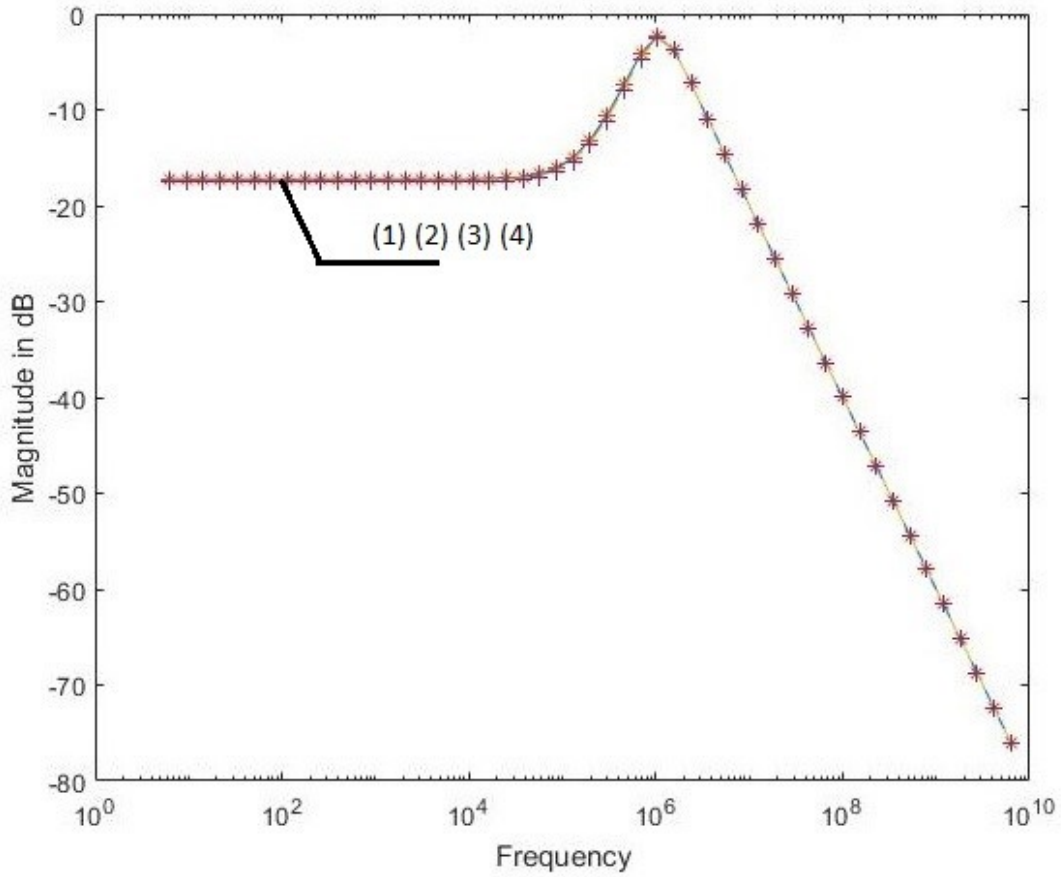
The transfer function is the same for both the VM and CM BPF, when the MCFOA is ideal, and given by:

$$T_{(s)} = \frac{V_{out}}{V_{in}} = \frac{I_{bp}}{I_{in}} = \frac{\frac{1}{C_1 R_1} s}{s^2 + \frac{1}{C_1 R_1} s + \frac{1}{C_1 C_2 R_2 R_3}} \quad (\text{A.5})$$

$$\omega_p = \frac{1}{\sqrt{C_1 C_2 R_2 R_3}}, Q_p = R_1 \sqrt{\frac{C_1}{C_2 R_2 R_3}} \quad (\text{A.6})$$

The transfer function of the VM BPF taking the terminal resistances of the MCFOA into consideration is

$$\begin{aligned}
T(s) = \frac{V_{out}}{V_{in}} = & ((C_2 R_2 R_3 R_w R_x s + C_2 R_2 R_3 R_y R_z s + C_2 R_2 R_w R_x R_z s + C_2 R_3 R_w R_x R_y s \\
& + C_2 R_w R_x R_y R_z s + R_2 R_3 R_x + R_2 R_x R_z + R_3 R_x R_y + R_x R_y R_z)) / \\
& (C_1 C_2 R_1 R_2 R_3 R_w R_x s^2 + C_1 C_2 R_1 R_2 R_3 R_y R_z s^2 + C_1 C_2 R_1 R_2 R_w R_x R_z s^2 \\
& + C_1 C_2 R_1 R_3 R_w R_x R_y s^2 + C_1 C_2 R_1 R_w R_x R_y R_z s^2 + C_1 R_1 R_2 R_3 R_x s \\
& + C_1 R_1 R_2 R_x R_z s + C_1 R_1 R_3 R_x R_y s + C_1 R_1 R_x R_y R_z s + C_2 R_1 R_2 R_3 R_w s \\
& + C_2 R_1 R_2 R_w R_z s + C_2 R_1 R_3 R_w R_y s + C_2 R_1 R_w R_y R_z s + C_2 R_2 R_3 R_w R_x s \\
& + C_2 R_2 R_3 R_y R_z s + C_2 R_2 R_w R_x R_z s + C_2 R_3 R_w R_x R_y s + C_2 R_w R_x R_y R_z s \\
& + R_1 R_2 R_3 + R_1 R_2 R_z + R_1 R_3 R_y + R_1 R_y R_z + R_2 R_3 R_x + R_2 R_x R_z + R_3 R_x R_y \\
& + R_x R_y R_z)
\end{aligned} \tag{A.7}$$



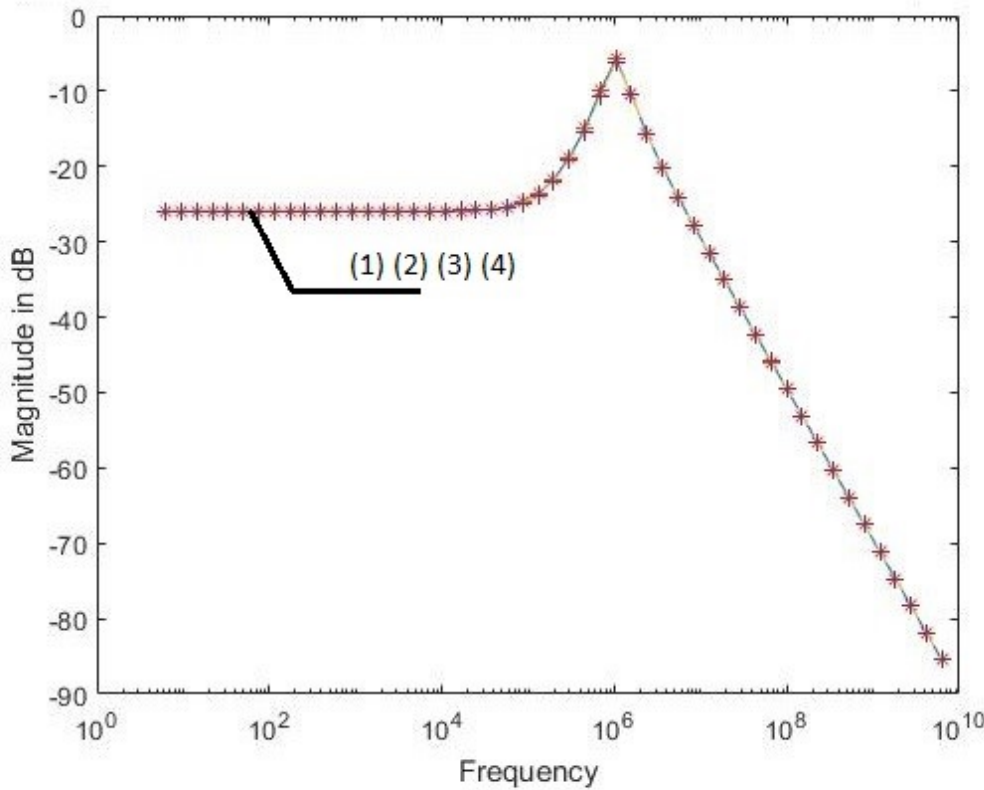
(1)- VM numerical result,(2)* CM numerical result, (3)-- Spice VM result, (4)+ Spice CM result

Figure A.5: Simulation and numerical results for BPF $Q_p = 1$ of Figures A.4 (a) and A.4 (b)

- (1) '-': numerical VM response from Equation (A.7);
- (2) '*': the transposed CM numerical result from Equation (A.8);
- (3) '--': VM response from SPICE simulation of Figure A.4 (a);
- (4) '+': the transposed CM response from SPICE simulation Figure A.4 (b)

The transfer function of the CM BPF taking the terminal resistances of the MCFOA into consideration is

$$\begin{aligned}
 T(s) = \frac{|_{\text{BP}}}{|_{\text{in}}} = & (C_2 R_2 R_3 R_w R_x s + C_2 R_2 R_3 R_y R_z s + C_2 R_2 R_w R_x R_z s + C_2 R_3 R_w R_x R_y s \\
 & + C_2 R_w R_x R_y R_z s + R_2 R_3 R_w + R_2 R_w R_z + R_3 R_w R_y + R_w R_y R_z) / \\
 & (C_1 C_2 R_1 R_2 R_3 R_w R_x s^2 + C_1 C_2 R_1 R_2 R_3 R_y R_z s^2 + C_1 C_2 R_1 R_2 R_w R_x R_z s^2 \\
 & + C_1 C_2 R_1 R_3 R_w R_x R_y s^2 + C_1 C_2 R_1 R_w R_x R_y R_z s^2 + C_1 R_1 R_2 R_3 R_w s \\
 & + C_1 R_1 R_2 R_w R_z s + C_1 R_1 R_3 R_w R_y s + C_1 R_1 R_w R_y R_z s + C_2 R_1 R_2 R_3 R_x s \\
 & + C_2 R_1 R_2 R_x R_z s + C_2 R_1 R_3 R_x R_y s + C_2 R_1 R_x R_y R_z s + C_2 R_2 R_3 R_w R_x s \\
 & + C_2 R_2 R_3 R_y R_z s + C_2 R_2 R_w R_x R_z s + C_2 R_3 R_w R_x R_y s + C_2 R_w R_x R_y R_z s \\
 & + R_1 R_2 R_3 + R_1 R_2 R_z + R_1 R_3 R_y + R_1 R_y R_z + R_2 R_3 R_w + R_2 R_w R_z \\
 & + R_3 R_w R_y + R_w R_y R_z)
 \end{aligned} \quad (\text{A.8})$$



(1)- VM numerical result,(2)* CM numerical result, (3)-- Spice VM result, (4)+ Spice CM result

Figure A.6: Simulation and numerical results for BPF $Q_p = 3$ of Figures A.4 (a) and A.4 (b)

- (1) ‘-’: numerical VM response from Equation (A.7);
- (2) ‘*’: the transposed CM numerical result from Equation (A.8);
- (3) ‘- -’ : VM response from SPICE simulation of Figure A.4 (a);
- (4) ‘+’: the transposed CM response from SPICE simulation Figure A.4 (b)

Comparing VM and CM TF of Equations (A.7) and (A.8), one can find that they are exactly the same equations, except that the positions of R_2 and R_3 are interchanged. The reason, as explained before, is that the passive components connected to terminals X and W are interchanged as a result of transposition.

Simulation and numerical results are shown in Figures A.5 and A.6 for $Q_p=1$ and 3, respectively. The former results are obtained from SPICE simulations of the circuits shown in Figures A.4 (a) and A.4 (b), and the numerical results are obtained using Equations (A.7) and (A.8) for VM and CM BPF, respectively. They show that Equations (A.7) and (A.8) can model the circuits' behavior accurately. Both the TFs and SPICE simulation results show that the BPF is not actually a BPF, but behaves as a LPF with a high Q, as was the case for configuration (a) and (b).

A.3. Configurations (d) of Figure 2.11 and Figure 2.16

Figures A.7 (a) and A.7 (b) are the schematics of the VM and the corresponding CM BPF of Configurations (d) shown in Figure 2.11 and Figure 2.16, respectively.

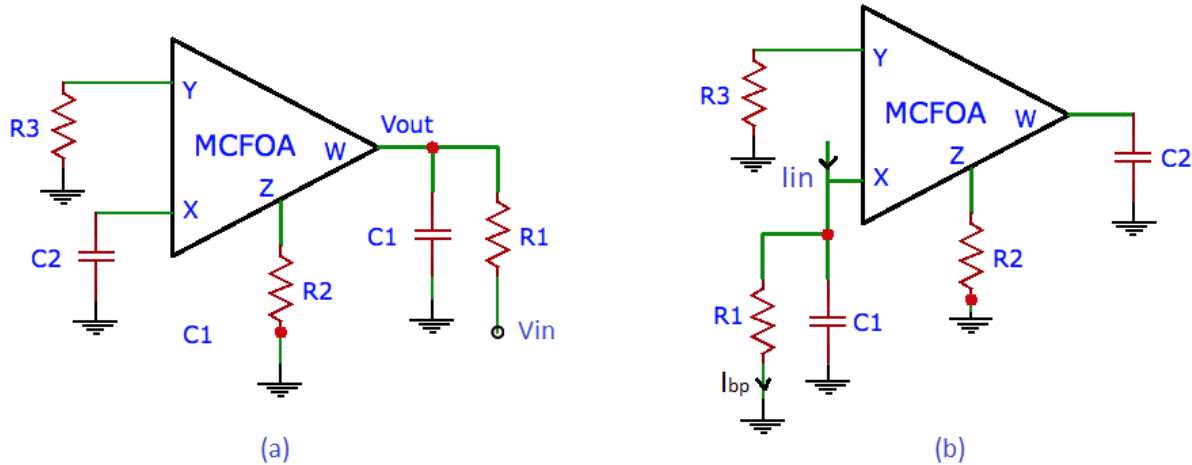


Figure A.7: Schematics of BPF configuration (d) of Figure 2.11
 (a) VM BPF (b) CM BPF

The transfer function is the same for both the VM and CM BPF, when the MCFOA is ideal, and given by:

$$T_{(s)} = \frac{V_{out}}{V_{in}} = \frac{I_{bp}}{I_{in}} = \frac{\frac{1}{C_1 R_1} s}{s^2 + \frac{1}{C_1 R_1} s + \frac{1}{C_1 C_2 R_2 R_3}} \quad (\text{A.9})$$

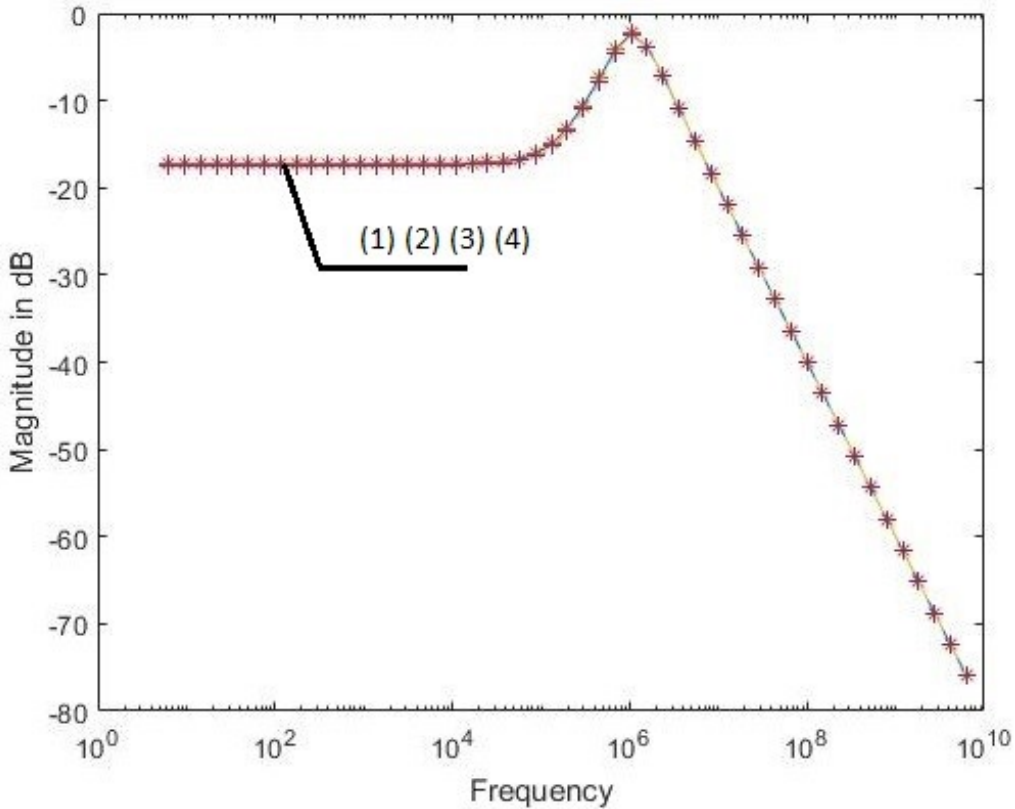
$$\omega_p = \frac{1}{\sqrt{C_1 C_2 R_2 R_3}}, Q_p = R_1 \sqrt{\frac{C_1}{C_2 R_2 R_3}} \quad (\text{A.10})$$

The transfer function of the VM BPF taking the terminal resistances of the MCFOA into consideration is

$$\begin{aligned} T(s) = \frac{V_{out}}{V_{in}} = & ((C_2 R_2 R_3 R_w R_x s + C_2 R_2 R_3 R_y R_z s + C_2 R_2 R_w R_x R_y s + C_2 R_3 R_w R_x R_z s \\ & + C_2 R_w R_x R_y R_z s + R_2 R_3 R_w + R_2 R_w R_y + R_3 R_w R_z + R_w R_y R_z) / \\ & (C_1 C_2 R_1 R_2 R_3 R_w R_x s^2 + C_1 C_2 R_1 R_2 R_3 R_y R_z s^2 + C_1 C_2 R_1 R_2 R_w R_x R_y s^2 \\ & + C_1 C_2 R_1 R_3 R_w R_x R_z s^2 + C_1 C_2 R_1 R_w R_x R_y R_z s^2 + C_1 R_1 R_2 R_3 R_w s \\ & + C_1 R_1 R_2 R_w R_y s + C_1 R_1 R_3 R_w R_z s + C_1 R_1 R_w R_y R_z s + C_2 R_1 R_2 R_3 R_x s \\ & + C_2 R_1 R_2 R_x R_y s + C_2 R_1 R_3 R_x R_z s + C_2 R_1 R_w R_y R_z s + C_2 R_2 R_3 R_w R_x s \\ & + C_2 R_2 R_3 R_y R_z s + C_2 R_2 R_w R_x R_y s + C_2 R_3 R_w R_x R_z s + C_2 R_w R_x R_y R_z s \\ & + R_1 R_2 R_3 + R_1 R_2 R_y + R_1 R_3 R_z + R_1 R_y R_z + R_2 R_3 R_w + R_2 R_w R_y + R_3 R_w R_z \\ & + R_w R_y R_z) \end{aligned} \quad (\text{A.11})$$

The transfer function of the CM BPF taking the terminal resistances of the MCFOA into consideration is

$$\begin{aligned} T(s) = \frac{I_{BP}}{I_{in}} = & (C_2 R_2 R_3 R_w R_x s + C_2 R_2 R_3 R_y R_z s + C_2 R_2 R_w R_x R_y s + C_2 R_3 R_w R_x R_z s \\ & + C_2 R_w R_x R_y R_z s + R_2 R_3 R_x + R_2 R_x R_y + R_3 R_x R_z + R_x R_y R_z) / \\ & (C_1 C_2 R_1 R_2 R_3 R_w R_x s^2 + C_1 C_2 R_1 R_2 R_3 R_y R_z s^2 + C_1 C_2 R_1 R_2 R_w R_x R_y s^2 \\ & + C_1 C_2 R_1 R_3 R_w R_x R_z s^2 + C_1 C_2 R_1 R_w R_x R_y R_z s^2 + C_1 R_1 R_2 R_3 R_x s \\ & + C_1 R_1 R_2 R_x R_y s + C_1 R_1 R_3 R_x R_z s + C_1 R_1 R_w R_y R_z s + C_2 R_1 R_2 R_3 R_w s \\ & + C_2 R_1 R_2 R_w R_y s + C_2 R_1 R_3 R_w R_z s + C_2 R_1 R_w R_y R_z s + C_2 R_2 R_3 R_w R_x s \\ & + C_2 R_2 R_3 R_y R_z s + C_2 R_2 R_w R_x R_y s + C_2 R_3 R_w R_x R_z s + C_2 R_w R_x R_y R_z s \\ & + R_1 R_2 R_3 + R_1 R_2 R_y + R_1 R_3 R_z + R_1 R_y R_z + R_2 R_3 R_x + R_2 R_x R_y \\ & + R_3 R_x R_z + R_x R_y R_z) \end{aligned} \quad (\text{A.12})$$



(1)- VM numerical result,(2)* CM numerical result, (3)-- Spice VM result, (4)+ Spice CM result

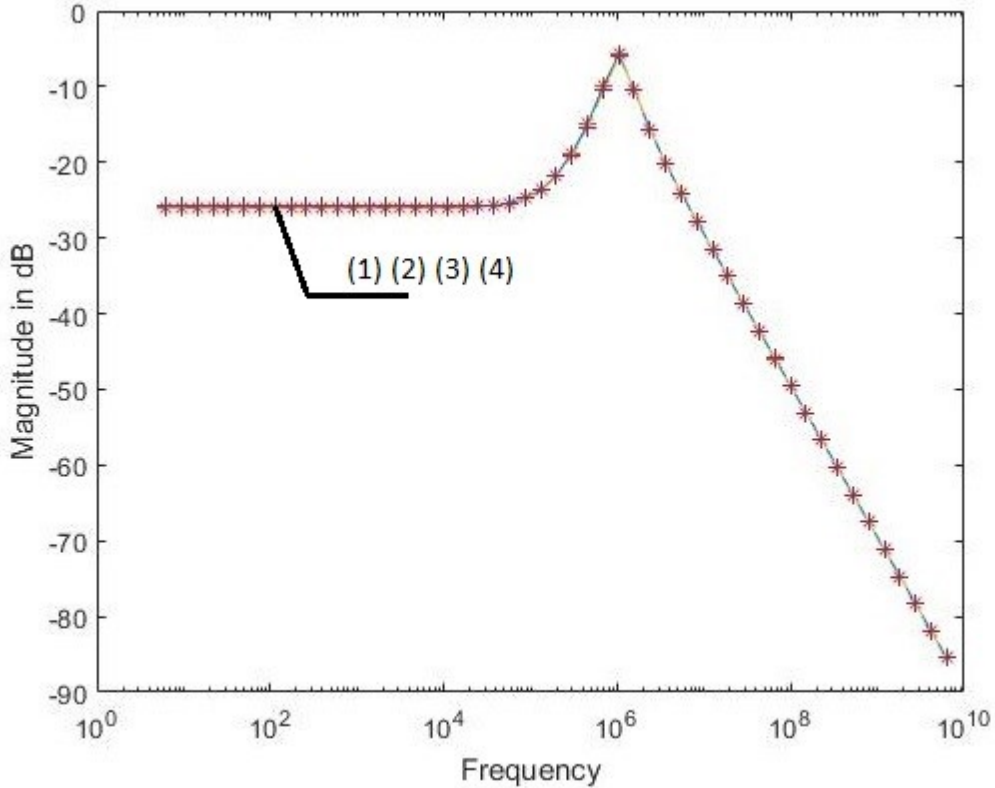
Figure A.8: Simulation and numerical results for BPF $Q_p = 1$ of Figures A.7 (a) and A.7 (b)

- (1) ‘-’: numerical VM response from Equation (A.11);
- (2) ‘*’: the transposed CM numerical result from Equation (A.12);
- (3) ‘- -’ : VM response from SPICE simulation of Figure A.7 (a);
- (4) ‘+’: the transposed CM response from SPICE simulation Figure A.7 (b)

Comparing VM and CM TF of Equations (A.11) and (A.12), one can find that they are exactly the same equations, except that the positions of R_2 and R_3 are interchanged. The reason, as explained before, is that the passive components connected to terminals X and W are interchanged as a result of transposition.

Simulation and numerical results are shown in Figures A.8 and A.9 for $Q_p=1$ and 3, respectively. The former results are obtained from SPICE simulations of the circuits shown in Figures A.7 (a) and A.7 (b), and the numerical results are obtained using Equations (A.11) and (A.12) for VM and

CM BPF, respectively. They show that Equations (A.11) and (A.12) can model the circuits' behavior accurately. Both the TFs and SPICE simulation results show that the BPF is not actually a BPF, but behaves as a LPF with a high Q, as was the case for configuration (a), (b) and (c).



(1)- VM numerical result,(2)* CM numerical result, (3)-- Spice VM result, (4)+ Spice CM result

Figure A.9: Simulation and numerical results for BPF $Q_p = 3$ of Figures A.7 (a) and A.7 (b)

- (1) ‘-’: numerical VM response from Equation (A.11);
- (2) ‘*’: the transposed CM numerical result from Equation (A.12);
- (3) ‘- -’ : VM response from SPICE simulation of Figure A.7 (a);
- (4) ‘+’: the transposed CM response from SPICE simulation Figure A.7 (b)

Appendix B

Voltage Mode and Current Mode Notch Filters

In Section 2.3.4, we considered the VM notch filter obtained from configuration (a) (See Figure 2.14), and derived the transfer function as well as simulation results, assuming $R_1 = R_2 = R_3 = 1K\text{ Ohm}$ and $C_1 = C_2 = 1nF$ for $\omega_p = 1M\text{ rad/s}$ and $Q_p=1$, as well as for $Q_p=3$ assuming $R_1 = 3K\text{ Ohm}$ with the other resistors and capacitors remaining the same. The corresponding CM notch filter derived by adding the HPF and LPF responses (see Figure 2.18) was considered in Section 2.4.2. Again for $Q_p=1$ and $Q_p=3$, the simulation results as well as the theoretical responses were obtained. In this Appendix, we will discuss the simulation results for the remaining configurations (b), (c) and (d) for both VM and CM notch filters.

B.1 Configurations (b) of Figure 2.11 and Figure 2.16

The schematics of VM NF of configuration (b) of Figure 2.11 is shown in Figure B.1 (a). The corresponding TF is given by

$$T(s) = \frac{V_{in}}{V_{out}} = \frac{s^2 + \frac{1}{R_2 R_3 C_1 C_2}}{s^2 + s \frac{1}{R_1 C_1} + \frac{1}{R_2 R_3 C_1 C_2}} \quad (\text{B.1})$$

Figure B.1 (b) shows the CM filter for configuration (b) realizing LP and HP responses. In Section 2.4.2, we obtained the NF for configuration (a) by adding the HP and LP responses. However, by looking at Table 2.8, we see that it is not possible to obtain the CM NF in configuration (b) by

adding I_{lp} and I_{hp} , since the numerator will not be of the form $s^2 + \omega_z^2$ but is of the form $s^2 - \omega_z^2$.

Thus, it is not possible to obtain a NF response in configuration (b).

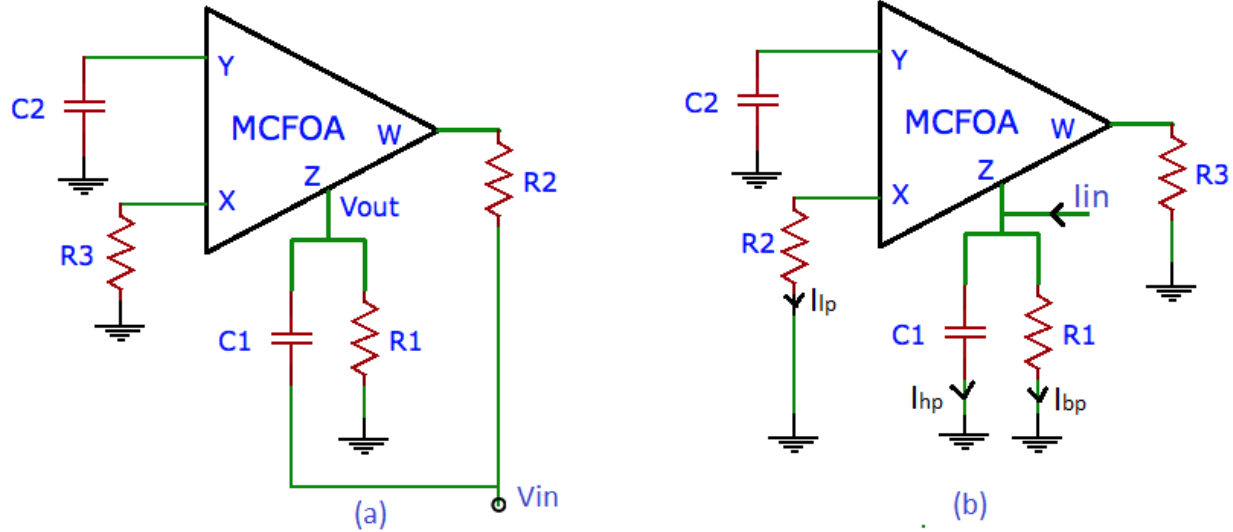


Figure B.1: (a) Schematic of VM NF configuration (b) of Figure 2.11
(b) Schematic of CM configuration (b) realizing LP and HP responses

The transfer function of the VM NF taking the terminal resistances of MCFOA into consideration is

$$\begin{aligned} T(s) = \frac{V_{out}}{V_{in}} = & \left(R_1 R_z (C_1 C_2 R_2 R_3 R_y s^2 + C_1 C_2 R_2 R_x R_y s^2 + C_1 C_2 R_3 R_w R_y s^2 + C_1 C_2 R_w R_x R_y s^2 \right. \\ & + C_1 R_2 R_3 s + C_1 R_2 R_x s + C_1 R_3 R_w s + C_1 R_w R_x s + R_y) \Big) / (C_1 C_2 R_1 R_2 R_3 R_y R_z s^2 \\ & + C_1 C_2 R_1 R_2 R_x R_y R_z s^2 + C_1 C_2 R_1 R_3 R_w R_y R_z s^2 + C_1 C_2 R_1 R_w R_x R_y R_z s^2 \\ & + C_1 R_1 R_2 R_3 R_z s + C_1 R_1 R_2 R_x R_z s + C_1 R_1 R_3 R_w R_z s + C_1 R_1 R_w R_x R_z s \\ & + C_2 R_1 R_2 R_3 R_y s + C_2 R_1 R_2 R_x R_y s + C_2 R_1 R_3 R_w R_y s + C_2 R_1 R_w R_x R_y s \\ & + C_2 R_2 R_3 R_y R_z s + C_2 R_2 R_x R_y R_z s + C_2 R_3 R_w R_y R_z s + C_2 R_w R_x R_y R_z s \\ & + R_1 R_2 R_3 + R_1 R_2 R_x + R_1 R_3 R_w + R_1 R_w R_x + R_1 R_y R_z + R_2 R_3 R_z + R_2 R_x R_z \\ & \left. + R_3 R_w R_z + R_w R_x R_z \right) \end{aligned} \quad (B.2)$$

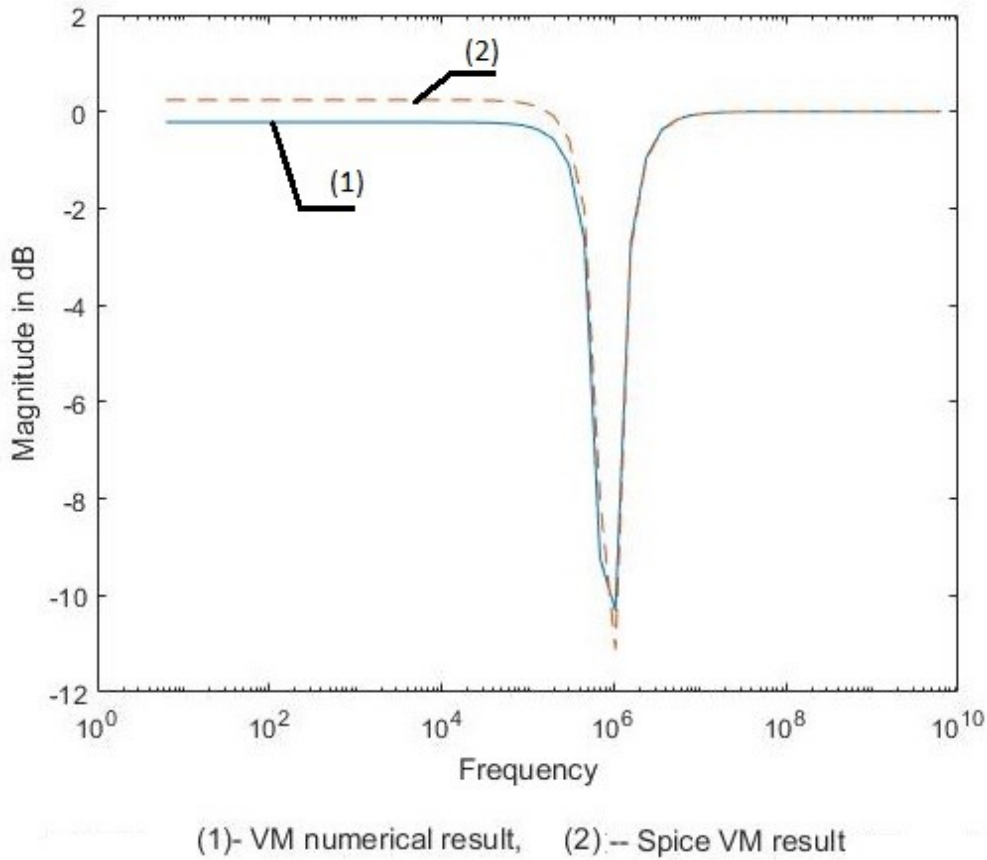


Figure B.2: Simulation and numerical results for NF $Q_p = 1$ of Figure B.1 (a)
 (1) ‘-’: numerical VM response from Equation (B.2);
 (2) ‘- -’: VM response from SPICE simulation of Figure B.1 (a);

Simulation and numerical results are shown in Figure B.2 and Figure B.3 for $Q_p=1$ and 3, respectively. The simulation results are obtained from SPICE simulation of the circuit shown in Figure B.1 (a), and the numerical results are obtained using Equation (B.2) for VM NF. They show that Equation (B.2) can approximately model the circuits’ behavior.

It is seen from (B.2) that ω_p and ω_z may not be equal when the MCFOA is not ideal. This is a factor that degrades the performance of the VM NF.

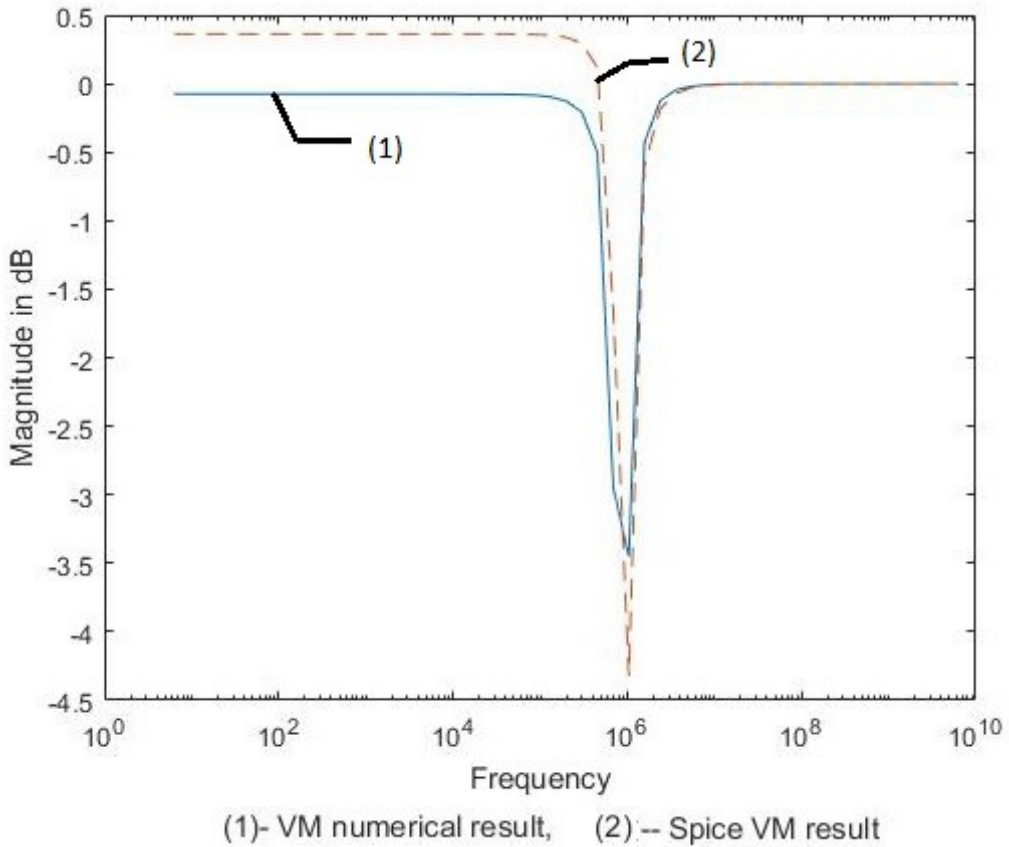


Figure B.3: Simulation and numerical results for NF $Q_p = 3$ of Figure B.1 (a)
 (1) ‘-’: numerical VM response from Equation (B.2);
 (2) ‘- -’: VM response from SPICE simulation of Figure B.1 (a);

B.2 Configurations (c) of Figure 2.11 and Figure 2.16

The schematics of VM and CM NF of configurations (c) of Figure 2.11 and Figure 2.16 are shown in Figures B.4 (a) and (b), respectively.

The VTF and CTF of the NF, assuming the MCFOA to be ideal, are given by

$$T(s) = \frac{V_{in}}{V_{out}} = \frac{s^2 + \frac{1}{R_2 R_3 C_1 C_2}}{s^2 + s \frac{1}{R_1 C_1} + \frac{1}{R_2 R_3 C_1 C_2}} \quad (\text{B.3})$$

$$T(s) = \frac{I_{Ntch}}{I_{in}} = \frac{s^2 + \frac{1}{R_2 R_3 C_1 C_2}}{s^2 + s \frac{1}{R_1 C_1} + \frac{1}{R_2 R_3 C_1 C_2}} \quad (\text{B.4})$$

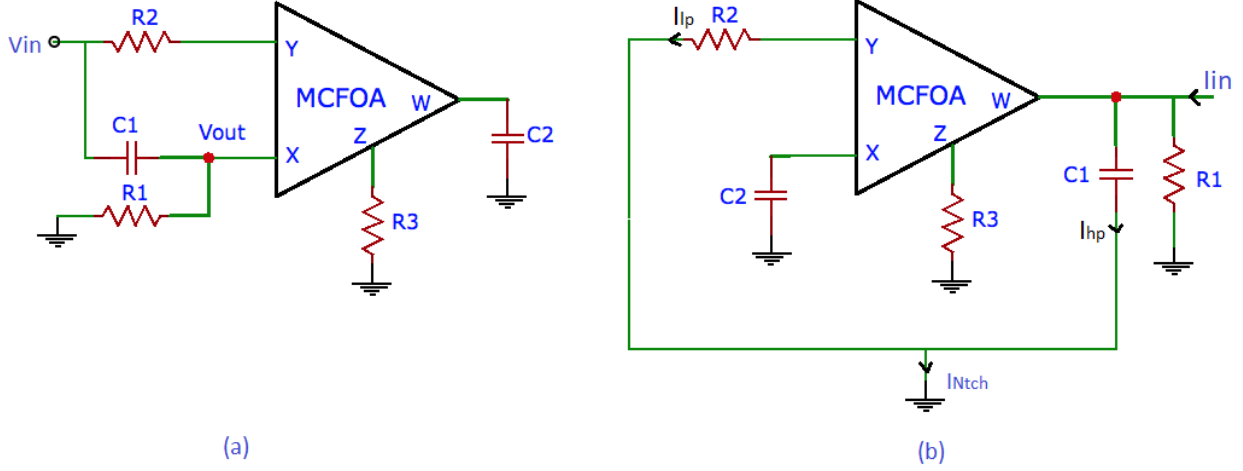


Figure B.4: Schematics of NF configuration (c) of Figure 2.11 and Figure 2.16
 (a) VM BPF (b) CM BPF

The transfer function of the VM NF taking the terminal resistances of the MCFOA into consideration is

$$T(s) = \frac{V_{out}}{V_{in}} = \left(R1 \left(C1 C2 R2 R3 R w R x s^2 + C1 C2 R2 R3 R y R z s^2 + C1 C2 R2 R w R x R z s^2 + C1 C2 R3 R w R x R y s^2 + C1 C2 R w R x R y R z s^2 + C1 R2 R3 R x s + C1 R2 R x R z s + C1 R3 R x R y s + C1 R x R y R z s + C2 R3 R w R y s + C2 R w R y R z s + R3 R y + R y R z \right) \right) / \\ \left(C1 C2 R1 R2 R3 R w R x s^2 + C1 C2 R1 R2 R3 R y R z s^2 + C1 C2 R1 R2 R w R x R z s^2 + C1 C2 R1 R3 R w R x R y s^2 + C1 C2 R1 R w R x R y R z s^2 + C1 R1 R2 R3 R x s + C1 R1 R2 R x R z s + C1 R1 R3 R x R y s + C1 R1 R x R y R z s + C2 R1 R2 R3 R w s + C2 R1 R2 R w R z s + C2 R1 R3 R w R y s + C2 R1 R w R y R z s + C2 R2 R3 R w R x s + C2 R2 R3 R y R z s + C2 R2 R w R x R z s + C2 R3 R w R x R y s + C2 R w R x R y R z s + R1 R2 R3 + R1 R2 R z + R1 R3 R y + R1 R y R z + R2 R3 R x + R2 R x R z + R3 R x R y + R x R y R z \right) \quad (B.5)$$

The transfer function of the CM NF taking the terminal resistances of the MCFOA into consideration is

$$\begin{aligned}
T(s) = \frac{I_{NTCH}}{I_{lin}} = & \left(\left(C_1 C_2 R_2 R_3 R_w R_x s^2 + C_1 C_2 R_2 R_3 R_y R_z s^2 + C_1 C_2 R_2 R_w R_x R_z s^2 + C_1 C_2 R_3 R_w R_x R_y s^2 \right. \right. \\
& + C_1 C_2 R_w R_x R_y R_z s^2 + C_1 R_2 R_3 R_w s + C_1 R_2 R_w R_z s + C_1 R_3 R_w R_v s + C_1 R_w R_y R_z s \\
& + C_2 R_3 R_x R_y s + C_2 R_x R_y R_z s + R_3 R_v + R_v R_z \Big) R_1 \Big) / \left(C_1 C_2 R_1 R_2 R_3 R_w R_x s^2 \right. \\
& + C_1 C_2 R_1 R_2 R_3 R_y R_z s^2 + C_1 C_2 R_1 R_2 R_w R_x R_z s^2 + C_1 C_2 R_1 R_3 R_w R_x R_y s^2 \\
& + C_1 C_2 R_1 R_w R_x R_y R_z s^2 + C_1 R_1 R_2 R_3 R_w s + C_1 R_1 R_2 R_w R_z s + C_1 R_1 R_3 R_w R_y s \\
& + C_1 R_1 R_w R_y R_z s + C_2 R_1 R_2 R_3 R_x s + C_2 R_1 R_2 R_x R_z s + C_2 R_1 R_3 R_x R_y s \\
& + C_2 R_1 R_x R_y R_z s + C_2 R_2 R_3 R_w R_x s + C_2 R_2 R_3 R_y R_z s + C_2 R_2 R_w R_x R_z s \\
& + C_2 R_3 R_w R_x R_y s + C_2 R_w R_x R_y R_z s + R_1 R_2 R_3 + R_1 R_2 R_z + R_1 R_3 R_y + R_1 R_y R_z \\
& \left. \left. + R_2 R_3 R_w + R_2 R_w R_z + R_3 R_w R_y + R_w R_y R_z \right) \right) \quad (B.6)
\end{aligned}$$

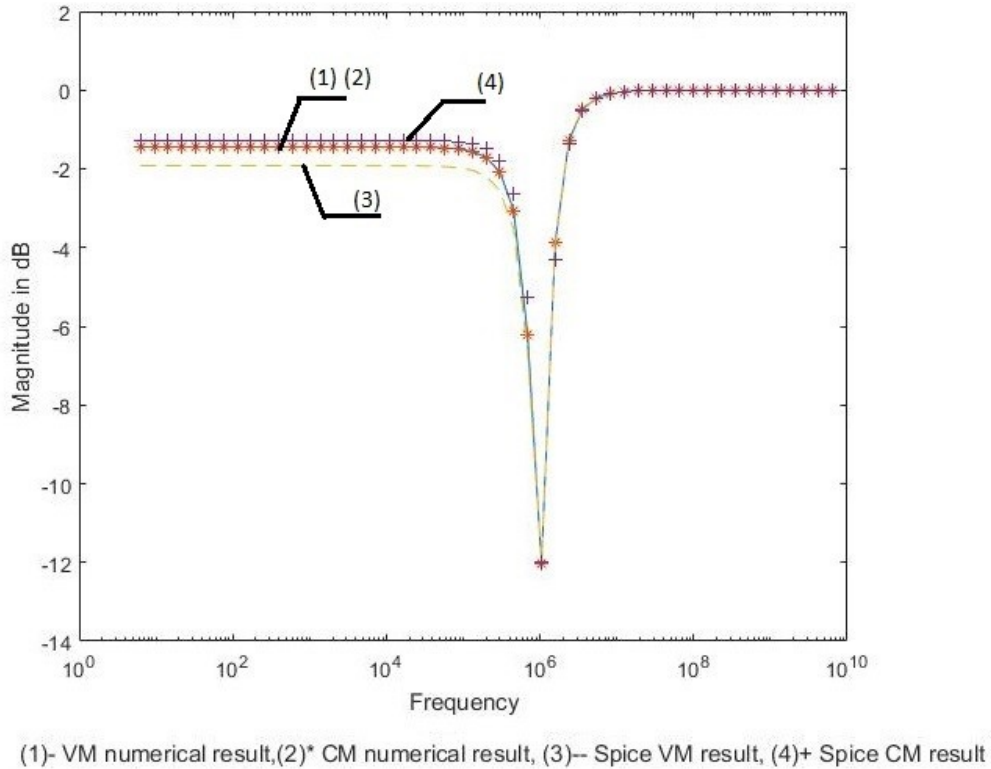


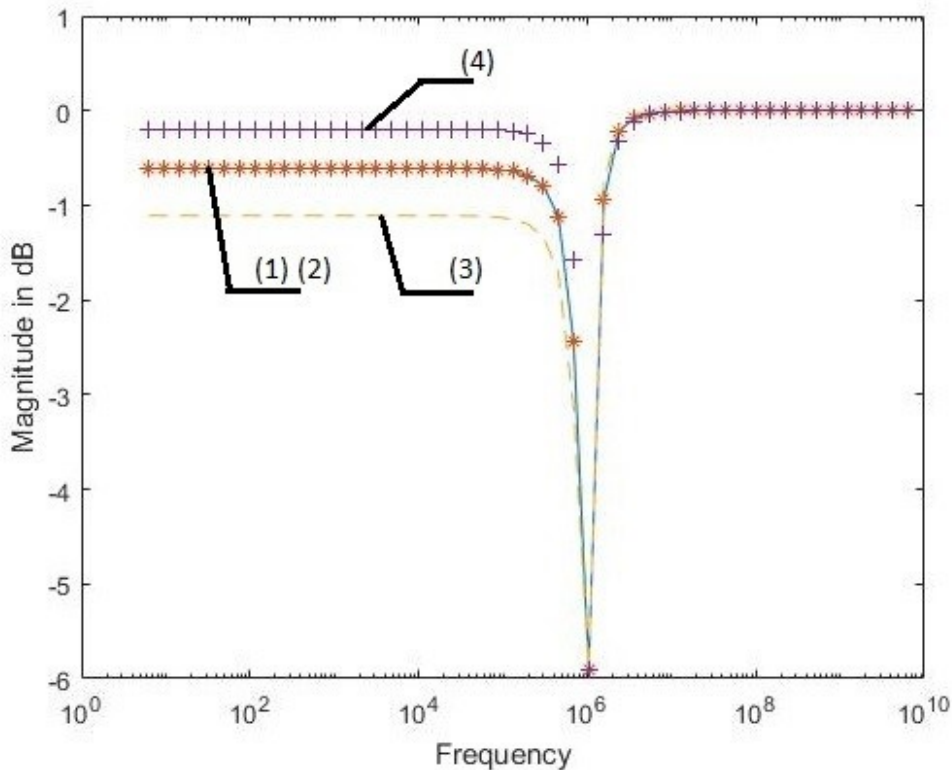
Figure B.5: Simulation and numerical results for NF $Q_p = 1$ of Figures B.4 (a) and B.4 (b)

- (1) ‘-’: numerical VM response from Equation (B.5);
- (2) ‘*’: the transposed CM numerical result from Equation (B.6);
- (3) ‘- -’ : VM response from SPICE simulation of Figure B.4 (a);
- (4) ‘+’: the transposed CM response from SPICE simulation Figure B.4 (b)

The values of ω_p and ω_z may not equal when the MCFOA is not ideal. This is a factor that degrades the performance of NF.

Comparing VM and CM TFs of Equations (B.5) and (B.6), one can find that they are exactly the same equations, except that the positions of R_x and R_w are interchanged. The reason is that the passive components connected to terminals X and W are interchanged as a result of transposition.

Simulation and numerical results are shown in Figure B.5 and Figure B.6 for $Q_p=1$ and 3, respectively. The simulation results are obtained from SPICE simulations of the circuits shown in Figures B.4 (a) and (b), respectively, and the corresponding numerical results are obtained using Equations (B.5) and (B.6). They show that Equations (B.5) and (B.6) can approximately model the circuits' behavior.



(1)- VM numerical result,(2)* CM numerical result, (3)-- Spice VM result, (4)+ Spice CM result

Figure B.6: Simulation and numerical results for NF $Q_p = 3$ of Figures B.4 (a) and B.4 (b)

- (1) ‘-’: numerical VM response from Equation (B.5);
- (2) ‘*’: the transposed CM numerical result from Equation (B.6);
- (3) ‘- -’ : VM response from SPICE simulation of Figure B.4 (a);
- (4) ‘+’: the transposed CM response from SPICE simulation Figure B.4 (b)

B.3 Configurations (d) of Figure 2.11 and Figure 2.16

The schematic of VM NF of configuration (d) of Figure 2.11 is shown in Figure B.7 (a). The corresponding TF when MCFOA is ideal is given by

$$T(s) = \frac{V_{in}}{V_{out}} = \frac{s^2 + \frac{1}{R_2 R_3 C_1 C_2}}{s^2 + s \frac{1}{R_1 C_1} + \frac{1}{R_2 R_3 C_1 C_2}} \quad (\text{B.7})$$

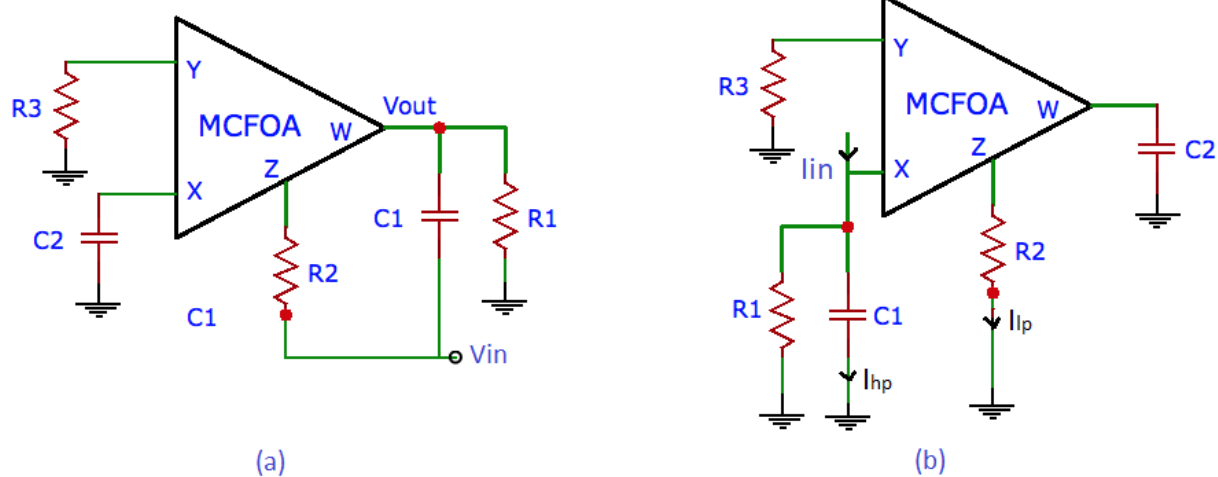


Figure B.7: (a) Schematic of VM NF configuration (d) of Figure 2.11
(b) Schematic of CM configuration realizing LP and HP responses

Figure B.7 (b) shows the CM filter for configuration (d). Again, by observing the LPF and HPF transfer function (Table 2.8), we see that it is not possible to obtain the CM NF in configuration (d) by adding I_{lp} and I_{hp} , since the numerator will not be of the form $s^2 + \omega_z^2$ but is of the form $s^2 - \omega_z^2$. The values of ω_p and ω_z for the VM NF may not equal when the MCFOA is not ideal. This is a factor that degrades the performance of VM NF.

The transfer function of the VM NF taking the terminal resistances of the MCFOA into consideration is

$$T(s) = \frac{V_{\text{out}}}{V_{\text{in}}} = \frac{(R1(C1 C2 R2 R3 R_w R_x s^2 + C1 C2 R2 R3 R_y R_z s^2 + C1 C2 R2 R_w R_x R_y s^2 + C1 C2 R3 R_w R_x R_z s^2 + C1 C2 R_w R_x R_y R_z s^2 + C1 R2 R3 R_w s + C1 R2 R_w R_y s + C1 R3 R_w R_z s + C1 R_w R_y R_z s + C2 R3 R_x R_z s + C2 R_x R_y R_z s + R3 R_z + R_y R_z))}{(C1 C2 R1 R2 R3 R_w R_x s^2 + C1 C2 R1 R2 R3 R_y R_z s^2 + C1 C2 R1 R2 R_w R_x R_y s^2 + C1 C2 R1 R3 R_w R_x R_z s^2 + C1 C2 R1 R_w R_x R_y R_z s^2 + C1 R1 R2 R3 R_w s + C1 R1 R2 R_w R_y s + C1 R1 R3 R_w R_z s + C1 R1 R_w R_y R_z s + C2 R1 R2 R3 R_x s + C2 R1 R2 R_x R_y s + C2 R1 R3 R_x R_z s + C2 R1 R_x R_y R_z s + C2 R2 R3 R_w R_x s + C2 R2 R_w R_x R_y s + C2 R3 R_w R_x R_z s + C2 R_w R_x R_y R_z s + R1 R2 R3 + R1 R2 R_y + R1 R3 R_z + R1 R_y R_z + R2 R3 R_w + R2 R_w R_y + R3 R_w R_z + R_w R_y R_z)} \quad (\text{B.8})$$

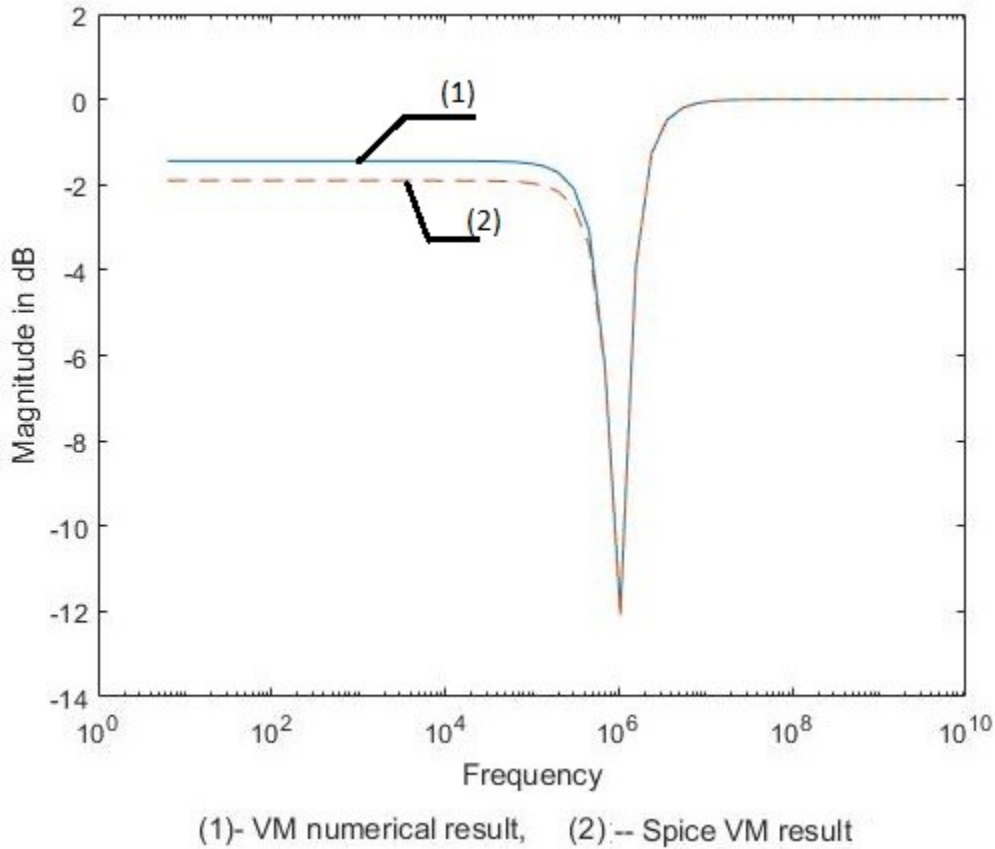


Figure B.8: Simulation and numerical results for NF $Q_p = 1$ of Figure B.7 (a)
 (1) ‘-’: numerical VM response from Equation (B.8);
 (2) ‘- -’: VM response from SPICE simulation of Figure B.7 (a);

Simulation and numerical results are shown in Figure B.8 and Figure B.9 for $Q_p = 1$ and 3, respectively. The simulation results are obtained from SPICE simulation of the circuit shown in Figure B.7 (a), and the numerical results are obtained using Equation (B.8) for VM NF. They show that Equation (B.8) can approximately model the circuits' behavior.

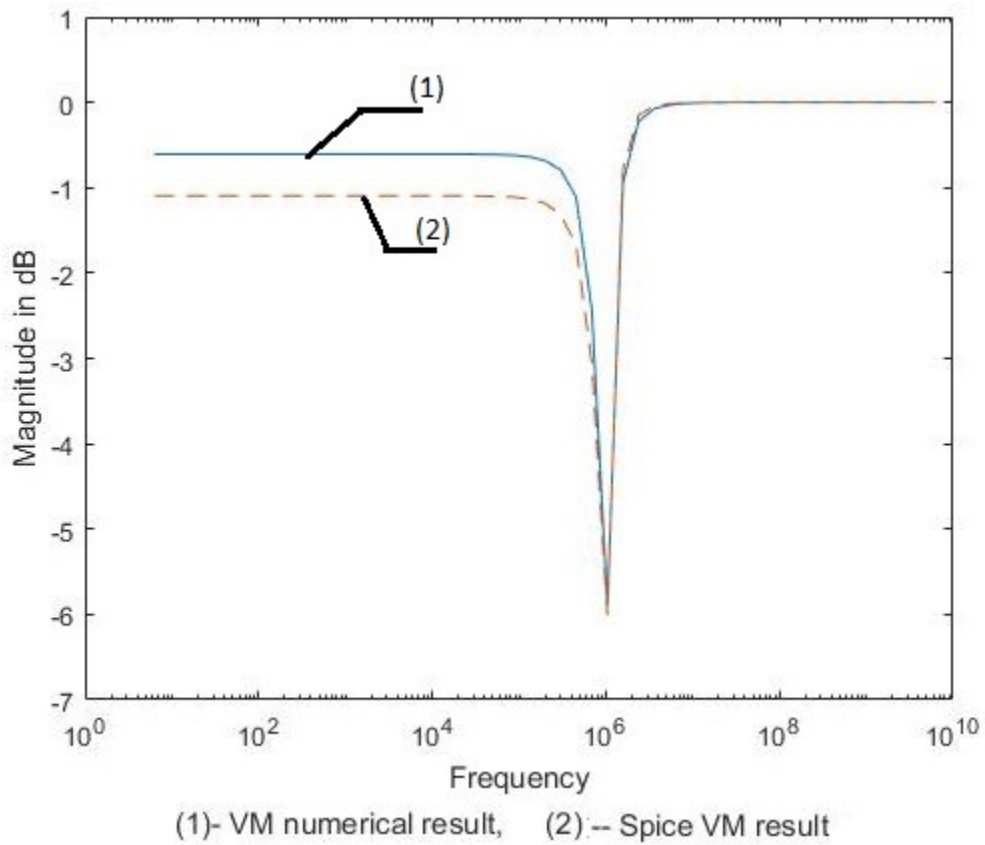


Figure B.9: Simulation and numerical results for NF $Q_p = 3$ of Figure B.7 (a)

- (1) '-': numerical VM response from Equation (B.8);
- (2) '--': VM response from SPICE simulation of Figure B.7 (a);

References

- [1] B. B. Bhattacharyya and M. N. S. Swamy, "Network transposition and its application in synthesis," IEEE Transactions on Circuit Theory, vol. 18, no. 3, pp. 394-397, 1971.
- [2] M. N. S. Swamy, "Transpose of a multiterminal element and applications," IEEE Transactions on Circuits and Systems II: Express Briefs, vol. 57, no. 9, pp. 696-700, 2010.
- [3] F. Yuan, CMOS Current-Mode Circuits for Data Communications. Springer Science & Business Media, 2007.
- [4] R. Raut and M. N. S. Swamy, Modern Analog Filter Analysis and Design: A Practical Approach. John Wiley & Sons, 2010.
- [5] A. S. Sedra and K. C. Smith, "A second-generation current conveyor and its applications," IEEE Transactions on Circuit Theory, vol. 17, no. 1, pp. 132-134, 1970.
- [6] I. A. Awad and A. M. Soliman, "Inverting second generation current conveyors: the missing building blocks, CMOS realizations and applications," International Journal of Electronics, vol. 86, no. 4, pp. 413-432, 1999.
- [7] E. Yuce and S. Minaei, "A modified CFOA and its applications to simulated inductors, capacitance multipliers, and analog filters," IEEE Transactions on Circuits and Systems I: Regular Papers, vol. 55, no. 1, pp. 266-275, 2008.
- [8] K. C. Smith and A. S. Sedra, "Realization of the Chua family of new nonlinear network elements using the current conveyor," IEEE Transactions on Circuit Theory, vol. 17, no. 1, pp. 137-139, 1970.

- [9] J. H. Huijsing, "Design and applications of the operational floating amplifier (OFA): the most universal operational amplifier," *Analog Integr. Cir. Signal Proc.*, vol. 4, no. 2, pp. 115-129, 1993.
- [10] D. Bolek, R. Senani, V. Biolkova and Z. Kolka, "Active elements for analog signal processing: classification, review, and new proposals," *Radioengineering*, vol. 17, no. 4, pp. 15-32, 2008.
- [11] K. C. Smith and A. S. Sedra, "The current conveyor—A new circuit building block," *Proc IEEE*, vol. 56, no. 8, pp. 1368-1369, 1968.
- [12] J. A. Svoboda, L. McGory and S. Webb, "Applications of a commercially available current conveyor," *International Journal of Electronics Theoretical and Experimental*, vol. 70, no. 1, pp. 159-164, 1991.
- [13] B. Wilson, "High-performance current conveyor implementation," *Electron. Lett.*, vol. 20, no. 24, pp. 990-991, 1984.
- [14] A. S. Sedra, G. W. Roberts and F. Gohh, "The current conveyor: history, progress and new results," *IEE Proceedings G-Circuits, Devices and Systems*, vol. 137, no. 2, pp. 78-87, 1990.
- [15] W. Surakampontorn, V. Riewruja, K. Kumwachara and K. Dejhan, "Accurate CMOS-based current conveyors," *IEEE Transactions on Instrumentation and Measurement*, vol. 40, no. 4, pp. 699-702, 1991.
- [16] A. Assi, M. Sawan and R. Raut, "A fully differential and tunable CMOS current mode opamp based on transimpedance-transconductance technique," in *Circuits and Systems*, 1997. Proceedings of the 40th Midwest Symposium On, 1997, pp. 168-171.

- [17] T. Kaulberg, "A CMOS current-mode operational amplifier," IEEE J Solid State Circuits, vol. 28, no. 7, pp. 849-852, 1993.
- [18] M. T. Abuelma'atti and H. A. Al-Zaher, "Current-mode sinusoidal oscillators using single FTFN," IEEE Trans. Circuits Syst. II Analog Digital Signal Process., vol. 46, no. 1, pp. 69-74, 1999.
- [19] R. Senani, "A novel application of four-terminal floating nullors," Proc IEEE, vol. 75, no. 11, pp. 1544-1546, 1987.
- [20] O. Cicekoglu, U. Cam and H. Kuntman, "Single-resistance-controlled sinusoidal oscillators employing single FTFN and grounded capacitors," in Circuits and Systems, 2001. MWSCAS 2001. Proceedings of the 44th IEEE 2001 Midwest Symposium On, 2001, pp. 874-877.
- [21] E. H. Nordholt, "Extending op amp capabilities by using a current-source power supply," IEEE Transactions on Circuits and Systems, vol. 29, no. 6, pp. 411-414, 1982.
- [22] J. H. Huijsing, "Operational floating amplifier," IEE Proceedings G (Circuits, Devices and Systems), vol. 137, no. 2, pp. 131-136, 1990.
- [23] M. N. S. Swamy, C. Bhushan and B. B. Bhattacharyya, "Generalized dual transposition and its applications," Journal of the Franklin Institute, vol. 301, no. 5, pp. 465-476, 1976.
- [24] M. N. S. Swamy, C. Bhushan and B. B. Bhattacharyya, "Generalized duals, generalized inverses and their applications," Radio and Electronic Engineer, vol. 44, no. 2, pp. 95-99, 1974.
- [25] M. N. S. Swamy, "Modified CFOA, its transpose, and applications," International Journal of Circuit Theory and Applications, vol. 44, no. 2, pp. 514-526, 2016.

- [26] J. Horng, C. Tsai and M. Lee, "Novel universal voltage-mode biquad filter with three inputs and one output using only two current conveyors," International Journal of Electronics, vol. 80, no. 4, pp. 543-546, 1996.
- [27] J. Horng, "Voltage-mode universal biquadratic filters using CCIs," IEICE Trans. Fund. Electron. Commun. Comput. Sci., vol. 87, no. 2, pp. 406-409, 2004.
- [28] S. Liu, "Cascadable current-mode filters using single FTFN," Electron. Lett., vol. 31, no. 23, pp. 1965-1966, 1995.
- [29] M. T. Abuelma'atti, "Cascadable current-mode filters using single FTFN," Electron. Lett., vol. 32, no. 16, pp. 1457-1458, 1996.
- [30] S. Liu and C. Hwang, "Realization of current-mode filters using single FTFN," International Journal of Electronics, vol. 82, no. 5, pp. 499-502, 1997.
- [31] E. Yuce and S. Minaei, "Universal current-mode filters and parasitic impedance effects on the filter performances," International Journal of Circuit Theory and Applications, vol. 36, no. 2, pp. 161-171, 2008.
- [32] P. R. Gray, P. J. Hurst, R. G. Meyer and S. H. Lewis, Analysis and Design of Analog Integrated Circuits. Wiley: 2001.
- [33] K. R. Laker and W. M. C. Sansen, Design of Analog Integrated Circuits and Systems. New York: McGraw-Hill, 1994.
- [34] B. Razavi, Design of Analog CMOS Integrated Circuits. New York: McGraw-Hill, 2001.

- [35] A. Fabre, O. Saaid and H. Barthelemy, "On the frequency limitations of the circuits based on second generation current conveyors," *Analog Integr. Cir. Signal Proc.*, vol. 7, no. 2, pp. 113-129, 1995.
- [36] S. Liu and J. Lee, "Voltage-mode universal filters using two current conveyors," *International Journal of Electronics*, vol. 82, no. 2, pp. 145-149, 1997.
- [37] J. Horng, M. Lee, H. Cheng and C. Chang, "New CCII-based voltage-mode universal biquadratic filter," *International Journal of Electronics*, vol. 82, no. 2, pp. 151-156, 1997.
- [38] C. Chang and S. Tu, "Universal voltage-mode filter with four inputs and one output using two CCIIIs," *International Journal of Electronics*, vol. 86, no. 3, pp. 305-309, 1999.
- [39] J. Horng, "High-input impedance voltage-mode universal biquadratic filter using three plus-type CCIIIs," *IEEE Trans. Circuits Syst. II Analog Digital Signal Process.*, vol. 48, no. 10, pp. 996-997, 2001.
- [40] J. Horng, "High input impedance voltage-mode universal biquadratic filters with three inputs using plus-type CCIIIs," *International Journal of Electronics*, vol. 91, no. 8, pp. 465-475, 2004.
- [41] M. Higashimura, "Current-mode allpass filter using FTFN with grounded capacitor," *Electron. Lett.*, vol. 27, no. 13, pp. 1182-1183, 1991.
- [42] S. Liu and Y. Liao, "Current-mode quadrature sinusoidal oscillator using single FTFN," *International Journal of Electronics*, vol. 81, no. 2, pp. 171-175, 1996.